



**USE OF TWO-WAY TIME TRANSFER MEASUREMENTS TO
IMPROVE GEOSTATIONARY SATELLITE NAVIGATION**

THESIS

Benjamin G. Dainty, Captain, USAF

AFIT/GSS/ENG/07-01

**DEPARTMENT OF THE AIR FORCE
AIR UNIVERSITY**

AIR FORCE INSTITUTE OF TECHNOLOGY

Wright-Patterson Air Force Base, Ohio

APPROVED FOR PUBLIC RELEASE; DISTRIBUTION UNLIMITED

The views expressed in this thesis are those of the author and do not reflect the official policy or position of the United States Air Force, Department of Defense, or the United States Government.

AFIT/GSS/ENG/07-01

USE OF TWO-WAY TIME TRANSFER MEASUREMENTS TO IMPROVE
GEOSTATIONARY SATELLITE NAVIGATION

THESIS

Presented to the Faculty

Department of Electrical and Computer Engineering

Graduate School of Engineering and Management

Air Force Institute of Technology

Air University

Air Education and Training Command

In Partial Fulfillment of the Requirements for the
Degree of Master of Science in Engineering and Environmental Management

Benjamin G. Dainty, B.S.E.P.

Captain, USAF

March 2007

APPROVED FOR PUBLIC RELEASE; DISTRIBUTION UNLIMITED.

USE OF TWO-WAY TIME TRANSFER MEASUREMENTS TO IMPROVE
GEOSTATIONARY SATELLITE NAVIGATION

Benjamin G. Dainty, B.S.E.P.
Captain, USAF


Approved:


Dr. John F. Raquet (Chairman)


1 MAR 07
date


Dr. Kerry D. Hicks, Lt Col, USAF (Member)

5 MAR 07
date


Dr. Nathan A. Titus, Lt Col, USAF (Member)

5 MAR 07
date


Dr. Richard R. Beckman, Capt, USAF (Member)

28 Feb 07
date

Abstract

An emerging use of GPS is to provide accurate navigation information for satellites in orbit. The GPS satellites are designed to provide service to terrestrial users, so the antenna array points directly towards the Earth and uses a narrow primary beamwidth. Because GEO altitudes are well above the GPS constellation, the Earth occludes most of the GPS signals to the satellite. Decreased satellite visibility is debilitating, as GPS navigation requires at least four visible satellites to determine position. To assist with the visibility problem, the receiver can look at the GPS satellite transmit antenna side lobes, but this does not entirely solve the navigation problem. GPS measurements are inherently bound by receiver clock errors. The clock error must be known or estimated in order to obtain meaningful ranging information. To obtain three-dimensional positioning, at least four satellites must be tracked to solve for three dimensions of position plus the receiver clock error.

A new method for improving geostationary navigation accuracy using GPS is to correct the time error by including Two-Way Time Transfer (TWTT) measurements. TWTT is a technique in which signals are simultaneously exchanged between two clocks, and is one of the most accurate methods of comparing clocks. By effectively removing the clock error between the GPS satellite and the GPS receiver, TWTT allows meaningful information to be gathered when less than four GPS satellites are available. The results show a 21-38% improvement in the 3-D RMS position accuracy while using TWTT between the GEO satellite and an atomic clock on the ground. There was a 60-70% improvement when the clock on the ground was synchronized to GPS time.

Table of Contents

	Page
Abstract	vii
Table of Contents	ix
List of Figures	xiii
List of Tables	xv
1 Introduction	1
1.1 Overview	1
1.2 Related Research	4
1.2.1 GPS Measurements Collected from Geosynchronous Transfer Orbit.....	4
1.2.2 High-Sensitivity GPS Receivers Built for GEO Operation.....	5
1.2.3 New GPS Satellite Architecture for High-Altitude Spacecraft	7
1.2.4 Two-Way Time Transfer Measurements used in Relative GPS Positioning.....	10
1.3 Problem Statement.....	11
1.4 Methodology.....	13
1.5 Thesis Overview	14
2 Background	15
2.1 Introduction	15
2.2 GPS Overview	15
2.2.1 Operational Control Segment (OCS)	15
2.2.2 Space Segment.....	16
2.2.3 User Segment.....	18
2.2.4 Pseudorange Measurements.....	19
2.3 Reference Coordinate Systems	20
2.3.1 ECI Reference Frame	21
2.3.2 ECEF Reference Frame	22
2.4 Two-Way Time Transfer Overview	23
2.4.1 Static TWTT.....	24
2.4.2 Dynamic TWTT	28
2.5 Kalman Filter.....	30
2.6 Summary.....	33
3 Methodology	35
3.1 Introduction	35
3.2 Parameters	35
3.2.1 Initial ECI State for Geostationary Satellite	36
3.2.2 Simulation Run Time and Time Step Interval	36
3.2.3 Ephemeris Date Selection.....	36
3.2.4 GPS Measurement Model Selection	37
3.2.5 Clock Type Selection	37
3.2.6 Clock Model Parameters	38
3.2.7 Two-Way Time Transfer Parameters	38
3.2.8 Kalman Filter Parameters.....	38
3.2.9 On/Off and Selection Flags	39

3.2.10	<i>Monte Carlo Parameters</i>	39
3.2.11	<i>Constants</i>	39
3.3	Truth Model	40
3.3.1	<i>Propagate Geostationary Satellite State</i>	40
3.3.2	<i>Calculate GPS Satellite Positions and Clock States</i>	44
3.3.3	<i>Clock Model</i>	44
3.4	Generated Measurements	47
3.4.1	<i>Pseudorange Measurements</i>	47
3.4.2	<i>Simple GPS Measurement Model</i>	48
3.4.3	<i>Advanced GPS Measurement Model</i>	50
3.4.4	<i>TWTT Measurements</i>	55
3.5	Kalman Filter	56
3.5.1	<i>Initial State Values</i>	56
3.5.2	<i>Filter Execution</i>	59
3.6	Results Analysis	63
3.7	Summary	65
4	Results and Analysis	67
4.1	Introduction	67
4.2	Preliminary Results	67
4.2.1	<i>Graphical Results</i>	67
4.2.2	<i>Root Mean Square Results</i>	70
4.3	Baseline Results	73
4.3.1	<i>Plotting the Results</i>	73
4.3.2	<i>Position Error</i>	79
4.4	Trade Study 1: Ephemeris Date	80
4.5	Trade Study 2: GPS Receiver Models	83
4.6	Trade Study 3: Gain Pattern Models	86
4.7	Trade Study 4: Clock Type Selection	88
4.8	Trade Study 5: TWTT Measurement Noise Error	90
4.9	Additional TWTT Study – TWTT Reference Clock Locked to GPS Time	91
4.10	Summary	92
5	Conclusions and Recommendations	95
5.1	Significance of Research	95
5.2	Trade Studies	97
5.2.1	<i>Baseline Results</i>	97
5.2.2	<i>Trade Study 1: Ephemeris Date</i>	98
5.2.3	<i>Trade Study 2: GPS Receiver Models</i>	98
5.2.4	<i>Trade Study 3: Gain Pattern Models</i>	99
5.2.5	<i>Trade Study 4: Clock Type Selection</i>	100
5.2.6	<i>Trade Study 5: TWTT Measurement Noise Error</i>	100
5.2.7	<i>Additional TWTT Study – Reference Clock Locked to GPS Time</i>	101
5.2.8	<i>Overall Results</i>	101
5.3	Recommendations for Future Research	102
5.3.1	<i>Improve Simulation Fidelity</i>	102
5.3.2	<i>Investigate a Non-standard GPS Receiver Antenna on the GEO Satellite</i>	103
	Appendix A – GPS Satellite Visibility Plots	105

Bibliography	109
--------------------	-----

List of Figures

	Page
Figure 1.1: GPS Signal Reception at GEO and HEO Orbital Altitudes	3
Figure 1.2: Falcon Gold GPS Signal Detection Locations	5
Figure 1.3: Simulated Received Power at GEO Orbital Altitude	6
Figure 1.4: Block II-R UHF Crosslink Antenna.....	8
Figure 1.5: Block II-R with Hemispherical Back-side Antenna.....	9
Figure 1.6: Real-Time Differential GPS Diagram.....	10
Figure 1.7: Simulation Block Diagram.....	13
Figure 2.1: Major Segments of the GPS System	16
Figure 2.2: The GPS Satellite Constellation.....	17
Figure 2.3: Illustration of Pseudorange Measurement.....	20
Figure 2.4: The ECI Coordinate System.....	21
Figure 2.5: The ECEF Coordinate System	22
Figure 2.6: Two-Way Time Transfer Technique.....	23
Figure 2.7: Static Two-Way Time Transfer Using a Satellite	24
Figure 2.8: Demonstration of the Sagnac Delay: Earth's Rotation Produces Non-Reciprocity	26
Figure 2.9: The Two-Way Time Transfer Equation	27
Figure 2.10: Dynamic Two-Way Time Transfer Using a Satellite.....	28
Figure 2.11: Kalman Filter Loop.....	33
Figure 3.1: Comparison of Simulated Clock Error and Quadratic Fit.....	46
Figure 3.2: Simple GPS Measurement Model Diagram (not to scale)	49
Figure 3.3: Advanced GPS Measurement Model Diagram (not to scale)	50
Figure 3.4: Simple GPS Antenna Gain Pattern Plot	51
Figure 3.5: Advanced GPS Antenna Gain Pattern Plot	52
Figure 3.6: Patch Antenna Gain Pattern Plot.....	53
Figure 3.7: Pseudorange Measurement Noise Error Standard Deviation Plot.....	54

Figure 4.1: Monte Carlo Measurements vs Time for 100 Iterations (Standard GPS Receiver Sensitivity, no TWTT)	68
Figure 4.2: 100-Run Monte Carlo Measurement Mean, Measurement Standard Deviation, and Filter-Computed Covariance	69
Figure 4.3: 3D Position RMS Over Time – Standard Sensitivity, no TWTT	72
Figure 4.4: GEO Satellite Clock Bias Error Filter Covariance for a Single Run (Standard Sensitivity with no TWTT Measurements)	74
Figure 4.5: Visible GPS Satellites from GEO Satellite (Standard Sensitivity).....	75
Figure 4.6: GEO Satellite Clock Bias Error Filter Covariance for a Single Run (Standard Sensitivity with TWTT Measurements Included)	76
Figure 4.7: GEO Satellite Clock Bias Error with TWTT Turned Off (top) and On (bottom) (Medium Sensitivity).....	77
Figure 4.8: Geo Satellite X-Direction Position Error with TWTT Turned Off (top) and On (bottom) (Medium Sensitivity).....	78
Figure 4.9: GPS Satellite Visibility Plots for a GEO Satellite Using Four Different Ephemeris Dates.....	82
Figure 5.1: Keystone Plot – 3D RMS Position Error vs. GPS Receiver Sensitivity Levels and Clock Configurations	96
Figure A.1: GPS Satellite Visibility from GEO for Standard Sensitivity Reciever (32 dB-Hz cutoff).....	105
Figure A.2: GPS Satellite Visibility from GEO for Standard Plus Sensitivity Reciever (27 dB-Hz cutoff).....	105
Figure A.3: GPS Satellite Visibility from GEO for Medium Sensitivity Reciever (22 dB-Hz cutoff).....	106
Figure A.4: GPS Satellite Visibility from GEO for Standard Plus Sensitivity Reciever (17 dB-Hz cutoff).....	106
Figure A.5: GPS Satellite Visibility from GEO for High Sensitivity Reciever (12 dB-Hz cutoff)	107
Figure A.6: GPS Satellite Visibility from GEO for Ultra High Sensitivity Reciever (7 dB-Hz cutoff).....	107

List of Tables

	Page
Table 1.1: GEONS State Estimation Error Statistics.....	7
Table 1.2: RMS Position Errors – GPS Broadcast Antenna Configuration vs User Clock Quality	9
Table 1.3: Position Accuracy Improvement When Using TWTT	11
Table 3.1: Process Noise Values for Atomic Clocks.....	46
Table 3.2: Initial State Error Standard Deviation Values	57
Table 4.1: Comparison of Monte Carlo Simulation and Single Run Simulation, no TWTT.....	71
Table 4.2: Simulation Baseline Results – RMS Position Error Values per Reciever Sensitivities.....	80
Table 4.3: Various Dates of Ephemeris and Resulting RMS Position Errors.....	81
Table 4.4: RMS Position Error Measurement Mean and Standard Deviation Across all Ten Ephemeris Dates.....	81
Table 4.5: Simple Model RMS Position Error Results with Pseudorange Measurement Noise Error Standard Deviation of 5 meters	84
Table 4.6: Comparison of Simple and Complex GPS Receiver Model RMS Position Error Values	84
Table 4.7: Simple Model RMS Position Error Results with Varying Pseudorange Measurement Noise Error Standard Deviations and GPS Look Angle of 42.6°	85
Table 4.8: Comparison of Simple and Complex GPS Receiver Models Based on Pseudorange Error	86
Table 4.9: Comparison of Simple and Complex GPS Gain Pattern Models and Resulting RMS Position Error Values	87
Table 4.10: Comparison of Clock Types and Resulting 3D RMS Position Error Values (in meters)	88
Table 4.11: Percent Decrease in 3D RMS Position Error Compared to Scenario Using Ovenized Crystal GEO Satellite Clock, no TWTT, Standard Sensitivity Receiver	89
Table 4.12: Comparison of Various TWTT Measurement Noise Error Standard Deviation Values and Resulting 3D RMS Position Errors (in meters)	90
Table 4.13: Comparison of 3D Position RMS Error (meters) When Using a TWTT Reference Clock that is Synchronized with GPS Time	92

USE OF TWO-WAY TIME TRANSFER MEASUREMENTS TO IMPROVE GEOSTATIONARY SATELLITE NAVIGATION

1 Introduction

1.1 Overview

The Global Positioning System (GPS) was developed by the United States Department of Defense to provide precise position, velocity, and time measurements to military users around the globe. Such information would provide U.S. military forces an unparalleled advantage among adversaries, allowing accurate navigation in any weather conditions during day or night operations. Upon initial operational capability on December 8, 1991 [17], civilian use of the GPS signal was intentionally corrupted with random error, allowing only the military users to have precise navigation. On May 2, 2000, the full accuracy of civilian GPS was made freely available to users of every nation [16]. Its role in daily life has broadened at a rapid rate, and now much of modern infrastructure is dependent upon GPS. Because of the growing reliance on GPS, users demand increased precision from the system.

An emerging use of GPS is to provide accurate navigation information for satellites in orbit. Previously, radar and optical range measurements to the satellite from the ground were collected, allowing operators to determine the position of the satellite. With GPS, the satellite can carry a receiver and calculate its own position using the GPS signals, eliminating the numerous ground stations and support costs. Additionally, GPS navigation allows the satellite to operate with a certain level of autonomy in station-keeping, making orbital corrections without the need for ground interaction. GPS

navigation is effective for satellites in Low Earth Orbit (LEO), but satellites operating in Geosynchronous Orbit (GEO) or Highly Elliptical Orbit (HEO) experience extreme performance degradation, for reasons described below.

GPS measurements are inherently bound by receiver clock errors. The clock error must be known or estimated in order to obtain meaningful ranging information. To obtain three-dimensional positioning, at least four satellites must be tracked to solve for three dimensions of position plus the receiver clock error. Because the receiver clock error can be estimated with four measurements, a user can have a very poor local clock attached to their receiver and still have accurate positioning.

The GPS satellites (approximately 20,200 kilometers altitude) are designed to provide service to terrestrial users, so the antenna array points directly towards the Earth and uses a narrow primary beamwidth. Because GEO (approximately 35,000 kilometers altitude) and HEO altitudes are well above the GPS constellation, the Earth occludes most of the GPS signals to the satellite. Decreased satellite visibility can be debilitating, as GPS navigation requires at least four visible satellites to determine position.

As a solution to the visibility problem, the receiver can look at more than just the primary GPS transmit beam that is intended for terrestrial use. The GPS transmit antennas have side lobes, shown in Figure 1.1, though at much lower power levels than the primary beam. These side lobes provide increased visibility for GEO and HEO satellites and are a requirement for high-altitude navigation.

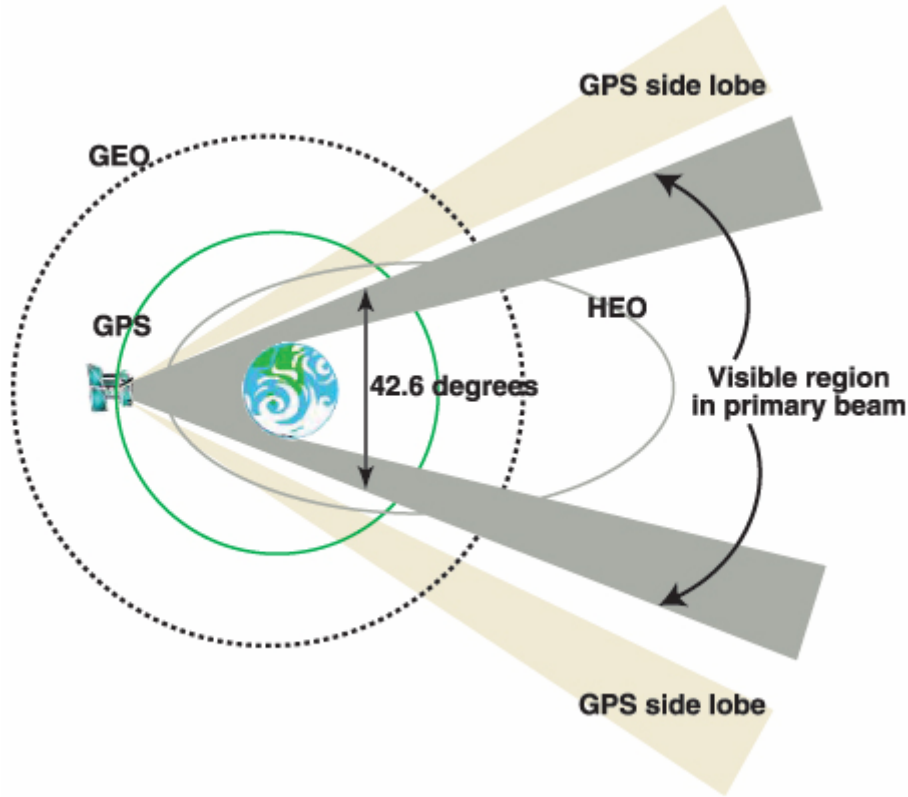


Figure 1.1: GPS Signal Reception at GEO and HEO Orbital Altitudes [1]

A current method for GPS navigation in high-altitude orbits is to use high-sensitivity GPS receivers and more powerful signal acquisition engines [1]. By increasing the sensitivity of the receiver, the very weak GPS signals become usable and the number of visible satellites increases, allowing for more precise positioning.

A new method for improving geostationary navigation accuracy using GPS is to correct the time error by including Two-Way Time Transfer measurements. Two-Way Time Transfer (TWTT) is a technique in which signals are simultaneously exchanged between two clocks. If the distance between the two clocks is equal, such as static clocks, the propagation delays cancel and the difference between the two clocks can be precisely measured [13]. Dynamic TWTT allows simultaneous signal exchanges to occur

between moving clocks, allowing vehicles, such as airplanes or satellites, to take advantage of TWTT [2]. TWTT is one of the most accurate methods of comparing clocks, so it can be used to create more accurate positioning using GPS by effectively removing the clock error between the GPS satellite and the GPS receiver. Using TWTT measurements, the clock error could be resolved, allowing less than four visible GPS satellites to provide meaningful ranging information.

1.2 Related Research

1.2.1 GPS Measurements Collected from Geosynchronous Transfer Orbit

A group of students at the United States Air Force Academy designed and constructed the “Falcon Gold” experiment that flew in 1997. The goal of this project was to measure GPS signals at high orbital altitudes using low-cost, low-power, off-the-shelf components [19]. The purpose was to test concepts, not to collect high-quality data.

The Falcon Gold experiment was a secondary payload on a DSCS spacecraft launch and was attached the side of the Centaur upper stage. Once the DSCS spacecraft separated from the upper stage and maneuvered into a geosynchronous orbit, the upper stage continued to orbit in a geosynchronous transfer orbit (GTO). The GTO orbit apogee and perigee were 35,200 and 200 kilometers, respectively, allowing the Falcon Gold to collect measurement data above and below the GPS constellation.

The experiment used an inexpensive two-inch patch antenna for the GPS receiver, which was modeled and used in this research simulation. Because of the hardware setup and limited ground link ability, only intermittent data could be collected. A total of 12 data frames were collected, detecting 25 PRN signals, as seen in Figure 1.2.

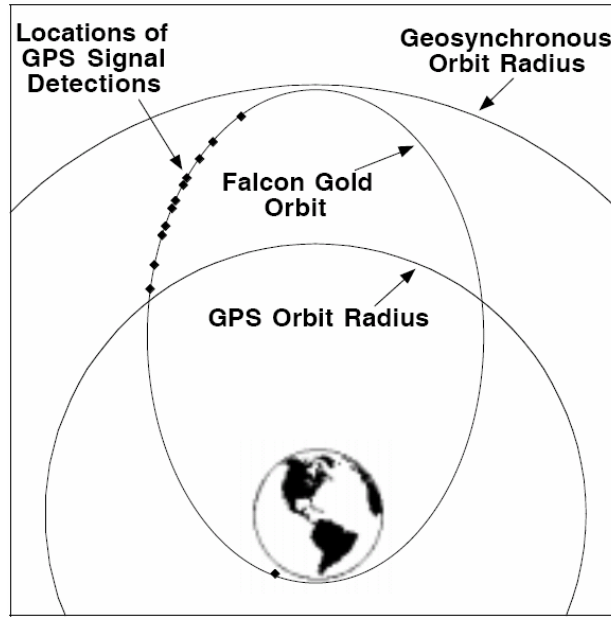


Figure 1.2: Falcon Gold GPS Signal Detection Locations [19]

The Falcon Gold experiment is one of the first examples of GPS signal detection at altitudes above the GPS constellation [19]. The future quality of performance can only improve, since Falcon Gold was able to achieve these capabilities by using only low-cost, low-power hardware. This demonstration was an important step in the progression of GPS-enabled satellites in high-altitude orbits.

The Falcon Gold experiment was also able to detect GPS sidelobe signals. This is very important for applications that could benefit from the extended coverage offered by sidelobe signals, such as high-altitude GPS positioning. New concepts may now be fully explored without hesitation, since the physical act of detecting sidelobe signals has been proven through experimentation.

1.2.2 High-Sensitivity GPS Receivers Built for GEO Operation

The National Aeronautics and Space Administration (NASA) developed a highly sensitive GPS receiver for use in geosynchronous orbits that is designed to track the very

weak GPS sidelobe signals [1]. This new receiver, called the Navigator, will drastically reduce GPS signal outages, providing more accurate positioning. The Navigator is able to track weak signals that are not usable by a standard GPS receiver, as seen in Figure 1.3. The lower dashed line represents the sensitivity threshold of the Navigator, while the upper dashed line represents a standard space receiver.

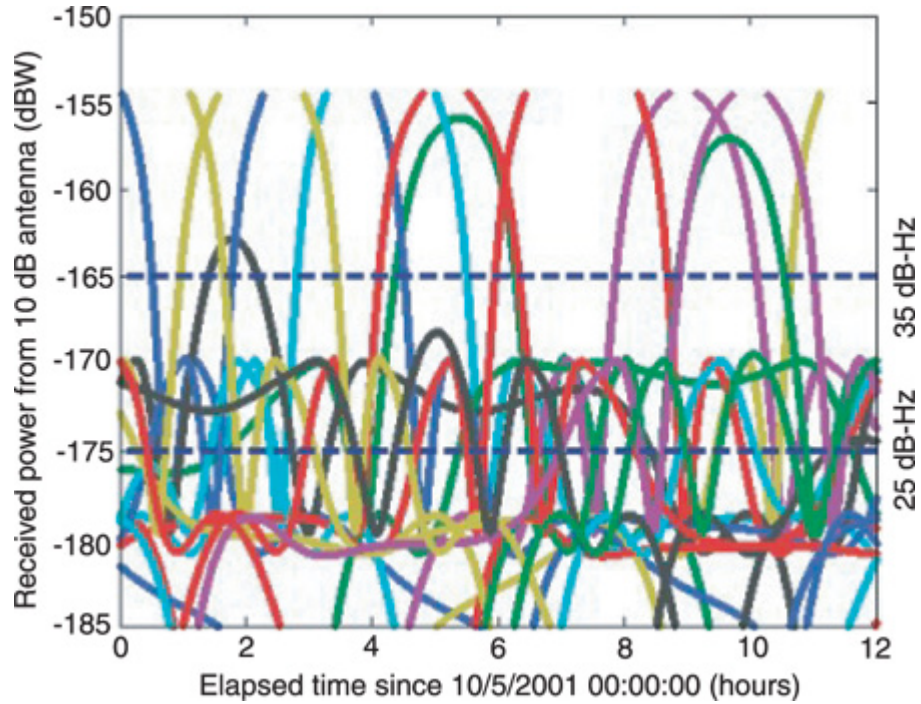


Figure 1.3: Simulated Received Power at GEO Orbital Altitude [1]

The Navigator is designed to provide autonomous navigation for spacecraft and includes the GPS Enhanced Onboard Navigation Systems (GEONS) software. GEONS is a powerful extended Kalman filter that uses an internal orbital dynamics model in conjunction with incoming measurements to generate a position solution, even when less than four GPS satellites are visible [1]. The GEONS orbital dynamics model is extremely sophisticated and can emulate a complex Earth gravity field and the forces due to solar and lunar gravity, atmospheric drag, and solar-radiation pressure. The Navigator

receiver feeds measurements to the GEONS, which is able to calculate precise GEO orbits to within 10 meters 3D root mean square as seen in Table 1.1.

Table 1.1: GEONS State Estimation Error Statistics [1]

	Radial	Intrack	Crosstrack	3D r.m.s.
Geostationary Orbit				
Position (m)	-4.424 ± 5.640	-0.546 ± 2.265	0.675 ± 2.462	7.959
Velocity (cm/s)	-0.038 ± 0.076	-0.133 ± 0.051	-0.001 ± 0.025	0.096
Low Earth Orbit				
Position (m)	0.036 ± 0.747	0.215 ± 0.995	0.103 ± 0.860	1.532
Velocity (cm/s)	-0.022 ± 1.613	0.002 ± 0.079	0.0243 ± 0.107	0.210

The research conducted in this thesis is similar to the concept of the Navigator, which supplements pseudorange measurements with additional data to produce a more accurate navigation solution. Instead of a high-fidelity orbital mechanics model, this research uses TWTT to improve the GPS accuracy at high altitudes. The Navigator requires specialized hardware and the GEONS software, while TWTT measurements could be used with a very simple GPS receiver and low-quality onboard clock.

The Navigator simulation uses slightly different values for the noise density and the gain patterns of the associated antennas, so a direct “apples-to-apples” comparison is not possible for this thesis research. However, the close similarity offers a good benchmark for validating the simulation used in this thesis.

1.2.3 New GPS Satellite Architecture for High-Altitude Spacecraft

The Aerospace Corporation conducted a study in 1998 to examine the effects of various GPS satellite architectures and user processing options on the accuracy of high altitude orbit determination using GPS [20]. The study was divided into two main investigations to examine the tradeoff between GPS system modifications and user

equipment complexity. It includes several hypothetical GPS satellite antenna configurations and receiver clock choices.

Five antenna architectures were used in Monte Carlo simulations: the Block II-A main beam (42°), the Block II-R main beam (38°), the Block II-R UHF crosslink antenna (120°), and a hemispherical back-side antenna combined with either the II-A or II-R main beam. The three receiver clock choices were a standard crystal, an improved crystal, and a standard atomic clock.

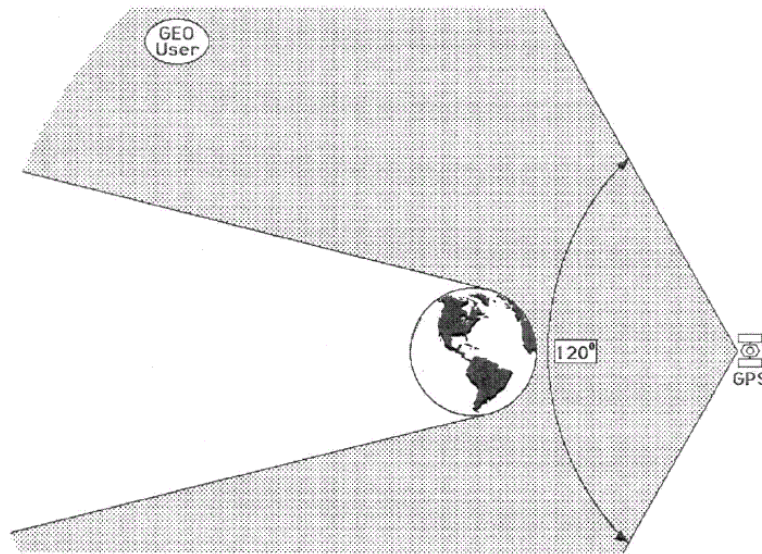


Figure 1.4: Block II-R UHF Crosslink Antenna [20]

The simulations did show that GPS modifications would improve positioning accuracy at GEO by increasing signal availability, but would require a significant increase in cost and complexity. Therefore, a complete redesign of the GPS satellites to assist GEO navigation is highly improbable.

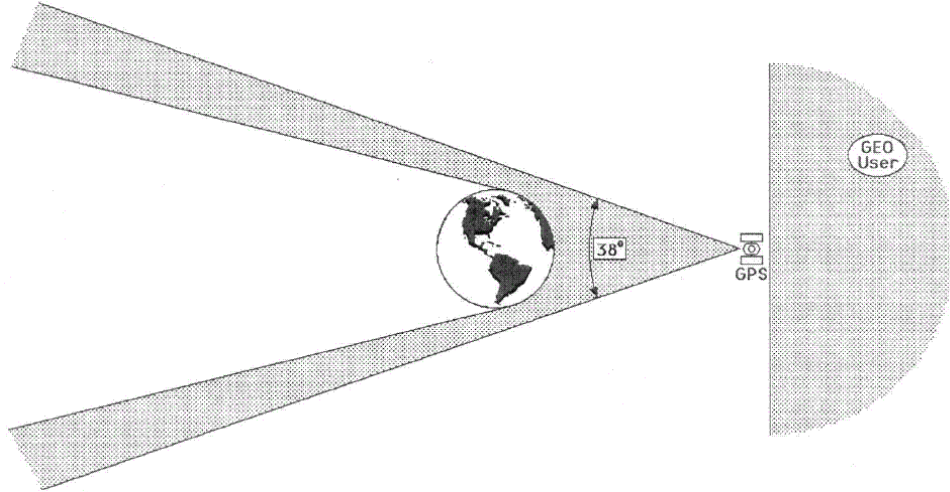


Figure 1.5: Block II-R with Hemispherical Back-side Antenna [20]

The most important result from this study concerns the choice of receiver clock. By using a clock with greater accuracy, the positioning error decreases significantly as seen in Table 1.2. Such a concept is the crux of this thesis research, purporting that introducing a more accurate clock via TWTT can significantly improve GEO positioning using GPS.

Table 1.2: RMS Position Errors – GPS Broadcast Antenna Configuration vs User Clock Quality [20]

	II-R Main (38°) Only		II-A Main (42°) Only		UHF Crosslink (120°)		II-R Main (38°) + Backside		II-A Main (42°) + Backside	
Standard Crystal	3D	16.9 m	3D	15.3 m	3D	3.6 m	3D	4.5 m	3D	4.5 m
	R	6.3 m	R	6.0 m	R	2.4 m	R	2.7 m	R	2.7 m
	I	15.4 m	I	13.9 m	I	2.5 m	I	3.4 m	I	3.5 m
	C	3.3 m	C	2.1 m	C	1.0 m	C	1.0 m	C	1.0 m
Improved Crystal	3D	11.8 m	3D	11.0 m	3D	3.5 m	3D	4.4 m	3D	4.4 m
	R	4.6 m	R	4.4 m	R	2.3 m	R	2.7 m	R	2.6 m
	I	10.7 m	I	9.8 m	I	2.5 m	I	3.4 m	I	3.5 m
	C	2.0 m	C	2.1 m	C	1.0 m	C	1.0 m	C	0.9 m
Atomic Clock	3D	8.4 m	3D	8.1 m	3D	2.8 m	3D	3.4 m	3D	3.4 m
	R	2.4 m	R	2.3 m	R	1.4 m	R	1.7 m	R	1.7 m
	I	7.8 m	I	7.6 m	I	2.1 m	I	2.8 m	I	2.8 m
	C	1.7 m	C	1.6 m	C	1.0 m	C	0.9 m	C	0.9 m

R = radial, I = in-track, C = cross-track

1.2.4 Two-Way Time Transfer Measurements used in Relative GPS Positioning

A previous AFIT masters degree student researched the effects of TWTT on networked differential GPS positioning [8]. Differential GPS techniques provide relative positioning between a mobile GPS receiver and a fixed receiver with well-known position information, as shown in Figure 1.6. The fixed receiver compares its GPS-calculated position with its known geographic position and determines the corrections necessary for eliminating the difference between the two. These corrections can then be sent to a mobile receiver, providing the same amount of positioning accuracy as the known location. In a networked system, multiple receivers exist in various locations, such as a swarm of Unmanned Aerial Vehicles (UAVs), and are linked to the same fixed reference station. Differential GPS accuracy is on the order of centimeters to meters, depending upon the method used [21].

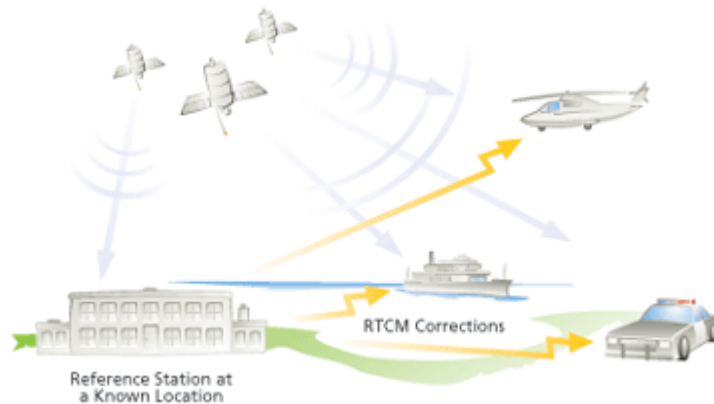


Figure 1.6: Real-Time Differential GPS Diagram [10]

This previous research, found in [8], used a MATLAB[®] simulation to explore the effects of introducing TWTT measurements to a network of six mobile receivers. The TWTT measurement accuracy standard deviation varied between 3, 0.3, 0.03, and 0.003 meters. Smaller TWTT measurement error results in greater position measurement

accuracy as seen in Table 1.3, which was created using the data produced in [8]. Clearly, there is a significant benefit to using TWTT measurements with GPS positioning.

Table 1.3: Position Accuracy Improvement When Using TWTT

Scenario	3-D Position RMS Value (m)	Percent Increase in Accuracy
ρ	1.587	
ρ +TWTT(3m)	1.415	10.84%
ρ +TWTT(0.3m)	0.935	41.08%
ρ +TWTT(0.03m)	0.890	43.92%
ρ +TWTT(0.003m)	0.889	43.98%

ρ = pseudorange measurement
TWTT(x) = TWTT measurement where *x* = accuracy level

The methodology found in [8] is similar to the research conducted for this thesis. The main difference is that this research examines TWTT measurements used with GPS positioning of geostationary satellites, versus a network of receivers on Earth. Both simulations use similar assumptions, such as ignoring relativistic effects and other types of error that can be modeled, calculated, and removed from physical measurements. The glaring similarity is the idea that TWTT can drastically improve GPS positioning accuracy.

1.3 Problem Statement

The main objective of this research is to examine the impact of adding TWTT measurements to geostationary satellite positioning using GPS measurements. By constraining relative clock errors, TWTT measurements can improve the positioning accuracy.

By using TWTT measurements, a GPS receiver in geostationary orbit could possibly calculate a good navigation solution without needing a high-sensitivity receiver. If the satellite did have a high-sensitivity receiver, the navigation solution would be even

better. TWTT measurements would eliminate the need for a precise clock on the satellite because it would only need a precise reference clock on the ground. Essentially, using TWTT with a highly accurate clock on the ground and a low quality clock on the satellite would be comparable to putting a highly accurate clock on the satellite itself. A highly accurate clock enables the system to meaningfully use individual pseudorange measurements, because the clock error can be accurately modeled over time.

This research involves five trade studies that quantify the benefits of using TWTT measurements with GPS. The first trade study involves using ephemeris data from several days to ensure that the results are not dependent upon the day that is used. The second trade study examines the differences between a simple GPS receiver model and a complex GPS receiver model to determine the effect of simulation model accuracy. The simple GPS receiver model uses a simple cut-off angle between the satellites and the Earth and a constant pseudorange measurement noise value. The complex GPS receiver model uses gain patterns for the GPS and geostationary satellite antennas and a varying pseudorange measurement noise that depends on received signal strength. The third trade study examines the differences between a rudimentary gain pattern and a more accurate gain pattern for the GPS satellite antenna to determine the effect of gain pattern accuracy levels. The fourth trade study investigates the effects of using different types of clocks for the geostationary satellite clock and the TWTT reference clock to determine the effect of using a high-accuracy clock versus a low-accuracy clock. The fifth trade study evaluates the results as a function of TWTT measurement accuracy.

1.4 Methodology

A simulation using MATLAB[®] examines the potential benefits of using TWTT measurements in addition to GPS measurements for determining the position of a geostationary satellite in orbit. The simulation is comprised of five main functions, shown in Figure 1.7, which involve loading parameters, generating truth data, generating measurement data, executing a Kalman filter, and analyzing the results.

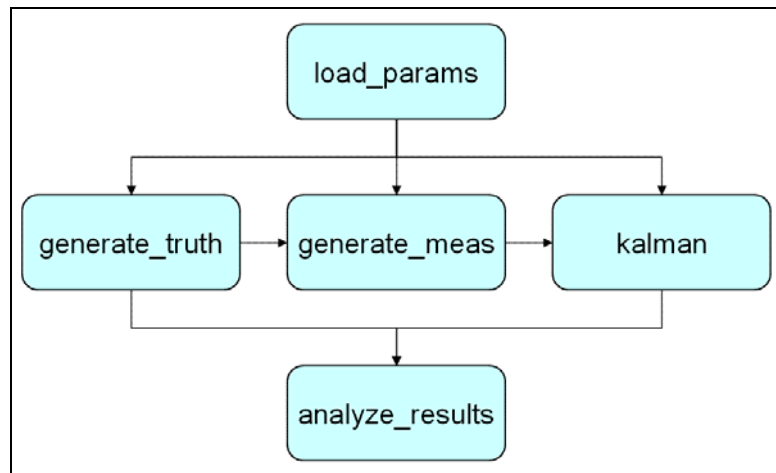


Figure 1.7: Simulation Block Diagram

The *load_params* function allows the user to input the desired parameters into the simulation. These parameters are used by the *generate_truth*, *generate_meas*, and *kalman* functions. The *generate_truth* function generates the ‘true’ values for the positions of each GPS satellite and the position of the geostationary satellite. The *generate_meas* function uses the ‘true’ data to calculate pseudorange measurements and the TWTT measurements, simulating what an actual GPS receiver would collect. The *kalman* function uses the generated measurements in a Kalman filter to estimate the position of the geostationary satellite. The *analyze_results* function compares the ‘true’ data with the Kalman filter results to determine how accurately the filter was able to

position the geostationary satellite using the measurements provide by *generate_meas*. A more detailed description of each function is located in Chapter Three.

1.5 Thesis Overview

Chapter Two describes the fundamental topics that are related to this research. This chapter includes backgrounds of GPS, orbital reference frames, Two-Way Time Transfer, and the Kalman filter. The topic of GPS includes an overview of pseudorange measurements and associated equations, while the topic of TWTT includes an overview of static and dynamic methods and associated equations. The topic of orbital reference frames describes the Earth-Centered Earth-Fixed (ECEF) and Earth-Centered Inertial (ECI) coordinate systems.

Chapter Three describes a simulation of positioning a geostationary satellite in orbit using simulated GPS measurements with and without TWTT measurements. Using the simulation, five trade studies were conducted to examine the impact on system performance. The trade studies include comparing the results obtained from using ephemeris data from different days, the differences between a simple and complex GPS receiver model, the differences between simple and complex gain pattern data, the differences between using high- and low-accuracy clocks for the geostationary and TWTT reference clocks, and the differences in adjusting the TWTT measurement noise error.

Chapter Four discusses the results of each trade study and provides an analysis of each trade study. Chapter Five explains conclusions and recommendations for further research.

2 Background

2.1 Introduction

This chapter describes the fundamental topics that became the building blocks of this research. There is a brief overview of GPS along with an explanation of system architecture and pseudorange measurements. This chapter describes the applicable reference frame coordinate systems, explains the theory and mechanics of Two-Way Time Transfer, and demonstrates the method of using a Kalman filter.

2.2 GPS Overview

The following sections will describe the GPS architecture, including the Operational Control Segment (OCS), the space segment, and the user segment as shown in Figure 2.1. The next section will describe how the system produces navigation information via pseudorange measurements. This section closely follows the descriptions given in [8] and [25].

2.2.1 Operational Control Segment (OCS)

The OCS is comprised of the Master Control Station (MCS), monitor stations, and ground antennas. The MCS provides the command and control for the entire GPS system and tracks GPS satellite orbits, monitors and sustains GPS satellite health, and maintains GPS time [16]. Operated by the MCS, the monitor stations are spread across the Earth and constantly observe GPS satellite signals. Monitor stations have a GPS receiver, an atomic clock, meteorological equipment, and communications hardware for

transmitting measurement data back to the MCS [16]. The ground antennas reside with a monitor station and communicate with the GPS satellites. Operated by the MCS, the ground antennas are responsible for transmitting commands and other messages to the satellites and for receiving telemetry and system health from the satellites [16].

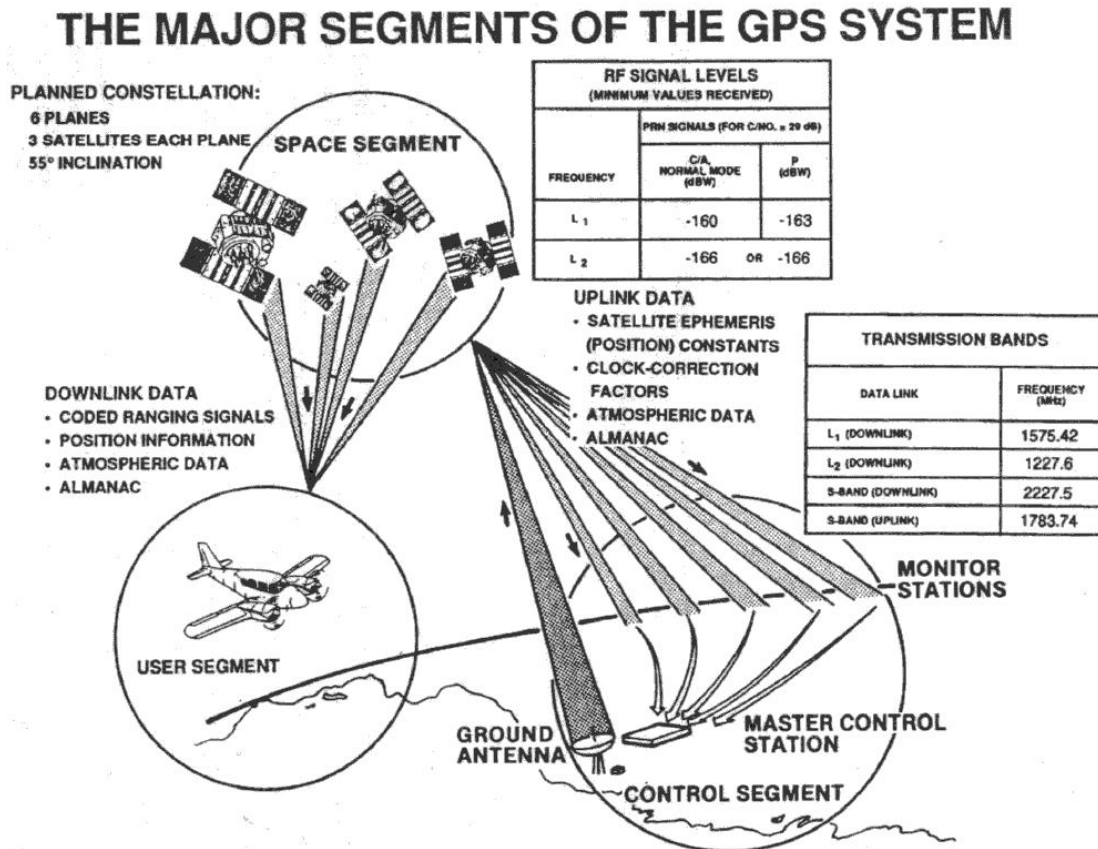


Figure 2.1: Major Segments of the GPS System [15]

2.2.2 Space Segment

The nominal GPS constellation consists of 24 satellites placed into six orbital planes at an altitude of 20,200 kilometers. Each orbital plane has an inclination of 55

degrees and holds four satellites. The orbital planes are labeled A through F, as seen in Figure 2.2.

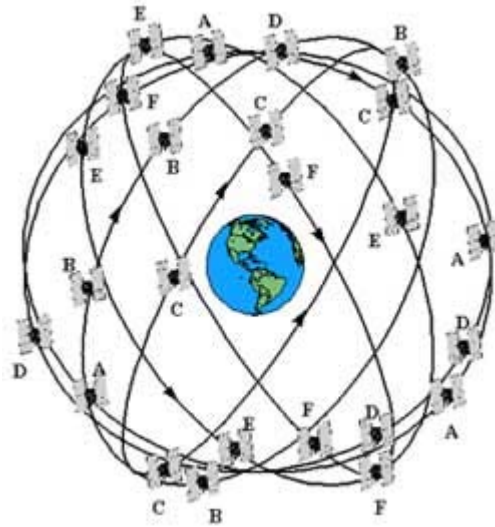


Figure 2.2: The GPS Satellite Constellation [12]

The responsibilities of the OCS include creating an ephemeris for each satellite, which is a compiled set of state vectors for each satellite predicted over time [23]. Ephemeris values describe the shape of the satellite's orbit, and can be used to calculate the satellite's position and velocity. A Kalman filter calculates ephemeris values by propagating the GPS satellites' positions and velocities forward in time. The final result is called the broadcast ephemeris. All satellites in the GPS constellation transmit the broadcast ephemeris data for each satellite, allowing a user to know the position of each GPS satellite.

A precise ephemeris data set is compiled roughly two weeks after the actual orbit by a private conglomeration of users. Technically it is not a true ephemeris, but rather a historical collection of observables. It includes measurement data from hundreds of ground stations and accounts for ionospheric, tropospheric, and many other errors. The

broadcast ephemeris is a prediction, while the precise ephemeris is compiled using past measurements. The precise ephemeris is extremely accurate, though post-dated, and is considered to be the true position of the GPS satellite. Precise ephemeris data used in this simulation comes from the International GPS Service (IGS).

Each GPS satellite broadcasts a global navigational message on two L-band frequencies, L1 (1575.42 Hz) and L2 (1227.60 Hz) [18]. The navigational message is unique to each satellite, modulated on a pseudo-random noise (PRN) signal. It provides satellite positions and satellite clock corrections for use in computing the user's navigation solution, to include position, velocity, and time.

2.2.3 User Segment

The GPS signal is globally available for use by any receiver. A typical GPS receiver must have seven components in order to correctly acquire and track the GPS signal [18]. It must have:

- an omnidirectional antenna to receive the encoded signals transmitted by the GPS satellites
- a filter to remove interfering signals
- an amplifier to boost the GPS signal
- a delay lock loop receiver and demodulator to provide estimates of the pseudorange, carrier phase, and navigational data for each satellite
- a navigation data processor to calculate the position of each satellite based on the navigation data.
- an algorithm to estimate the user position and velocity state vector

- a reference oscillator to provide a time and frequency reference for the receiver.

2.2.4 Pseudorange Measurements

Two pseudorandom noise (PRN) codes, the Coarse-Acquisition (C/A) code and the Precision (P(Y)) code, are modulated onto the L1 and L1/L2 bands respectively [23]. Each PRN code is unique for a given satellite. To make a GPS measurement, the PRN signal transmit time between the GPS satellite and the user must be determined. To do this, the user's receiver compares an internal copy of the PRN code with the PRN signal received from the satellite. By calculating the time shift required to align the two PRN codes and multiplying by the speed of light, the user can determine the pseudorange between the receiver and the GPS satellite.

Because the true range from the receiver to the satellite is corrupted by receiver clock errors, it is called a *pseudorange*. A pseudorange measurement (ρ) can be expressed as:

$$\rho = \sqrt{(x^{sat} - x_{rec})^2 + (y^{sat} - y_{rec})^2 + (z^{sat} - z_{rec})^2} + c\delta t_{rec} - c\delta t^{sat} + v_{PR} \quad (2.1)$$

where

$x^{sat}, y^{sat}, z^{sat}$ = true ECEF position of the satellite (meters)

$x_{rec}, y_{rec}, z_{rec}$ = true ECEF position of the receiver (meters)

δt_{rec} = receiver clock bias (seconds)

δt^{sat} = satellite clock bias (seconds)

v_{PR} = pseudorange error (meters)

c = speed of light (2.99792458×10^8 meters/second)

Figure 2.3 displays the concept of a pseudorange measurement. At least four satellites are needed to simultaneously estimate the receiver's position and clock error (x , y , z , δt_{rec}). In Figure 2.3, the b term is equal to $-c\delta t_{rec} + c\delta t^{sat} - v_{PR}$, as described above.

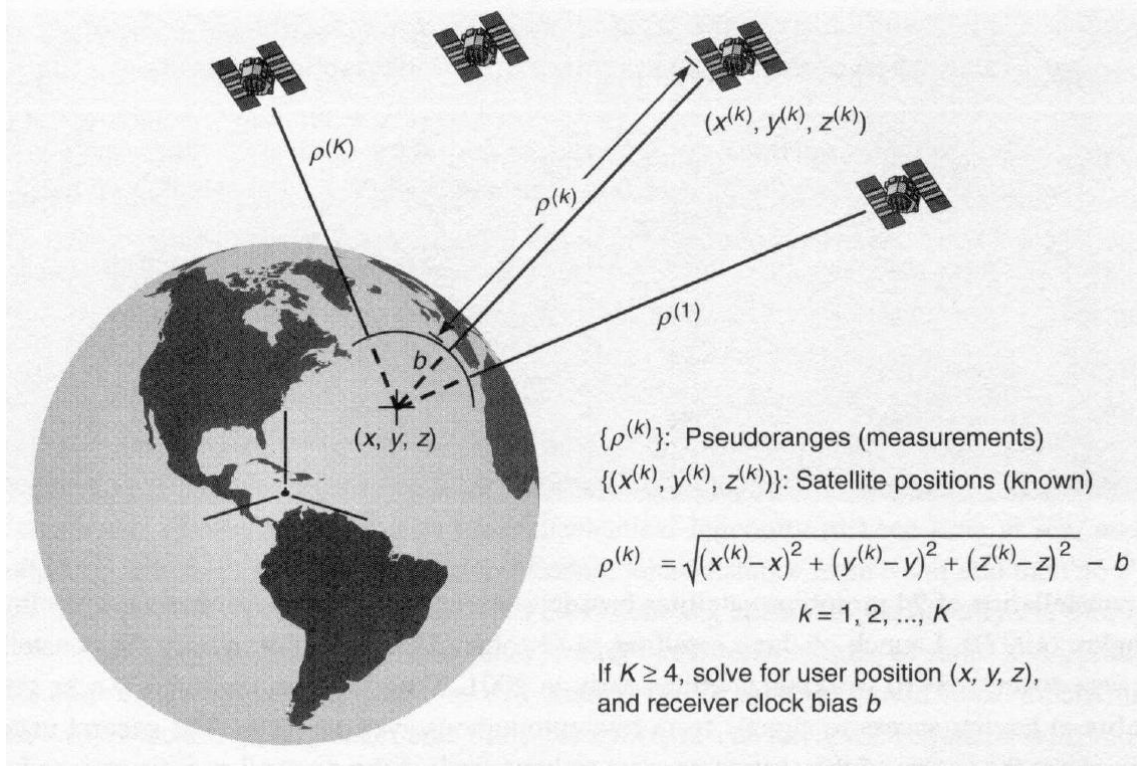


Figure 2.3: Illustration of Pseudorange Measurement [16]

2.3 Reference Coordinate Systems

All motion in the universe is relative, so there are many different ways to express the reference frame that describes an object's orbital motion around the Earth. Each reference frame has advantages for particular circumstances, so this research utilizes two reference frames: Earth-Centered Inertial (ECI) and Earth-Centered Earth-Fixed (ECEF). Both the ECI and ECEF reference frames are Cartesian (orthogonal) coordinate systems. This section closely follows the descriptions given in [25].

2.3.1 ECI Reference Frame

The Earth-Centered Inertial coordinate system is typically used when describing the motion of an object orbiting the Earth, as it is an inertial frame and is not concerned with the rotation of the Earth. For ECI, the origin is located at the center of the Earth with the \hat{X} axis pointing toward the vernal equinox, also called the First Point of Aries, in the equatorial plane. The \hat{Z} axis points through the North Pole along the Earth's axis of rotation, and the \hat{Y} axis points ninety degrees from the \hat{X} axis in the equatorial plane, following the right-hand rule. The $\hat{X}, \hat{Y}, \hat{Z}$ axes are often referred to as $\hat{I}, \hat{J}, \hat{K}$, as seen in Figure 2.4. Since the \hat{X} axis direction is fixed in space, the ECI coordinate system does not change as the Earth spins about its axis and revolves around the sun.

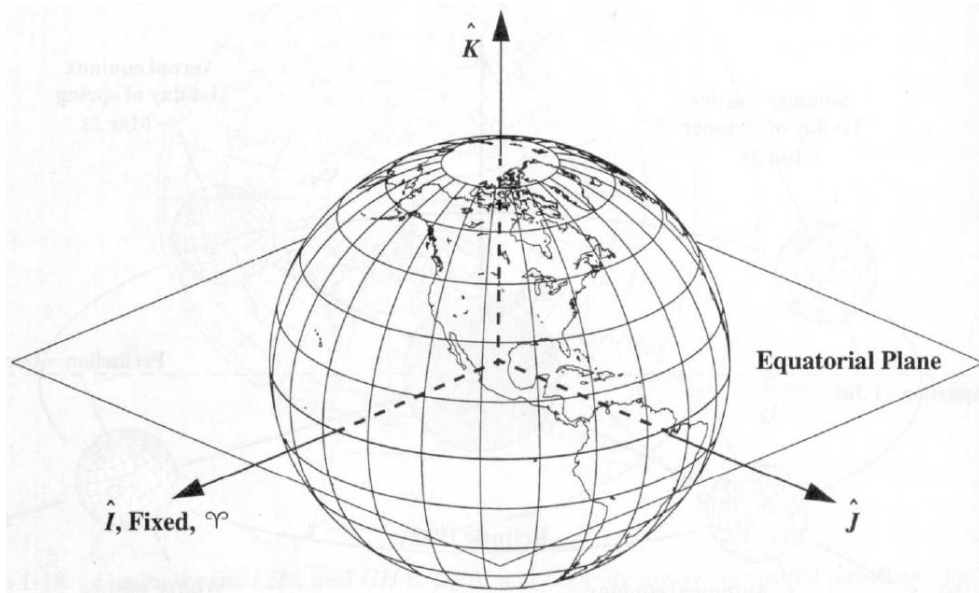


Figure 2.4: The ECI Coordinate System [23]

2.3.2 ECEF Reference Frame

The Earth-Centered Earth-Fixed coordinate system is typically used for Earth-based satellite tracking operations where the satellite's coordinates need to be expressed in relation to a geographic location on the surface of the Earth. Unlike the ECI reference frame, the ECEF reference frame is always aligned with a particular longitude, normally the Prime Meridian at Greenwich, and thus rotates with the Earth. The origin is still located at the center of the Earth, and the \hat{Z} axis still points through the North Pole along the axis of rotation, while the \hat{X} axis points toward a designated longitude and rotates with the Earth. The \hat{Y} axis always points ninety degrees from the \hat{X} axis. Figure 2.5 portrays the ECEF coordinate system.

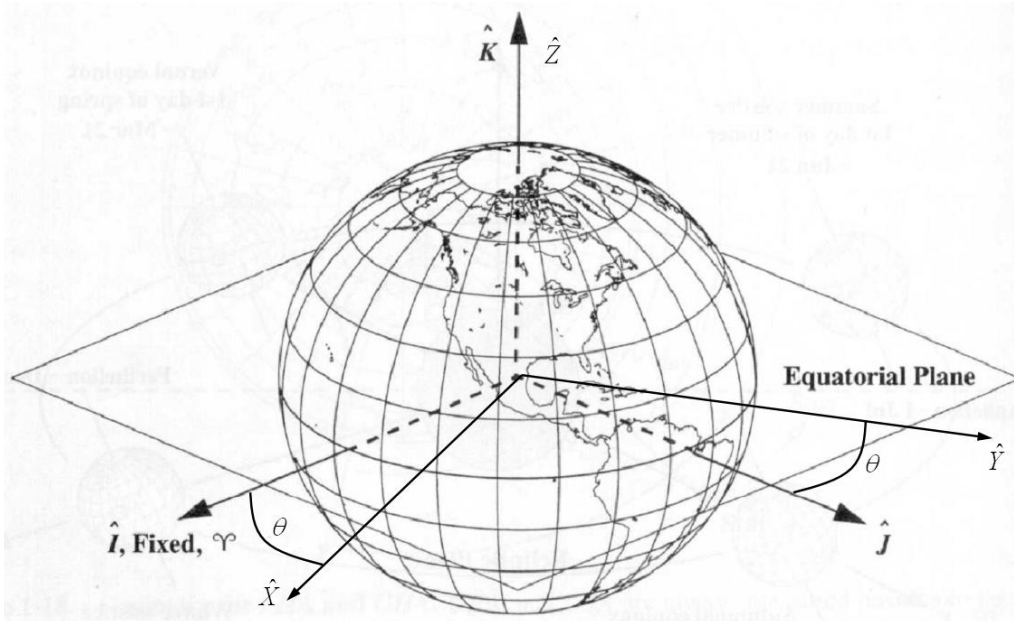


Figure 2.5: The ECEF Coordinate System

The ECEF coordinate system proves useful when examining geostationary orbits, since a geostationary orbit rotates at the same rate as the Earth. If a satellite were situated in a perfectly geostationary orbit, the satellite's \hat{X} , \hat{Y} , \hat{Z} coordinates would remain

constant. Because this research examines the errors in the navigation solution of a geostationary satellite, the results will be presented in the ECEF coordinate system, making them more intuitive to interpret.

2.4 Two-Way Time Transfer Overview

Two-Way Time Transfer (TWTT) is a technique in which signals are simultaneously exchanged between two users to measure their relative clock offsets. If the paths between the two users are reciprocal, the delays cancel and the difference between the two clocks is half the difference in time interval counter readings [13]. Figure 2.6 explains the TWTT technique in more detail using a simplified setup with two clocks connected via two cables.

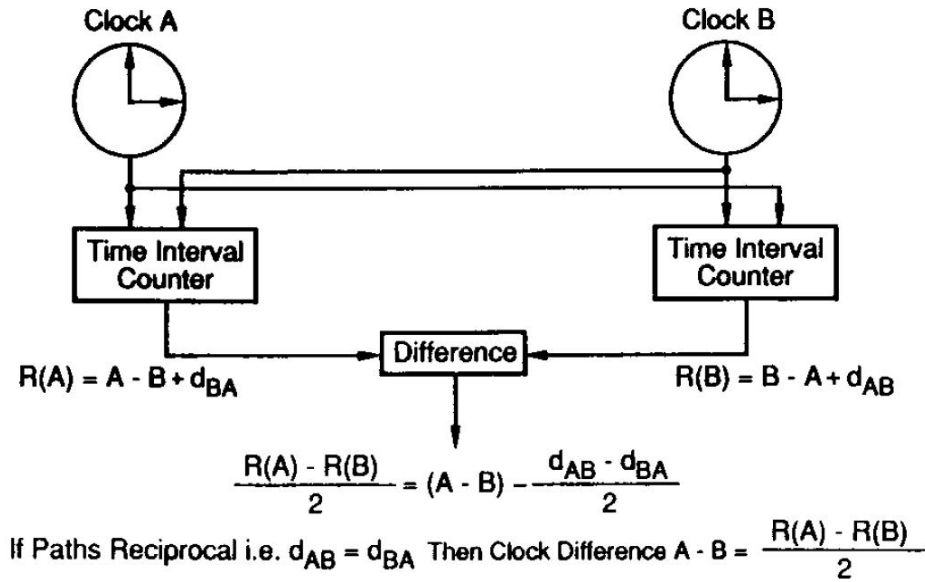


Figure 2.6: Two-Way Time Transfer Technique [13]

In Figure 2.6,

A = Time Interval Counter measurement from Clock A

B = Time Interval Counter measurement from Clock B

d_{AB} = delay caused in cable from Clock A to Clock B

d_{BA} = delay caused in cable from Clock B to Clock A
 $R(A)$ = difference between Clock A and Clock B with cable delay d_{BA}
 $R(B)$ = difference between Clock B and Clock A with cable delay d_{AB}

There are two types of TWTT, those being static and dynamic. Static TWTT uses two or more transceivers whose positions are held constant during the transmission and reception of the measurement signals. Dynamic TWTT is a more recent development that allows one or more of the transceivers to be moving [2]. This section closely follows the descriptions given in [8] and [25].

2.4.1 Static TWTT

TWTT commonly involves two static clocks on the Earth's surface that use a geostationary satellite to relay signals between them. The connection between the two clocks proceeds through an antenna, a transmitter, an uplink to the satellite, a route through the satellite, a downlink from the satellite, an antenna, and a receiver [13]. This arrangement is depicted in Figure 2.7.

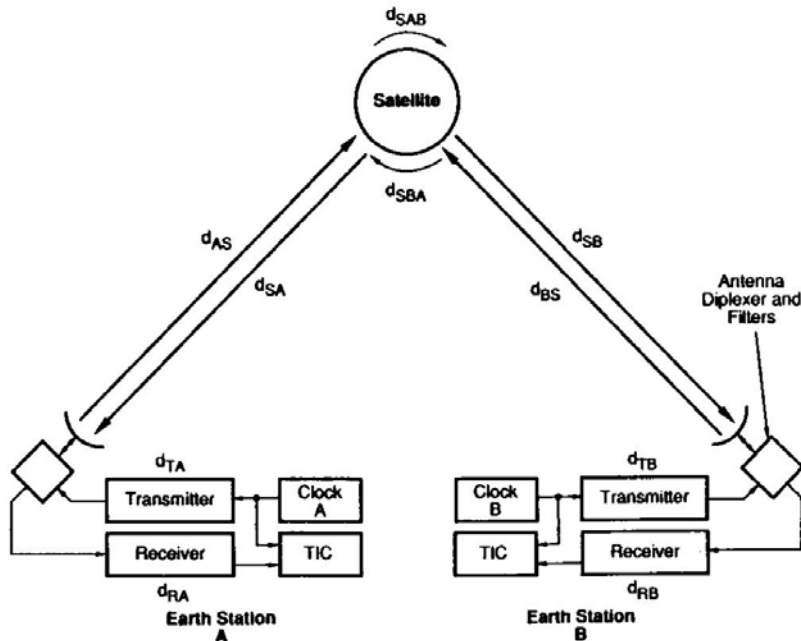


Figure 2.7: Static Two-Way Time Transfer Using a Satellite [13]

In Figure 2.7,

d_{AS} = delay between Receiver A and satellite during time of transmission

d_{SA} = delay between satellite and Receiver A during time of transmission

d_{BS} = delay between Receiver B and satellite during time of transmission

d_{SB} = delay between satellite and Receiver B during time of transmission

d_{TA} = delay in Transmitter A

d_{TB} = delay in Transmitter B

d_{RA} = delay in Receiver A

d_{RB} = delay in Receiver B

d_{SAB} = delay in satellite when signal is going from Transmitter A to Receiver B

d_{SBA} = delay in satellite when signal is going from Transmitter B to Receiver A

TIC = Time Interval Counter

The Time Interval Counters (TICs) make basic time interval measurements at each site. Each TIC starts with a pulse from the local clock and ends when the signal is received from the remote clock. The remote clock sends a pulse at the same time that the local clock sends a pulse. Nominally, one pulse per second is the rate used for TWTT. Each station records the time interval and the information is sent to the other station where the two values are differenced. The data rate required for exchanging pulses is trivial, allowing TWTT to occur in real time [13].

The time interval information that is differenced at each station includes all delays shown in Figure 2.7. An additional delay term, the Sagnac delay, is also included. The Sagnac delay is associated with the Earth's rotation and the fact that transmitted signals have a finite velocity, as demonstrated in Figure 2.8. The Earth stations and satellite are at position 1 when the pulses are sent to the satellite. The rotation of the Earth causes the stations to move to position 3 before the signals are received. The Earth's rotation and the finite velocity of the signals have combined to make the transmit

signal path longer from Station B to Station A, and shorter from Station A to Station B.

For static TWTT, the Sagnac error is effectively a deterministic propagation delay.

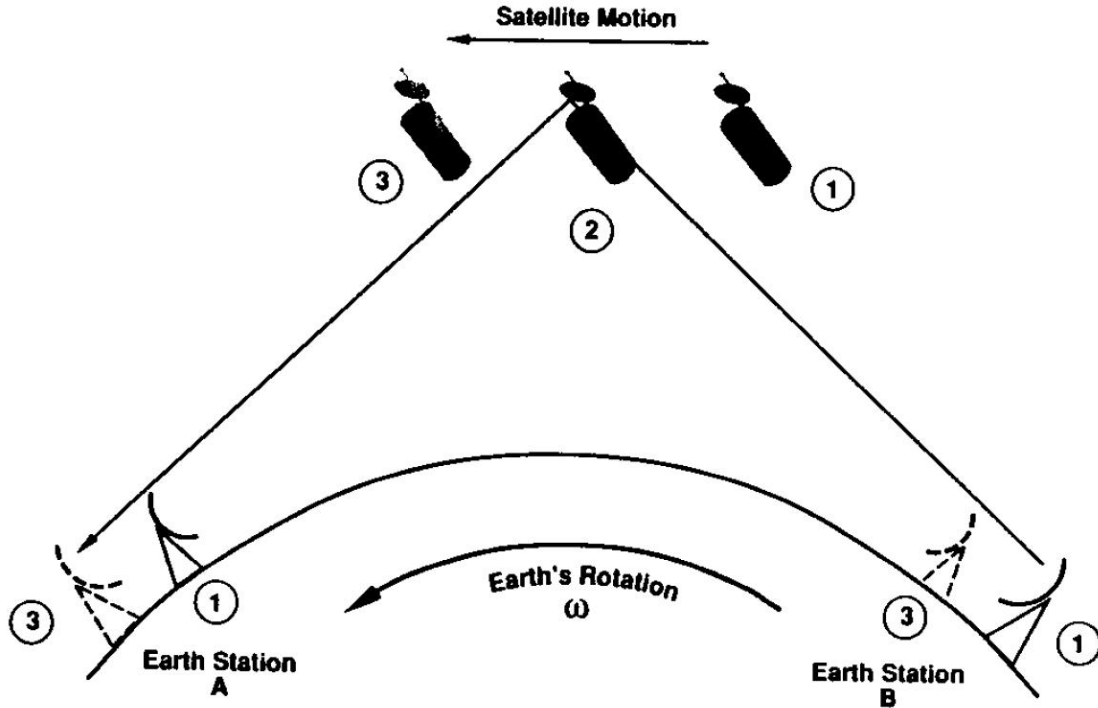


Figure 2.8: Demonstration of the Sagnac Delay: Earth's Rotation Produces Non-Reciprocity [13]

By adding all delays to the difference, the complete time interval measurement for each station can be stated in the following equations:

$$R(A) = A - B + d_{TB} + d_{BS} + d_{SBA} + d_{SA} + d_{RA} + S_{AB} \quad (2.2)$$

$$R(B) = B - A + d_{TA} + d_{AS} + d_{SAB} + d_{SB} + d_{RB} + S_{BA} \quad (2.3)$$

where

$R(A)$ = time interval counter reading for Station A

$R(B)$ = time interval counter reading for Station B

S_{AB} = Sagnac delay from Station A to Station B

S_{BA} = Sagnac delay from Station B to Station A

A = time of Clock A

B = time of Clock B

All other variables are the same as Figure 2.7

Differencing Equations 2.2 and 2.3, as seen in Figure 2.9, produces the expanded Two-Way Time Transfer equation.

$A - B = \frac{R(A) - R(B)}{2}$	Time Interval Counter Readings
$- \frac{d_{TB} \cdot d_{RB}}{2} + \frac{d_{TA} \cdot d_{RA}}{2}$	Earth Station Equipment
$+ \frac{d_{AS} \cdot d_{SA}}{2} - \frac{d_{BS} \cdot d_{SB}}{2}$	Propagation
$+ \frac{d_{SAB} \cdot d_{SBA}}{2}$	Delay in Satellite
$- \frac{2\omega A_r}{C^2}$	Earth's Rotation

Figure 2.9: The Two-Way Time Transfer Equation [13]

In Figure 2.9,

C = speed of light

A_r = area enclosing the projection of the satellite onto the Earth's equatorial plane

ω = Earth rotation rate

In the case of static TWTT, the uplink and downlink propagation delays are essentially equal, thus $d_{SA} \approx d_{AS}$ and $d_{SB} \approx d_{BS}$. The difference in Sagnac delays ($S_{AB} - S_{BA}$) is constant for the static case of TWTT, and the transmitting and receiving delay for the Earth station equipment is equal, as is the satellite delay when routing a signal from Station A to Station B or Station B to Station A. These factors cause cancellation when the measurements are differenced, and the TWTT equation is reduced to:

$$A - B = \frac{1}{2} [R(A) - R(B) + S_{AB} - S_{BA}] \quad (2.4)$$

where

$R(A)$ = time interval counter reading for Station A

$R(B)$ = time interval counter reading for Station B

S_{AB} = Sagnac delay from Station A to Station B

S_{BA} = Sagnac delay from Station B to Station A
 A = time of Clock A
 B = time of Clock B

Great precision and accuracy can be achieved by using a geostationary satellite for comparing and synchronizing clocks in this manner. This accuracy is a result of many simplifications that occur in the process of calculating a time difference measurement using TWTT. Propagation delays that occur during uplink and downlink to and from the satellite are essentially equivocal, causing them to cancel. Sagnac effects can be accurately calculated without the need for precise information on clock locations and errors, further reducing complexity.

2.4.2 Dynamic TWTT

Dynamic TWTT is accomplished in the same fashion as static TWTT with the exception that one or more of the receivers is moving. The moving receiver(s) introduce motion-related errors that were not present in the static case, changing the TWTT time differencing equation. A dynamic TWTT configuration is illustrated in Figure 2.10.

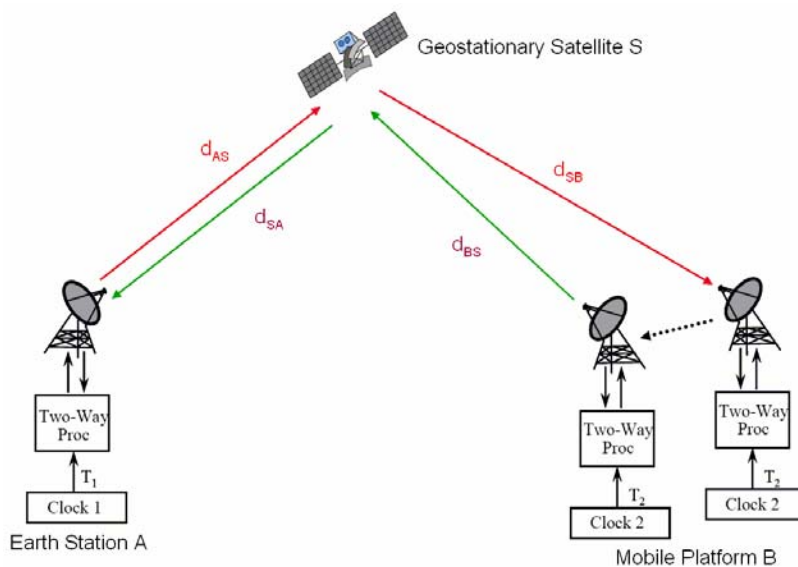


Figure 2.10: Dynamic Two-Way Time Transfer Using a Satellite [3]

Not all of the cancellations that applied to the static TWTT case transfer to the dynamic case. For the dynamic TWTT scenario in Figure 2.10, it can be assumed that $d_{AS} \approx d_{SA}$, since the geostationary satellite has no relative motion with respect to the earth station and the path length does not change. This replicates the situation in the static case. Unlike the static case, $d_{SB} \neq d_{BS}$ for the dynamic case, since the mobile platform has moved during the transmission of signals, causing the transmit and receive path lengths to be different between the geostationary satellite and mobile platform. Because the mobile platform is in motion, the Sagnac effect will also vary and produces a time-dependent value.

Taking all this into account, the time differenced measurement for dynamic TWTT becomes:

$$A - B = \frac{1}{2} [R(A) - R(B) - \Delta Propagation Delay + S_{AB} - S_{BA}] \quad (2.5)$$

where

$R(A)$ = time interval counter reading for Station A

$R(B)$ = time interval counter reading for Station B

S_{AB} = Sagnac delay from Station A to Station B

S_{BA} = Sagnac delay from Station B to Station A

A = time of Clock A

B = time of Clock B

$\Delta Propagation Delay$ = change in propagation delay over measurement interval

The $\Delta Propagation Delay$ term is a time-varying value that changes based on the relative motion of the mobile platform as well as how the velocity vector is projected onto the line of sight vector from the geostationary satellite. The Sagnac delay term (S_{AB}

– S_{BA}) is also time-varying, changing based on the absolute position of the two receivers and the velocity vector projected onto the equatorial plane [3].

2.5 Kalman Filter

A Kalman filter is a sequential filter that continuously improves the estimate of a state vector by sequentially incorporating new data measurements into the estimate as they become available [24]. A state vector can include data regarding position, velocity, acceleration, and any other pertinent information. A Kalman filter predicts the state in a future time epoch and then, upon reaching that new epoch, it uses collected measurements to correct the estimated state before predicting again to a new epoch. Kalman filters are able to compensate for ill-known or incompletely modeled dynamical systems [23] and are ideal for handling stochastic systems, such as navigation. This section uses the equations and descriptions provided in [22] for presenting a Kalman filter summary.

The Kalman filter is an iteration of time propagation and measurement incorporation [22]. It begins with an initial estimated state vector $\hat{\mathbf{x}}(t_0)$ and an initial estimated covariance $\mathbf{P}(t_0)$. The covariance matrix is a statistical measure of the accuracy of the state vector $\hat{\mathbf{x}}(t_0)$. In the next step the state $\hat{\mathbf{x}}(t_0)$ and covariance $\mathbf{P}(t_0)$ are predicted for the next epoch. These predictions are merely calculated and are not computed using measurement data. The Kalman filter uses Equations 2.6 and 2.7 to propagate the state and the covariance forward in time from t_{k-1}^+ to t_k^- . Using this notation, t_k and t_{k-1} refer to the times when measurements are incorporated and a

superscript plus sign (+) indicates the specified time is after measurement incorporation, while a superscript minus sign (-) indicates the specified time is before measurement incorporation.

$$\hat{\mathbf{x}}(t_k^-) = \Phi(t_k - t_{k-1})\hat{\mathbf{x}}(t_{k-1}^+) \quad (2.6)$$

$$\mathbf{P}(t_k^-) = \Phi(t_k - t_{k-1})\mathbf{P}(t_{k-1}^+)\Phi^T(t_k - t_{k-1}) + \mathbf{Q}_d \quad (2.7)$$

where

$\hat{\mathbf{x}}(t_{k-1}^+)$ = current state vector (before propagation)

$\hat{\mathbf{x}}(t_k^-)$ = state vector propagated to next epoch

$\mathbf{P}(t_{k-1}^+)$ = current covariance matrix (before propagation)

$\mathbf{P}(t_k^-)$ = covariance matrix propagated to next epoch

$\Phi(t_k - t_{k-1})$ = state transition matrix, which propagates the state and covariance forward in time

\mathbf{Q}_d = second moment of the process noise, which is the discrete time equivalent covariance associated with process noise that occurs when covariance \mathbf{P} is propagated through time [23]

Once the state vector and covariance matrix are propagated forward in time to the next epoch, real measurements are incorporated to correct any error that may have been introduced during propagation. The measurements must first be weighted properly before they can be incorporated into the estimated state and covariance. If the measurements are very poor, the filter must know to rely less on the collected data and depend more upon its own estimation of the state. Alternatively, if the measurements are very good, the filter must know to rely more heavily upon the collected data and depend less upon its own estimation of the state. This weighting factor is calculated using the Kalman gain, as seen in Equation 2.8.

$$\mathbf{K} = \mathbf{P}(t_k^-)\mathbf{H}^T[\mathbf{H}\mathbf{P}(t_k^-)\mathbf{H}^T + \mathbf{R}]^{-1} \quad (2.8)$$

where

\mathbf{K} = Kalman gain matrix

$\mathbf{P}(t_k^-)$ = covariance matrix propagated to next epoch (but before measurement incorporation)
 \mathbf{H} = observational partial derivative matrix, which relates the linearized observations (\mathbf{z}) to the estimated states (\mathbf{x})
 \mathbf{R} = measurement noise covariance matrix

Once the Kalman gain has been calculated, the state and covariance are updated by incorporating the measurement data. This process is illustrated in Equations 2.9 and 2.10.

$$\hat{\mathbf{x}}(t_k^+) = \hat{\mathbf{x}}(t_k^-) + \mathbf{K}[\mathbf{z} - \mathbf{H}\hat{\mathbf{x}}(t_k^-)] \quad (2.9)$$

$$\mathbf{P}(t_k^+) = \mathbf{P}(t_k^-) - \mathbf{KHP}(t_k^-) \quad (2.10)$$

where

\mathbf{z} = measurement vector

$\mathbf{z} - \mathbf{H}\hat{\mathbf{x}}(t_k^-) = \mathbf{r}$ = residual vector, which indicates how much error exists between the estimated state and the measurements (want residuals to be small, as it indicates the estimate is accurate)

At this point, the cycle repeats as the Kalman filter again propagates the state and covariance to the next epoch, incorporates collected measurements, and updates the state and covariance using the measurements. The Kalman filter loop is displayed in Figure 2.11 (using slightly different notation).

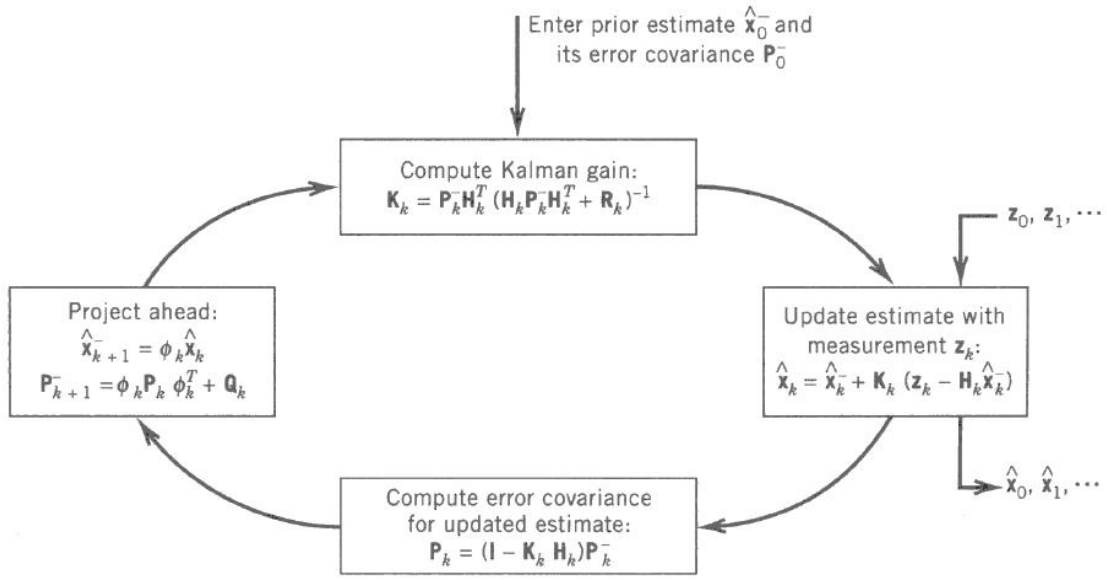


Figure 2.11: Kalman Filter Loop [7]

2.6 Summary

This chapter presented the relevant background information necessary for this research. Several key issues were explained, including the GPS system and pseudorange measurements, Earth-based reference coordinate systems, both static and dynamic Two-Way Time Transfer techniques, and the Kalman filter. Chapter 3 will describe the methodology of this research and how it used the background concepts explained in Chapter 2.

3 Methodology

3.1 Introduction

This chapter describes the methodologies and assumptions that were used to accomplish the research objectives described in Chapter 1. This research is based on a simulation created using MATLAB[®] and contains five main functions.

The first main function involves collecting desired input parameters from the user. The second function uses the input parameters to create truth data that will simulate the environment that is being measured. The third function uses the truth data to generate pseudorange and TWTT measurements for a geostationary satellite. The fourth function inputs the generated measurements into a Kalman filter and predicts the state of the satellite at each epoch in the simulation. The fifth and final function takes the results of the Kalman filter and compares them to the truth data to determine the accuracy of the filter.

3.2 Parameters

The simulation begins by collecting all the desired input values for a host of variables that will be used throughout the simulation. The list of input variables is described in the following sections. All the values in the parameters function are declared globally for use in all functions throughout the simulation.

3.2.1 Initial ECI State for Geostationary Satellite

The initial ECI state consists of X, Y, Z position and velocity values that describe the location of the satellite at the start of the simulation. This vector is nominally configured to place the satellite over the Prime Meridian (0 degrees longitude) at an altitude of 35,785.863 kilometers with an orbital velocity of 3.07466 km/s. The result is a circular geostationary orbit.

3.2.2 Simulation Run Time and Time Step Interval

The simulation run time is set for a single day. The time step interval denotes how often measurement data is collected by the satellite as it orbits and is set for 60 seconds. If a higher measurement resolution is desired, the time step can be shortened at the expense of a longer computation time.

3.2.3 Ephemeris Date Selection

As discussed in Chapter 2, the ephemeris describes the location of a satellite within its orbit. The ephemeris data for the GPS constellation may be chosen from any of ten possible days that were randomly selected from each year between 1997 and 2006. For simplicity in the model, each chosen day is a Sunday. GPS time is recorded in week seconds and resets at midnight every Sunday. By starting the simulation at midnight on Sunday, which is zero GPS week seconds, many complications can be avoided in the simulation code. These issues arise when attempting to keep track of the GPS week second time interval and initialize the time vector accordingly, making it much easier to always start at a time value of zero.

3.2.4 *GPS Measurement Model Selection*

Two models are available for generating GPS pseudorange measurements—a simple model and an advanced model. The simple model uses a constant cut-off angle between the GPS satellite and the Earth. As long as the Earth is not blocking the transmitted signal from the GPS satellite, it is received by the GEO satellite. The advanced model is more realistic, because it accounts for the antenna gain on the GPS satellite and the GEO satellite and includes the signal path loss that occurs as the signal travels through space. If the received power is below a specified threshold, the signal is considered too weak and cannot be used for generating pseudorange measurements.

The advanced GPS measurement model has additional parameters that can be adjusted. There are two gain patterns that can be used for the GPS satellite, simple and advanced. The simple gain pattern contains fewer values, ranging between 0-30 degrees off-boresight, and is based on data found in [19]. The advanced gain pattern has values from 0-180 degrees off-boresight and more realistically portrays an actual GPS antenna and is based on data found in [9]. The GEO satellite uses the gain pattern taken from the commercial patch antenna listed in [19], replicating actual flight hardware.

3.2.5 *Clock Type Selection*

The simulation has a choice of three clock types to use as the GEO satellite clock and as the TWTT reference clock. The possible clock oscillators include Rubidium, Cesium, and ovenized crystal. The clock parameters are taken from [14]. The Rubidium clock is the most precise and the ovenized crystal is the least precise. Ovenized crystal is an inexpensive and prolific type of clock oscillator and is the typical clock of choice built into current satellites.

3.2.6 Clock Model Parameters

In order to accurately predict how the clocks will propagate forward in time, certain parameters must be configured. The GEO satellite clock and TWTT reference clock are assigned an initial accuracy in bias and drift that is fed into the truth state propagator and the Kalman filter, allowing both propagators to model the clocks accurately. These initial values are standard deviations of the bias and drift error and will be multiplied by a random number and fed into the covariance matrix when starting the clock simulation.

3.2.7 Two-Way Time Transfer Parameters

The TWTT measurements are modeled to have a white Gaussian measurement noise error, expressed as a standard deviation. The TWTT measurement noise error is a result of signal degradation during transmission and in the hardware, affecting measurement accuracy, and will be held constant. The values used were 10, 3, 0.3, 0.03, and 0.003 meters for this simulation.

3.2.8 Kalman Filter Parameters

The Kalman filter contains initialization values that are used in the covariance matrix for predicting the level of measurement accuracy. The initial accuracy in the position and velocity measurements are provided to the filter when it starts. There is also a process noise value, expressed as a standard deviation, which is a degradation of the measurement signal as it travels through the associated hardware, reducing accuracy.

3.2.9 On/Off and Selection Flags

Numerous naturally-occurring errors are built into the simulation model that can be turned on or off. The on/off flags enable or disable clock errors in the GEO satellite and/or TWTT reference clock, measurement noise errors in the pseudorange and/or TWTT measurements, hardware-related process noise errors, and initial state errors in the Kalman filter.

The selection flags allow the user to choose different modeling options in the simulation. The GPS measurement model includes a simple and advanced model, and the TWTT measurement model includes two choices: using no TWTT measurements and using TWTT measurements where the reference clock has a drift rate that does not coincide with GPS time.

3.2.10 Monte Carlo Parameters

The simulation is equipped to handle Monte Carlo simulation, involving multiple iterations of the simulation with different random numbers. Monte Carlo simulation is a statistical analysis that strives to provide enough data, through repetition and random inputs, to accurately represent the stochastic characteristics of the model. In this simulation, Monte Carlo simulation is turned on or off with a flag, and the total number of iterations is defined by the user.

3.2.11 Constants

This simulation uses many constant values throughout the various sub-functions. These constants include the speed of light, the radius of the Earth, the radius of a GPS orbit, the frequency of the GPS L1 signal, nominal transmit power of a GPS antenna, the

gravitation parameter of the Earth, and the rotation rate of the Earth. To eliminate chance for error, the sub-functions reference all constants from a single global location, as opposed to being declared in each sub-function that requires the value.

3.3 Truth Model

The truth model function is responsible for generating all data that will be considered as the absolute truth. There are three main sections in this function: propagating the geostationary satellite state forward over a specified time interval, calculating the positions and clock states for each GPS satellite during that time interval, and modeling clock errors.

3.3.1 Propagate Geostationary Satellite State

Implementation of a simple Kalman filter propagates the GEO satellite state vector into the future. The initial state vector $\hat{\mathbf{x}}(t_0)$ is provided along with an initial covariance matrix $\mathbf{P}(t_0)$ and a dynamics matrix $\mathbf{F}(t_0)$. As explained previously, the covariance matrix describes the accuracy of the state vector values, and the dynamics matrix explains the motion of the state vector.

The GEO satellite state vector contains six values, displayed in Equation 3.1, where X, Y, Z are the position values and $\dot{X}, \dot{Y}, \dot{Z}$ are the velocity values.

$$\hat{\mathbf{x}} = \begin{bmatrix} X \\ Y \\ Z \\ \dot{X} \\ \dot{Y} \\ \dot{Z} \end{bmatrix} \quad (3.1)$$

The dynamics matrix describes the motion of the GEO satellite, which is a circular orbit, and is in a continuous form. The dynamics matrix is constructed to satisfy the relationship described in Equation 3.2.

$$\dot{\mathbf{x}} = \mathbf{F}\mathbf{x} \quad (3.2)$$

The orbital acceleration for a two-body circular orbit is calculated by using Equation 3.3. This expression is needed to find the time derivative of the orbital velocity, which is needed to build the relationship indicated in Equation 3.2.

$$\hat{\mathbf{a}} = -\frac{\mu}{r^3} \hat{\mathbf{x}} \quad (3.3)$$

where

$$\begin{aligned} \hat{\mathbf{a}} &= \text{orbital acceleration vector} \\ \mu &= \text{Earth gravitational constant} \\ r &= \sqrt{X^2 + Y^2 + Z^2} = \text{orbital radius} \\ \hat{\mathbf{x}} &= \text{orbital position vector} \end{aligned}$$

Using Equation 3.3, a list of relationships is formulated for use in creating the dynamics matrix. The list of relationships is shown in Equation 3.4, where

$$\begin{bmatrix} X & Y & Z & \dot{X} & \dot{Y} & \dot{Z} \end{bmatrix}^T = \begin{bmatrix} x_1 & x_2 & x_3 & x_4 & x_5 & x_6 \end{bmatrix}^T.$$

$$\begin{aligned} \dot{x}_1 &= x_4 \\ \dot{x}_2 &= x_5 \\ \dot{x}_3 &= x_6 \\ \dot{x}_4 &= -\frac{\mu}{r^3} x_1 \\ \dot{x}_5 &= -\frac{\mu}{r^3} x_2 \\ \dot{x}_6 &= -\frac{\mu}{r^3} x_3 \end{aligned} \quad (3.4)$$

Using Equation 3.4, Equation 3.2 can be written in expanded form as:

$$\begin{bmatrix} \dot{x}_1 \\ \dot{x}_2 \\ \dot{x}_3 \\ \dot{x}_4 \\ \dot{x}_5 \\ \dot{x}_6 \end{bmatrix} = \begin{bmatrix} 0 & 0 & 0 & 1 & 0 & 0 \\ 0 & 0 & 0 & 0 & 1 & 0 \\ 0 & 0 & 0 & 0 & 0 & 1 \\ -\frac{\mu}{r^3} & 0 & 0 & 0 & 0 & 0 \\ 0 & -\frac{\mu}{r^3} & 0 & 0 & 0 & 0 \\ 0 & 0 & -\frac{\mu}{r^3} & 0 & 0 & 0 \end{bmatrix} \begin{bmatrix} x_1 \\ x_2 \\ x_3 \\ x_4 \\ x_5 \\ x_6 \end{bmatrix} \quad (3.5)$$

For ease in a computer simulation, the continuous form equation must be converted to a discrete-time equation [22]. This conversion takes the dynamics matrix \mathbf{F} and turns it into the state transition matrix $\mathbf{\Phi}$, as shown in Equation 3.6.

$$\mathbf{\Phi} = e^{\mathbf{F}\Delta t} \quad (3.6)$$

where

$$\Delta t = t_{k+1} - t_k = \text{time interval}$$

A similar conversion must take place for the covariance matrix \mathbf{Q} to ensure it is also in a discrete-time form. Shown below, the continuous \mathbf{Q} matrix represents process noise being added to the acceleration terms to account for unmodeled orbit perturbations.

$$\mathbf{Q} = \begin{bmatrix} 0 & 0 & 0 & 0 & 0 & 0 \\ 0 & 0 & 0 & 0 & 0 & 0 \\ 0 & 0 & 0 & 0 & 0 & 0 \\ 0 & 0 & 0 & \sigma_n^2 & 0 & 0 \\ 0 & 0 & 0 & 0 & \sigma_n^2 & 0 \\ 0 & 0 & 0 & 0 & 0 & \sigma_n^2 \end{bmatrix} \quad (3.7)$$

Using Equation 3.8, the continuous \mathbf{Q} becomes the discrete-time \mathbf{Q}_d . The \mathbf{Q}_d matrix will be used when introducing process noise.

$$\mathbf{Q}_d = \int_0^{\Delta t} \mathbf{\Phi}(\tau) \mathbf{Q} \mathbf{\Phi}^T(\tau) d\tau \quad (3.8)$$

The next step is to propagate the state to the next time interval by using Equation 3.9.

$$\mathbf{x}(t_k^-) = \mathbf{\Phi}(t_k - t_{k-1})\hat{\mathbf{x}}(t_{k-1}^+) \quad (3.9)$$

If process noise is to be included in the propagation, correlated randomized white noise must be introduced to Equation 3.9. This is achieved by using the U-D factorization algorithm (explained in [7]) on the \mathbf{Q}_d matrix, which will provide the correlation factor. The decomposition of \mathbf{Q}_d into \mathbf{U} and \mathbf{D} is illustrated in Equation 3.10.

$$\mathbf{Q}_d = \mathbf{U}\mathbf{D}\mathbf{U}^T \quad (3.10)$$

where

\mathbf{U} = composed of elements along major diagonal of \mathbf{Q}_d , the nontrivial elements in upper triangular part of \mathbf{Q}_d , zeros elsewhere

\mathbf{D} = composed of elements in major diagonal \mathbf{Q}_d , zeros elsewhere

By multiplying the U-D factorization results with a 6 x 1 vector of random numbers generated by MATLAB[®], the result is a 6 x 1 vector \mathbf{w}_d of correlated randomized white noise values that correspond with the positions and velocities in the state vector $\hat{\mathbf{x}}$. This process is described in Equation 3.11.

$$\mathbf{w}_d = \mathbf{U}\sqrt{\mathbf{D}}\mathbf{n} \quad (3.11)$$

where

\mathbf{w}_d = 6 x 1 vector of correlated white noise

\mathbf{n} = 6 x 1 vector of random numbers

If so desired, process noise can be included in the state propagation by using Equation 3.12. Inclusion of process noise is selected by using a flag in the parameters function. It was always selected, except for initial simulation debugging.

$$\mathbf{x}(t_k^-) = \mathbf{\Phi}(t_k - t_{k-1})\hat{\mathbf{x}}(t_{k-1}^+) + \mathbf{w}_d \quad (3.12)$$

3.3.2 Calculate GPS Satellite Positions and Clock States

After propagating the GEO satellite state vector forward in time over the entire simulation time interval, the truth model function then calculates the positions and clock states of each individual GPS satellite over the entire simulation time interval. This information is stored for use in the generated measurements function.

There are two sets of ephemeris data, broadcast and precise. As described in Chapter 2, the broadcast ephemeris is a prediction of the orbital parameters for the GPS satellites, while the precise ephemeris is a calculation of the orbital parameters using collected measurement data. The broadcast ephemeris is used by a GPS receiver to calculate a navigation solution, while the precise ephemeris contains two-week-old data and can only be used for post-processing. In this simulation, the precise ephemeris is used to calculate the true position and clock state of each GPS satellites, while the broadcast ephemeris is used when generating simulated measurements.

3.3.3 Clock Model

GPS depends upon highly accurate atomic clocks that can provide synchronization between the satellites and receiver. Synchronization occurs through estimating the time offset, drift, and drift rate of the receiver clock relative to GPS time. To ensure the simulation accurately represents real clocks, the clock model must replicate the performance of atomic clocks. This sub-section closely follows the descriptions given in [8] and [25].

GPS satellites use Rubidium and Cesium atomic clocks to maintain accurate GPS time. In addition to these clock types, ovenized crystal will also be modeled for use on

the GEO satellite. Ovenized crystal is a very common clock found on satellites that do not require the extremely precise time measurements used in navigation.

The performance of atomic clocks can be simulated using a three-state polynomial process driven by white noise. The discrete process model and its covariance can be written as [6]:

$$\Phi(\tau) = \begin{bmatrix} 1 & \tau & \frac{1}{2}\tau^2 \\ 0 & 1 & \tau \\ 0 & 0 & 1 \end{bmatrix} \quad (3.13)$$

$$\begin{bmatrix} x_1(t_{k+1}) \\ x_2(t_{k+1}) \\ x_3(t_{k+1}) \end{bmatrix} = \begin{bmatrix} 1 & \tau & \frac{1}{2}\tau^2 \\ 0 & 1 & \tau \\ 0 & 0 & 1 \end{bmatrix} \begin{bmatrix} x_1(t_k) \\ x_2(t_k) \\ x_3(t_k) \end{bmatrix} + \begin{bmatrix} w_1(k) \\ w_2(k) \\ w_3(k) \end{bmatrix} \quad (3.14)$$

$$\mathbf{Q}_d(\tau) = E[w(k)w(k)^T] = \begin{bmatrix} q_1\tau + \frac{1}{2}q_2\tau^3 + \frac{1}{20}q_3\tau^5 & \frac{1}{2}q_2\tau^2 + \frac{1}{8}q_3\tau^4 & \frac{1}{6}q_3\tau^3 \\ \frac{1}{2}q_2\tau^2 + \frac{1}{8}q_3\tau^4 & q_2\tau + \frac{1}{3}q_3\tau^3 & \frac{1}{2}q_3\tau^2 \\ \frac{1}{6}q_3\tau^2 & \frac{1}{2}q_3\tau^2 & q_3\tau \end{bmatrix} \quad (3.15)$$

where

$x_1(t_k)$ and $x_1(t_{k+1})$ = clock bias error at times t_k and t_{k+1}

$x_2(t_k)$ and $x_2(t_{k+1})$ = clock drift error at times t_k and t_{k+1}

$x_3(t_k)$ and $x_3(t_{k+1})$ = clock drift rate error at times t_k and t_{k+1}

$\tau = t_{k+1} - t_k$ = time interval

$w_1(k)$, $w_2(k)$, and $w_3(k)$ = independent white noises

q_1 , q_2 , q_3 = continuous process noise power spectral densities representing the bias, drift, and drift rate

$\Phi(\tau)$ = state transition matrix propagating current clock bias, drift, and drift rate errors forward in time from t_k to t_{k+1}

$\mathbf{Q}_d(\tau)$ = discrete-time process noise covariance matrix

The clocks cannot be modeled deterministically because of their stochastic nature. Instead, the performance of the random walk noise values (w_1 , w_2 , w_3) is modeled and the characteristic Allan Variance curves of the atomic frequency standards are matched [7]. An example of a three-state random clock process is illustrated in Figure 3.1. A best fit

curve drawn through the plot shows how the three-state atomic clock performance is quadratic in nature. The statistics of the random walk noise values are determined by the values of the variance elements (q_1, q_2, q_3) of \mathbf{Q}_d in Equation 3.15 [5].

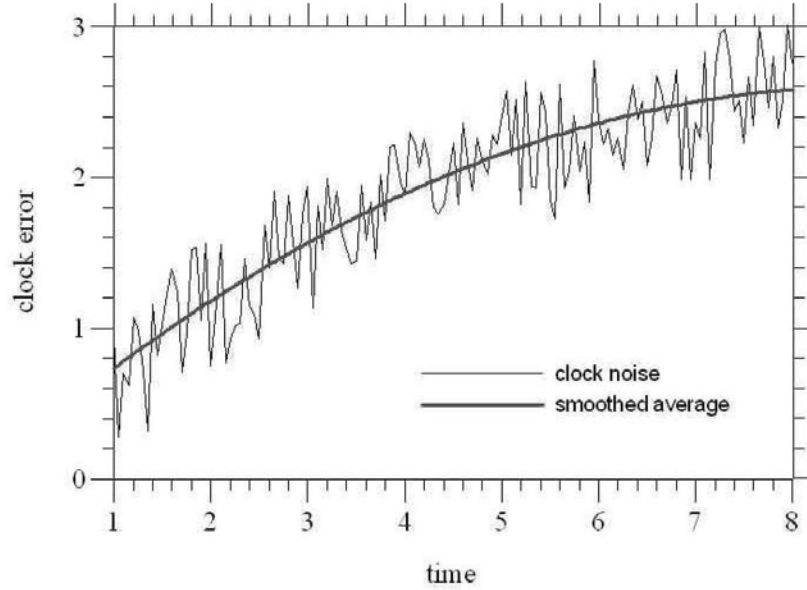


Figure 3.1: Comparison of Simulated Clock Error and Quadratic Fit [5]

The q values for this simulation were chosen by leveraging research conducted in the Clock Improvement Initiative [14] and are displayed in Table 3.1. To calculate a clock's three-state random process in the simulation, initial clock bias, drift, and drift rate values are selected from Table 3.1 and then propagated using Equation 3.14. The \mathbf{Q}_d from Equation 3.15 was used to generate properly correlated w_1 , w_2 , and w_3 terms using the UD factorization technique described in Equations 3.10 and 3.11.

Table 3.1: Process Noise Values for Atomic Clocks

	Rubidium Clock	Cesium Clock	Ovenized Crystal Clock
q_1 (bias)	$1.11 \times 10^{-22} \text{ s}^2/\text{s}$	$4.44 \times 10^{-22} \text{ s}^2/\text{s}$	$1.6 \times 10^{-21} \text{ s}^2/\text{s}$
q_2 (drift)	$2.22 \times 10^{-32} \text{ s}^2/\text{s}^3$	$3.33 \times 10^{-32} \text{ s}^2/\text{s}^3$	$16\pi^2 \times 10^{-23} \text{ s}^2/\text{s}^3$
q_3 (drift rate)	$6.66 \times 10^{-45} \text{ s}^2/\text{s}^5$	$0 \text{ s}^2/\text{s}^5$	$0 \text{ s}^2/\text{s}^5$

When using a three-state model, a value of zero for the q_3 term creates a singularity. To prevent this, a value of $1 \times 10^{-100} \text{ s}^2/\text{s}^5$ is used in the simulation instead of zero. This value is sufficiently small enough to represent zero while also being large enough to prevent a singularity from occurring.

3.4 Generated Measurements

The measurement generation function is responsible for creating pseudorange measurements by using the information supplied by the truth generation function. The pseudorange measurements can be calculated using a simple or an advanced GPS measurement model.

3.4.1 Pseudorange Measurements

Pseudorange values are normalized range measurements with the addition of errors due to pseudorange measurement noise, GPS satellite clock bias, and receiver clock bias. The pseudorange equation is:

$$\rho = \sqrt{(x^{sat} - x_{rec})^2 + (y^{sat} - y_{rec})^2 + (z^{sat} - z_{rec})^2} + c\delta t_{rec} - c\delta t^{sat} + v_{PR} \quad (3.16)$$

where

$x^{sat}, y^{sat}, z^{sat}$ = true ECEF position of the satellite (meters)

$x_{rec}, y_{rec}, z_{rec}$ = true ECEF position of the receiver (meters)

δt_{rec} = receiver clock bias (seconds)

δt^{sat} = satellite clock bias (seconds)

v_{PR} = pseudorange error (meters)

c = speed of light (meters/second)

The simulation allows various errors to be turned on and off, so the pseudorange is calculated in stages to produce more efficient code. Initially, the pseudorange measurement is the exact distance between the GPS satellite and the GEO satellite, as is

described by the square root value in Equation 3.16. If no errors were turned on, this would be the final output of the pseudorange generation.

The next step is to determine which errors are turned on, and add each error value incrementally. If all errors are turned on in the simulation, then the final output of the pseudorange generation would match Equation 3.16. The receiver and GPS satellite clock errors are generated in the truth model and would be incorporated into the pseudorange measurement if their on/off flags were turned on in the parameters function.

The measurement generation function has two models for simulating the pseudorange measurements. The simple model is very rudimentary and is computationally less expensive, while the advanced model is much more realistic.

3.4.2 Simple GPS Measurement Model

The simple GPS measurement model uses distinct cut-off angles for determining satellite visibility and does not include the side lobes of the GPS transmit antenna. The minimum cut-off angle is where the Earth occludes the GPS signal, and the maximum cut-off angle is where the GPS antenna no longer transmits. Figure 3.2 illustrates the simple measurement model.

The ionosphere extends to about 400 kilometers above the Earth's surface and will bend the GPS signals, creating errors in the pseudorange measurement. For this reason, the Earth's surface cannot be used as the occlusion for the GPS signals, since any signals that come close to the Earth's surface will be distorted and erroneous. Ionospheric errors can be corrected and removed, but this simulation does not use such methods. For simplicity, the ionosphere boundary is considered opaque, and any signals

that pass through it are ignored. In a sense, it is like extending the radius of the Earth by 400 kilometers.

The nominal beamwidth of a Block II/IIA GPS satellite antenna is approximately 42.6° [1], which equates to a 21.3° off-nadir look angle. This value becomes the maximum look angle for the GPS satellite, as seen in Figure 3.2.

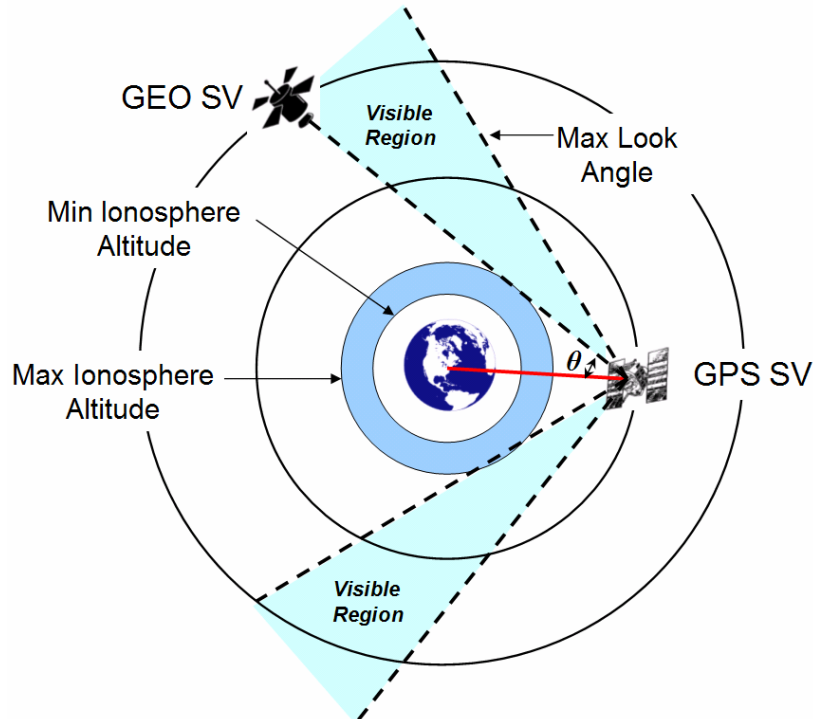


Figure 3.2: Simple GPS Measurement Model Diagram (not to scale)

The simple GPS measurement model produces a pseudorange measurement for a given GPS satellite only if the GEO satellite falls within the visible region seen in Figure 3.2. Signal power is not modeled and it is assumed that line-of-sight visibility guarantees a pseudorange measurement. The standard deviation of the pseudorange measurement noise error is constant, set at five meters. If the pseudorange measurement noise error is not turned on in the simulation, the pseudorange value is the exact distance between the GEO and GPS satellites.

3.4.3 Advanced GPS Measurement Model

The advanced GPS measurement model is much more robust than the simple model, taking into account the individual antenna gain patterns of each satellite to determine the received signal strength. It then uses the received signal strength to calculate the value of the pseudorange measurement noise error, which is taken from a table of values. The minimum cut-off angle imposed by the upper ionosphere is still in effect. The advanced GPS measurement model is illustrated in Figure 3.3

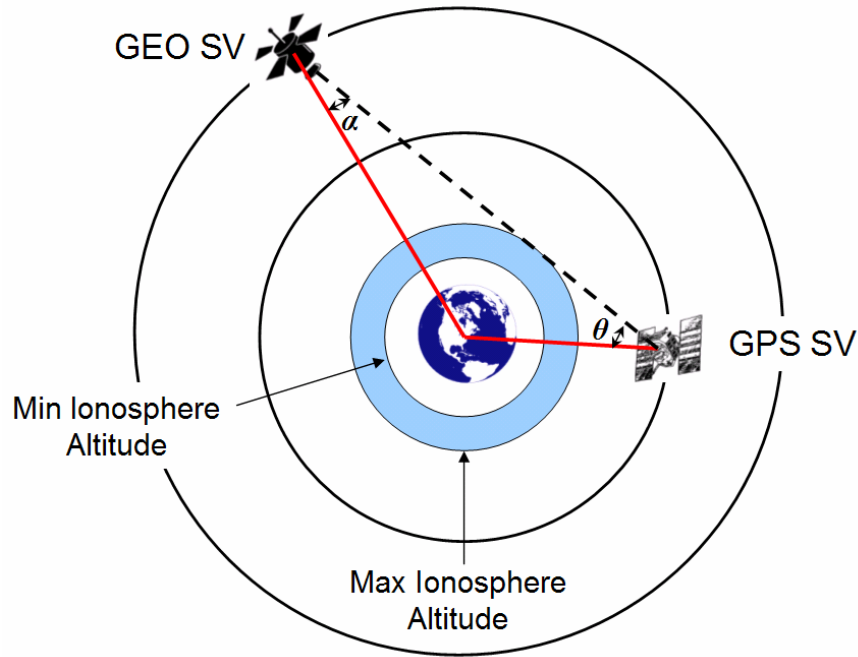


Figure 3.3: Advanced GPS Measurement Model Diagram (not to scale)

To determine the strength of the GPS signal that is received by the GEO satellite, the satellite nadir look angles are needed. If the GEO satellite and GPS satellite positions are known, simple vector math will produce the angles θ and α (referenced in Figure 3.3), which are the GPS satellite look angle and GEO satellite look angle, respectively. The calculated look angles are then used with antenna gain pattern information to determine the received signal strength. By knowing the look angle, it is a simple measure of tracing

the plot to find the corresponding antenna gain. This is accomplished for both the GPS satellite and the GEO satellite.

An antenna gain pattern plot can be created in a laboratory by making measurements on an antenna and recording the signal strength at various horizontal look angles. This simulation uses either a simple or advanced GPS antenna gain pattern plot, both based on the Block II/IIA GPS satellites. For the GEO satellite antenna, the simulation uses an antenna gain pattern plot taken from a commercial patch antenna that is currently used on spacecraft.

The simple GPS satellite antenna gain pattern plot includes the primary signal lobe and the secondary lobe, as seen in Figure 3.4, and drops off at approximately 43° from nadir.

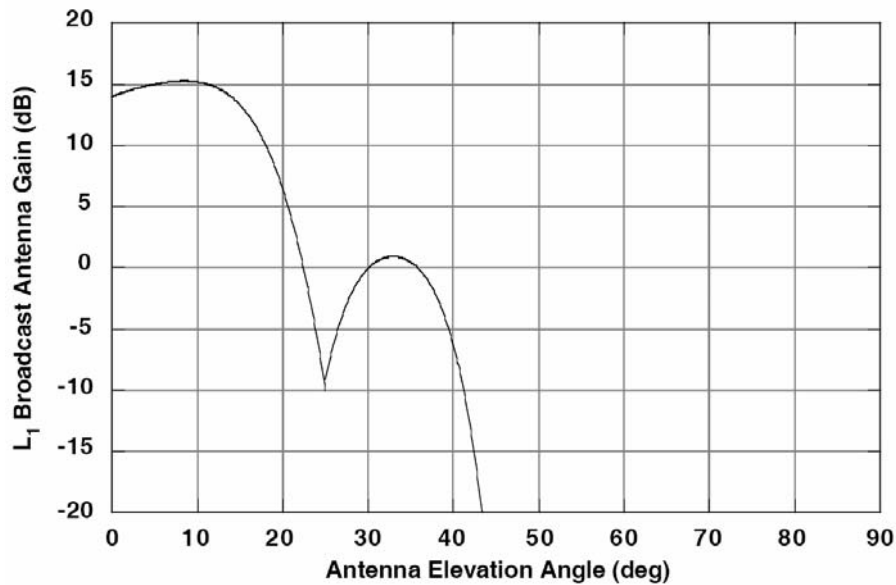


Figure 3.4: Simple GPS Antenna Gain Pattern Plot [19]

The advanced GPS antenna gain pattern plot, shown in Figure 3.5, includes the primary and secondary lobes, as well as additional information all the way out to 180° from nadir. A gain pattern is not necessarily symmetrical, but, for simplicity in this

simulation, it is assumed that the gain pattern does not change with varying vertical angles. Similar GPS broadcast antenna gain pattern data is located in [4] and [11].

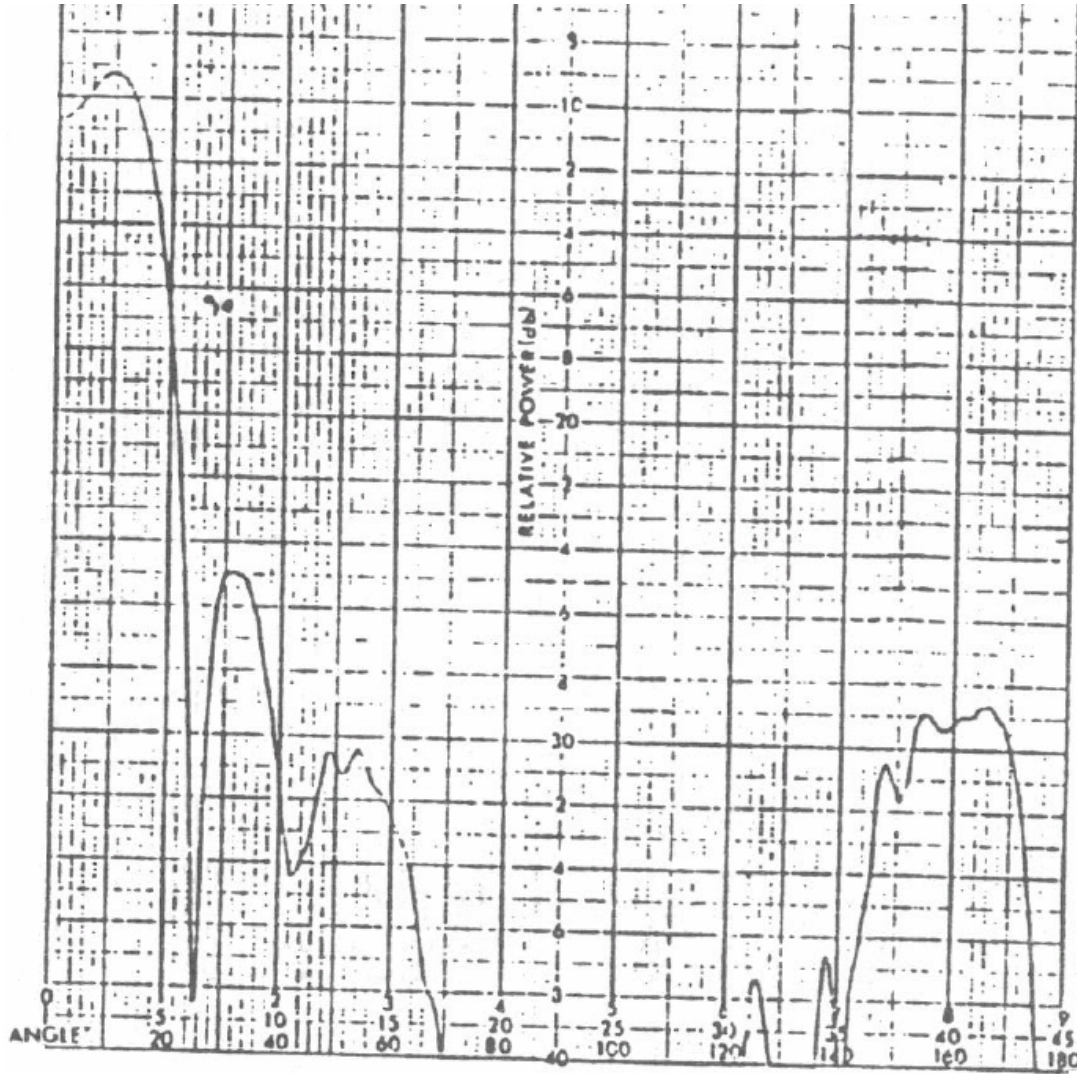


Figure 3.5: Advanced GPS Antenna Gain Pattern Plot [9]

The GEO satellite uses the gain pattern from a patch antenna that flew aboard the Falcon Gold experiment, designed by students at the Air Force Academy [19]. This particular antenna is representative of hardware that has flown on previous satellites. The antenna gain pattern plot is illustrated in Figure 3.6.

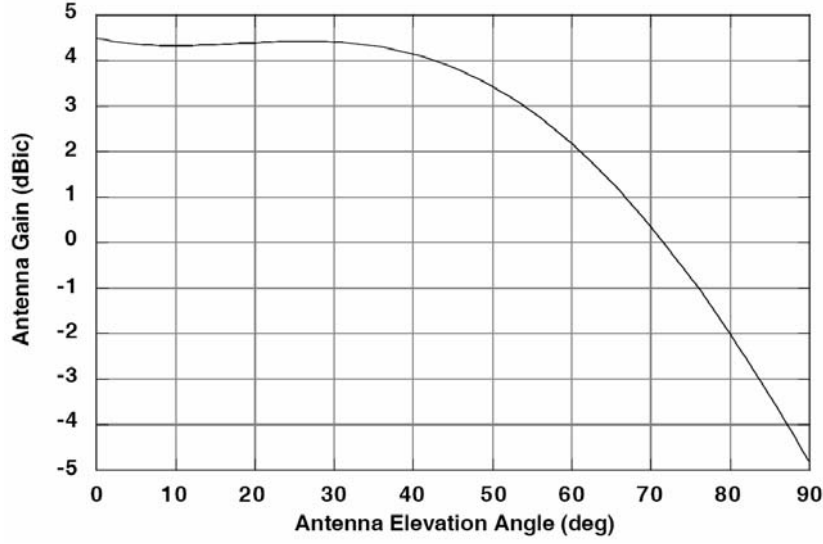


Figure 3.6: Patch Antenna Gain Pattern Plot [19]

The received power can be calculated by using the transmit and receive antenna gains, the transmit power, the distance between the transmit and receive antennas, and the wavelength of the transmitted signal. The resulting equation is listed below in standard and decibel format [16].

$$P_s = \frac{P_T G_T G_R}{4\pi R^2} \frac{\lambda^2}{4\pi} \quad (3.17)$$

$$P_{s,dB} = P_{T,dB} + G_{T,dB} + G_{R,dB} - 20 \log_{10} R - 22 + 2\lambda_{dB} \quad (3.18)$$

where

P_s = received signal power (Watts)

P_T = signal power at transmit antenna

G_T = transmit antenna gain

G_R = receive antenna gain

R = distance between transmit and receive antennas

λ = signal wavelength (GPS L1 wavelength ≈ 5.255 meters)

The resulting value is the signal power at the exit of the receiver antenna. All hardware has an associated noise value which must be subtracted from the received power when the signal is processed. The final value is referred to as C/N_0 (also written as P_s/N_0), which is the carrier to noise density, where N_0 is the noise density. This

simulation uses a standard N_0 value of 202 decibel-Watts [16], which is subtracted from Equation 3.18 to produce the final C/N_0 value.

Once the received signal strength has been calculated, the pseudorange measurement noise error can be established. The pseudorange measurement noise error values are developed in a laboratory setting by testing the operating hardware, and vary between GPS receivers. The data is compiled into a table of corresponding signal strengths, as illustrated in Figure 3.7. This plot is expressed in received power and not C/N_0 . By subtracting N_0 (-202 dBW) from the signal strength values listed, the C/N_0 values can be obtained. This plot is representative of an extremely high-sensitivity receiver. Similar C/N_0 data is located in [4].

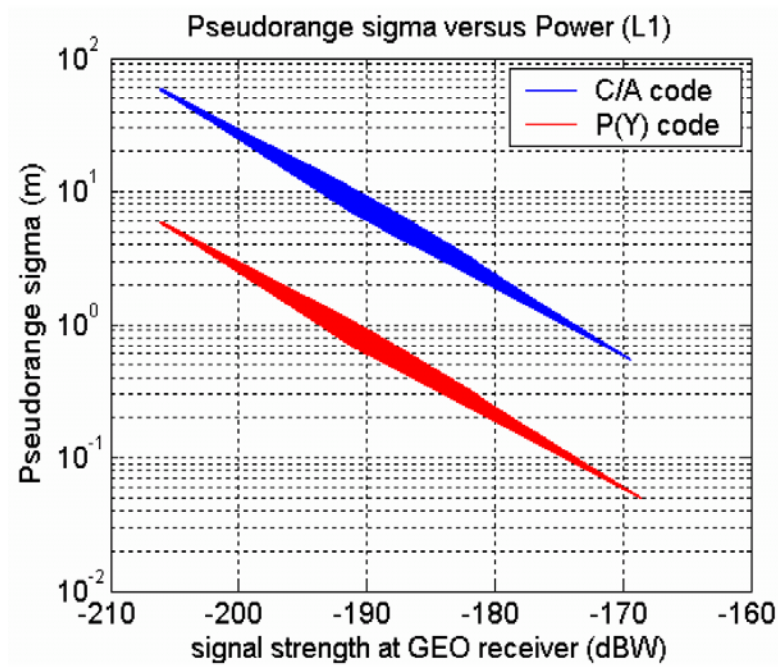


Figure 3.7: Pseudorange Measurement Noise Error Standard Deviation Plot [11]

The pseudorange measurement noise error value is given as a standard deviation, which is in turn multiplied by a MATLAB[®] random number, providing the measurement error that will be added to the pseudorange value. The pseudorange measurement noise

error can be turned on or off in the simulation. If the error is turned off, the pseudorange value will equal the exact distance between the GPS and GEO satellites, just as in the simple GPS measurement model.

3.4.4 TWTT Measurements

The Two-Way Time Transfer measurements in this simulation do not include Sagnac error or motion related errors, since they are largely deterministic and can be removed. The simulation could add the errors and then remove them, but it is a wasted step that will only increase computational cost and would have no added value. For simplicity, this simulation assumes that the propagation delays will cancel as in the static TWTT case. The resulting TWTT measurement equation is:

$$\begin{aligned}
 \Delta T &= \frac{1}{2} [TIC(GEO) - TIC(REF)] + \nu_{TWTT} \\
 &= \frac{1}{2} [2c\delta t_{GEO} - 2c\delta t_{REF}] + \nu_{TWTT} \\
 &= c\delta t_{GEO} - c\delta t_{REF} + \nu_{TWTT}
 \end{aligned} \tag{3.19}$$

where

- δt_{GEO} = GEO satellite clock error
- δt_{REF} = reference clock error
- ν_{TWTT} = TWTT measurement error
- c = speed of light

If TWTT measurements are to be used in the simulation, they are given to the Kalman filter along with the pseudoranges for measurement incorporation. The TWTT measurement error can be turned on and off, using values of 10, 3, 0.3, 0.03, and 0.003 meters.

3.5 Kalman Filter

A Kalman filter was chosen over a least squares batch filter, as was used in the research conducted in [8]. The Kalman filter allows for the use of new measurement data as it becomes available and easily allows for any stochastic processes, such as clock errors. The least squares estimation algorithm can not use data as it is collected, requiring all information up front. It also is more difficult to model stochastic processes in a least squares estimator.

The Kalman filter has several initial values that govern the estimation algorithm. The filter must know the accuracy level of the incoming measurements and how much to trust in their positioning information, as well as the amount of process noise in the system.

3.5.1 Initial State Values

The first thing needed by the Kalman filter is an initial state, including position, velocity, and clock error. These initial values are gathered from the truth data, so that the filter will begin its estimation at the same initial point of the truth data. The state vector is given in Equation 3.20.

$$\hat{\mathbf{x}} = \begin{bmatrix} X & Y & Z & \dot{X} & \dot{Y} & \dot{Z} & c\delta t_{GEO} & c\delta \dot{t}_{GEO} & c\delta t_{ref} & c\delta \dot{t}_{ref} \end{bmatrix}^T \quad (3.20)$$

where

X, Y, Z = GEO satellite position components

$\dot{X}, \dot{Y}, \dot{Z}$ = GEO satellite velocity components

δt_{GEO} and $\delta \dot{t}_{GEO}$ = GEO satellite clock bias and clock drift

δt_{ref} and $\delta \dot{t}_{ref}$ = TWTT reference clock bias and clock drift

c = speed of light

If initial state error is turned on, a particular error standard deviation is multiplied by a random number and added to each initial value. The initial state error standard

deviations are listed in Table 3.2. These were considered reasonable values for the start of a simulation run.

Table 3.2: Initial State Error Standard Deviation Values

Initial State Value	Standard Deviation Value
Position	20 m
Velocity	0.01 m/s
Clock bias	14 m
Clock drift	20 m/s

The dynamics matrix \mathbf{F} describes the motion of the satellite, and is modeled using the same equations as the truth generation (see Equation 3.6). The Kalman filter \mathbf{F} matrix includes the clock terms, making it a 10 x 10 matrix, as seen below.

$$\dot{\mathbf{x}} = \mathbf{F}\mathbf{x} \quad (3.21)$$

$$\begin{bmatrix} \dot{X} \\ \dot{Y} \\ \dot{Z} \\ \ddot{X} \\ \ddot{Y} \\ \ddot{Z} \\ c\delta\dot{t}_{GEO} \\ c\delta\ddot{t}_{GEO} \\ c\delta\dot{t}_{ref} \\ c\delta\ddot{t}_{ref} \end{bmatrix} = \begin{bmatrix} 0 & 0 & 0 & 1 & 0 & 0 & 0 & 0 & 0 & 0 \\ 0 & 0 & 0 & 0 & 1 & 0 & 0 & 0 & 0 & 0 \\ 0 & 0 & 0 & 0 & 0 & 1 & 0 & 0 & 0 & 0 \\ -\frac{\mu}{r^3} & 0 & 0 & 0 & 0 & 0 & 0 & 0 & 0 & 0 \\ 0 & -\frac{\mu}{r^3} & 0 & 0 & 0 & 0 & 0 & 0 & 0 & 0 \\ 0 & 0 & -\frac{\mu}{r^3} & 0 & 0 & 0 & 0 & 0 & 0 & 0 \\ 0 & 0 & 0 & 0 & 0 & 0 & 0 & 1 & 0 & 0 \\ 0 & 0 & 0 & 0 & 0 & 0 & 0 & 0 & 0 & 0 \\ 0 & 0 & 0 & 0 & 0 & 0 & 0 & 0 & 0 & 1 \\ 0 & 0 & 0 & 0 & 0 & 0 & 0 & 0 & 0 & 0 \end{bmatrix} \begin{bmatrix} X \\ Y \\ Z \\ \dot{X} \\ \dot{Y} \\ \dot{Z} \\ c\delta t_{GEO} \\ c\delta\dot{t}_{GEO} \\ c\delta t_{ref} \\ c\delta\dot{t}_{ref} \end{bmatrix} \quad (3.22)$$

where

- X, Y, Z = GEO satellite position components
- $\dot{X}, \dot{Y}, \dot{Z}$ = GEO satellite velocity components
- $\ddot{X}, \ddot{Y}, \ddot{Z}$ = GEO satellite acceleration components
- δt_{GEO} , $\delta\dot{t}_{GEO}$, and $\delta\ddot{t}_{GEO}$ = GEO satellite clock bias, drift, and drift rate
- δt_{ref} , $\delta\dot{t}_{ref}$, and $\delta\ddot{t}_{ref}$ = TWTT reference clock bias, drift, and drift rate
- c = speed of light

Since the truth generation and Kalman filter use the same dynamics, they will produce the same results if all errors are turned off. This provides a method for quantitative error-checking of the code.

The initial covariance matrix \mathbf{P} describes the accuracy of the state vector, and will be updated as the filter iterates. The first six values along the diagonal are for the X, Y, Z position and velocity values. The last four values along the diagonal are for the clock bias and drift of the GEO satellite and TWTT reference clocks. The \mathbf{P} matrix uses the values shown in Table 3.2 and is described in Equation 3.23, where subscripts p = position, v = velocity, cb = clock bias, and cd = clock drift.

$$\mathbf{P}(t_0) = \begin{bmatrix} \sigma_p^2 & 0 & 0 & 0 & 0 & 0 & 0 & 0 & 0 & 0 \\ 0 & \sigma_p^2 & 0 & 0 & 0 & 0 & 0 & 0 & 0 & 0 \\ 0 & 0 & \sigma_p^2 & 0 & 0 & 0 & 0 & 0 & 0 & 0 \\ 0 & 0 & 0 & \sigma_v^2 & 0 & 0 & 0 & 0 & 0 & 0 \\ 0 & 0 & 0 & 0 & \sigma_v^2 & 0 & 0 & 0 & 0 & 0 \\ 0 & 0 & 0 & 0 & 0 & \sigma_v^2 & 0 & 0 & 0 & 0 \\ 0 & 0 & 0 & 0 & 0 & 0 & \sigma_{cb}^2 & 0 & 0 & 0 \\ 0 & 0 & 0 & 0 & 0 & 0 & 0 & \sigma_{cd}^2 & 0 & 0 \\ 0 & 0 & 0 & 0 & 0 & 0 & 0 & 0 & \sigma_{cb}^2 & 0 \\ 0 & 0 & 0 & 0 & 0 & 0 & 0 & 0 & 0 & \sigma_{cd}^2 \end{bmatrix} \quad (3.23)$$

The covariance matrix \mathbf{Q} describes the errors associated with propagating the state covariance matrix \mathbf{P} through time. The \mathbf{Q} matrix includes the process noise value of the GEO satellite and the related clock q values. The process noise value is equal to the process noise value used in the truth generation and the clock q values are taken from Table 3.1, depending upon the type of clocks that are used. Equation 3.24 describes the \mathbf{Q} matrix used in the Kalman filter, and it does not change throughout the simulation.

$$\mathbf{Q} = \begin{bmatrix} 0 & 0 & 0 & 0 & 0 & 0 & 0 & 0 & 0 & 0 \\ 0 & 0 & 0 & 0 & 0 & 0 & 0 & 0 & 0 & 0 \\ 0 & 0 & 0 & 0 & 0 & 0 & 0 & 0 & 0 & 0 \\ 0 & 0 & 0 & \sigma_n & 0 & 0 & 0 & 0 & 0 & 0 \\ 0 & 0 & 0 & 0 & \sigma_n & 0 & 0 & 0 & 0 & 0 \\ 0 & 0 & 0 & 0 & 0 & \sigma_n & 0 & 0 & 0 & 0 \\ 0 & 0 & 0 & 0 & 0 & 0 & cq_1(sv) & 0 & 0 & 0 \\ 0 & 0 & 0 & 0 & 0 & 0 & 0 & cq_2(sv) & 0 & 0 \\ 0 & 0 & 0 & 0 & 0 & 0 & 0 & 0 & cq_1(ref) & 0 \\ 0 & 0 & 0 & 0 & 0 & 0 & 0 & 0 & 0 & cq_2(ref) \end{bmatrix} \quad (3.24)$$

where

σ_n = GEO satellite process noise

$q_1(sv)$ = GEO satellite clock bias process noise

$q_2(sv)$ = GEO satellite clock drift process noise

$q_1(ref)$ = reference clock bias process noise

$q_2(ref)$ = reference clock drift process noise

c = speed of light

3.5.2 Filter Execution

Once the initial state vector, dynamics matrix, and covariance matrices are defined, the Kalman filter is ready to begin. The first step is to calculate the state transition matrix Φ by using the dynamics matrix F and the time interval Δt , shown in Equation 3.25.

$$\Phi = e^{F\Delta t} \quad (3.25)$$

The next step is to calculate \mathbf{Q}_d , the discrete time version of the continuous-form \mathbf{Q} matrix.

$$\mathbf{Q}_d = \int_0^{\Delta t} \Phi(\tau) \mathbf{Q} \Phi^T(\tau) d\tau \quad (3.26)$$

Next, the filter propagates the state and covariance, as seen below:

$$\mathbf{x}(t_k^-) = \Phi(t_k - t_{k-1})\hat{\mathbf{x}}(t_{k-1}^+) \quad (3.27)$$

$$\mathbf{P}(t_k^-) = \Phi(t_k - t_{k-1})\mathbf{P}(t_{k-1}^+)\Phi^T(t_k - t_{k-1}) + \mathbf{Q}_d \quad (3.28)$$

Measurement information for a Kalman filter must follow the equation listed below.

$$\mathbf{z}(t_i) = \mathbf{h}[\mathbf{x}(t_i), t_i] + \mathbf{v}(t_i) \quad (3.29)$$

where

$\mathbf{z}(t_i)$ = measurement vector at time t_i

$\mathbf{v}(t_i)$ = zero-mean white Gaussian vector process noise of strength \mathbf{R} ,
independent of process noise

The GPS pseudorange measurements are of the form:

$$\rho = \sqrt{(x^{sat} - x_{rec})^2 + (y^{sat} - y_{rec})^2 + (z^{sat} - z_{rec})^2} + c\delta t_{rec} - c\delta t^{sat} + v_{PR} \quad (3.30)$$

Combined with Equation 3.29, Equation 3.30 implies the following:

$$\mathbf{h}[\mathbf{x}(t_i), t_i] = \sqrt{(x^{sat} - x_{rec})^2 + (y^{sat} - y_{rec})^2 + (z^{sat} - z_{rec})^2} + c\delta t_{rec} - c\delta t^{sat} \quad (3.31)$$

After the \mathbf{h} vector equations are written, the observational partial derivative matrix \mathbf{H} is constructed. The \mathbf{H} matrix relates the linearized observations to the estimated states, and is expressed in Equation 3.32.

$$\mathbf{H} = \begin{bmatrix} H_1 \\ H_2 \\ \vdots \\ H_n \end{bmatrix} \quad (3.32)$$

where

$$H_1 = \frac{\delta h_1(\hat{\mathbf{x}})}{\delta \hat{\mathbf{x}}}, H_2 = \frac{\delta h_2(\hat{\mathbf{x}})}{\delta \hat{\mathbf{x}}}, \dots, H_n = \frac{\delta h_n(\hat{\mathbf{x}})}{\delta \hat{\mathbf{x}}} \quad (3.33)$$

$$\frac{\delta h_1(\hat{\mathbf{x}})}{\delta \hat{\mathbf{x}}} = \begin{bmatrix} \frac{\delta h_1(\hat{\mathbf{x}})}{\delta x_1} & \frac{\delta h_1(\hat{\mathbf{x}})}{\delta x_2} & \dots & \frac{\delta h_1(\hat{\mathbf{x}})}{\delta x_m} \end{bmatrix} \quad (3.34)$$

The \mathbf{H} matrix is of size n by m , where n is the number of collected measurements and m is the number of states in $\hat{\mathbf{x}}$ (in this simulation, $m = 10$). For example, if there are two pseudorange measurements and one TWTT measurement at a given epoch, the \mathbf{H} matrix and measurement vector \mathbf{z} will be:

$$\mathbf{H} = \begin{bmatrix} \mathbf{e}_x^1 & \mathbf{e}_y^1 & \mathbf{e}_z^1 & 0 & 0 & 0 & 1 & 0 & 0 & 0 \\ \mathbf{e}_x^2 & \mathbf{e}_y^2 & \mathbf{e}_z^2 & 0 & 0 & 0 & 1 & 0 & 0 & 0 \\ 0 & 0 & 0 & 0 & 0 & 0 & 1 & 0 & -1 & 0 \end{bmatrix} \quad (3.35)$$

$$\mathbf{z} = \begin{bmatrix} \rho_1 \\ \rho_2 \\ TWTT \end{bmatrix} \quad (3.36)$$

where

$$\begin{aligned} \mathbf{e}_x &= \frac{x_{rec} - x^{sat}}{\sqrt{(x^{sat} - x_{rec})^2 + (y^{sat} - y_{rec})^2 + (z^{sat} - z_{rec})^2}} \\ \mathbf{e}_y &= \frac{y_{rec} - y^{sat}}{\sqrt{(x^{sat} - x_{rec})^2 + (y^{sat} - y_{rec})^2 + (z^{sat} - z_{rec})^2}} \\ \mathbf{e}_z &= \frac{z_{rec} - z^{sat}}{\sqrt{(x^{sat} - x_{rec})^2 + (y^{sat} - y_{rec})^2 + (z^{sat} - z_{rec})^2}} \end{aligned}$$

The error term $\mathbf{v}(t_i)$ in the Kalman filter measurement equation is controlled by the covariance matrix \mathbf{R} . The \mathbf{R} matrix is specified for a given measurement vector. This means that each pseudorange measurement will have its own values in the \mathbf{R} matrix. The \mathbf{R} matrix is typically based upon expected error statistics, which is based upon knowledge of the system.

In the example given above, the corresponding \mathbf{R} matrix will be:

$$\mathbf{R} = \begin{bmatrix} \sigma_{PR1}^2 & 0 & 0 \\ 0 & \sigma_{PR2}^2 & 0 \\ 0 & 0 & \sigma_{TWT}^2 \end{bmatrix} \quad (3.37)$$

where

σ_{PR} = standard deviation value of pseudorange measurement noise

σ_{TWT} = standard deviation value of TWT measurement noise

It is now time for the filter to incorporate the measurements, involving several steps. The filter will calculate the residuals, compute the Kalman gain, and update the state and covariance.

The residuals are the difference between the predicted state and the observed state. Residuals are calculated using the following equation:

$$\mathbf{r} = \mathbf{z}(t_i) - \mathbf{h}(t_i) \quad (3.38)$$

The Kalman gain determines the weighting factor that is applied to the measurement data. The Kalman gain depends upon the covariance and will instruct the filter to trust the measurement data more or less, depending upon its accuracy. The Kalman gain calculation is listed below.

$$\mathbf{K} = \mathbf{P}(t_k^-) \mathbf{H}^T [\mathbf{H} \mathbf{P}(t_k^-) \mathbf{H}^T + \mathbf{R}]^{-1} \quad (3.39)$$

where

\mathbf{K} = Kalman gain matrix

$\mathbf{P}(t_k^-)$ = covariance matrix propagated to next epoch (but before measurement incorporation)

\mathbf{H} = observational partial derivative matrix, which relates the linearized observations (\mathbf{z}) to the estimated states (\mathbf{x})

\mathbf{R} = measurement noise covariance matrix

Now the Kalman gain can be used to update the state and covariance, using the following equations (stated previously in Chapter 2):

$$\hat{\mathbf{x}}(t_k^+) = \hat{\mathbf{x}}(t_k^-) + \mathbf{K} \left(\mathbf{z} - \mathbf{h} \left[\hat{\mathbf{x}}(t_k^-), t_k \right] \right) \quad (3.40)$$

$$\mathbf{P}(t_k^+) = \mathbf{P}(t_k^-) - \mathbf{K} \mathbf{H} \mathbf{P}(t_k^-) \quad (3.41)$$

Lastly, the filter updates the \mathbf{F} , Φ , and \mathbf{Q}_d matrices. In the new epoch, the GEO satellite will have a new radius, which changes the \mathbf{F} matrix. The new \mathbf{F} matrix will then change the Φ and \mathbf{Q}_d matrices using the same equations listed above.

Before starting the next iteration, the current filter information is saved into a history matrix. When the simulation is complete, the history matrix will contain the state, covariance, and residuals values for each epoch.

3.6 Results Analysis

Analyzing the simulation results involves comparing the Kalman filter estimated state with the true state. The analysis depends on the simulation type, being either a single run or a Monte Carlo collection of runs.

The most important result is the three-dimensional positioning error, which will be expressed as Mean Radial Spherical Error (MRSE). The MRSE is analogous to a three-dimensional Distance Root Mean Square (DRMS) value. For a Monte Carlo simulation, the MRSE for a particular epoch is calculated by using the following equation:

$$MRSE = \sqrt{\frac{\sum_{i=1}^n (x_i^2 + y_i^2 + z_i^2)}{n}} \quad (3.42)$$

where

n = number of simulation runs

$x_i = X_i^{true} - X_i^{filter}$ = difference of truth and filter X position for epoch i

$y_i = Y_i^{true} - Y_i^{filter}$ = difference of truth and filter Y position for epoch i

$z_i = Z_i^{true} - Z_i^{filter}$ = difference of truth and filter Z position for epoch i

The MRSE value can also be calculated by using the standard deviation values that exist in the covariance matrix for a particular epoch, as seen below.

$$MRSE = \sqrt{\frac{\sum_{i=1}^n (x_i^2 + y_i^2 + z_i^2)}{n}} \approx \sqrt{\sigma_x^2 + \sigma_y^2 + \sigma_z^2} \quad (3.43)$$

where

$\sigma_x, \sigma_y, \sigma_z$ = standard deviation values for the X, Y, Z coordinates

As the number of simulations n increases, the two square root values approach the same value. Using a Monte Carlo simulation, each run will generate different position values, but the filter-computed covariance values will be the same for every single run. As a result, the covariance standard deviation values from a single run can replace the position values from hundreds of runs in a Monte Carlo simulation.

To insure the covariance values are accurate and the equality assumption is true, the standard deviation values are first compared with a Monte Carlo simulation using a high number of runs. If the MRSE computed from the Monte Carlo simulation closely resembles the MRSE computed from the covariance values of a single run, the model is validated and only a single run is necessary to calculate the MRSE from that point on.

After the MRSE is calculated for each time epoch, the Root Mean Square (RMS) is calculated for the entire collection of epochs, using Equation 3.44. The final result is a single RMS value that depicts the level of error in the estimation filter.

$$RMS = \sqrt{\frac{\sum_{i=1}^n x_i^2}{n}} \quad (3.44)$$

where

n = number of epochs

x_i = MRSE for epoch i

3.7 Summary

This Chapter describes the five main functions of the simulation. The five functions include loading simulation parameters, generating truth data, generating measurement data, running a Kalman filter, and analyzing the results. Chapter 4 will discuss the results and analysis of the simulation.

4 Results and Analysis

4.1 Introduction

This chapter provides the simulation results and analyses. First, preliminary results are explained that will allow a better understanding of the simulation data. The baseline results are then described, giving a reference point from which to compare the results of each trade study. Five trade studies explore the effects of using GPS ephemeris data from different days, using a simple or complex GPS receiver model, using simple or complex antenna gain patterns, using different combinations of clock types in the receiver and TWTT reference clock, and varying the TWTT measurement noise error.

4.2 Preliminary Results

The primary purpose of this research is to explore the impact of using TWTT measurements on the positioning accuracy of GPS navigation in a geostationary orbit. As a first step in validating the simulation model, several Monte Carlo simulations were performed to analyze the statistical results and confirm the output was reasonable.

4.2.1 Graphical Results

The Monte Carlo simulations consisted of 100 iterations, and sample raw data is displayed in Figure 4.1. Each line represents the difference between the true position and the Kalman filter-predicted position over a single simulation run. Each simulation uses the same parameters but will utilize a different set of random numbers produced by the random number generator in MATLAB[®].

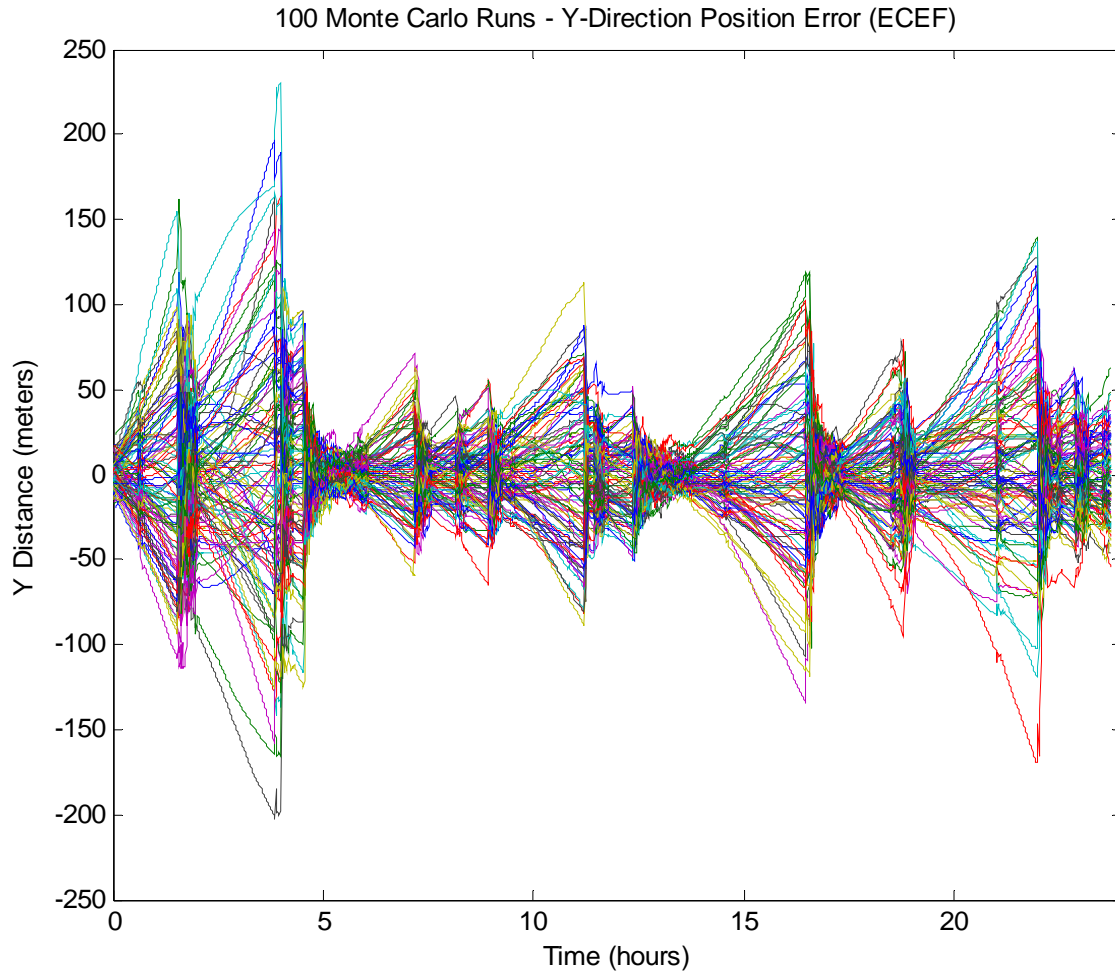


Figure 4.1: Monte Carlo Measurements vs Time for 100 Iterations (Standard GPS Receiver Sensitivity, no TWTT)

The Monte Carlo simulation results are more appropriately displayed by using the Monte Carlo mean, Monte Carlo mean plus/minus the Monte Carlo standard deviation, and the covariance calculated by the Kalman filter, as seen in Figure 4.2. The blue line represents the Monte Carlo mean value at each measurement epoch. Since the Monte Carlo simulation is composed of 100 iterations, each point on the blue line is the mean of 100 values. The dotted black lines represent the sum and difference of the Monte Carlo mean and the standard deviation of the Monte Carlo mean. The red lines represent the covariance values computed by the Kalman filter. As the number of simulation runs

approaches infinity, the plots of the Monte Carlo mean plus/minus the standard deviation should exactly match the plots of the filter-computed covariance.

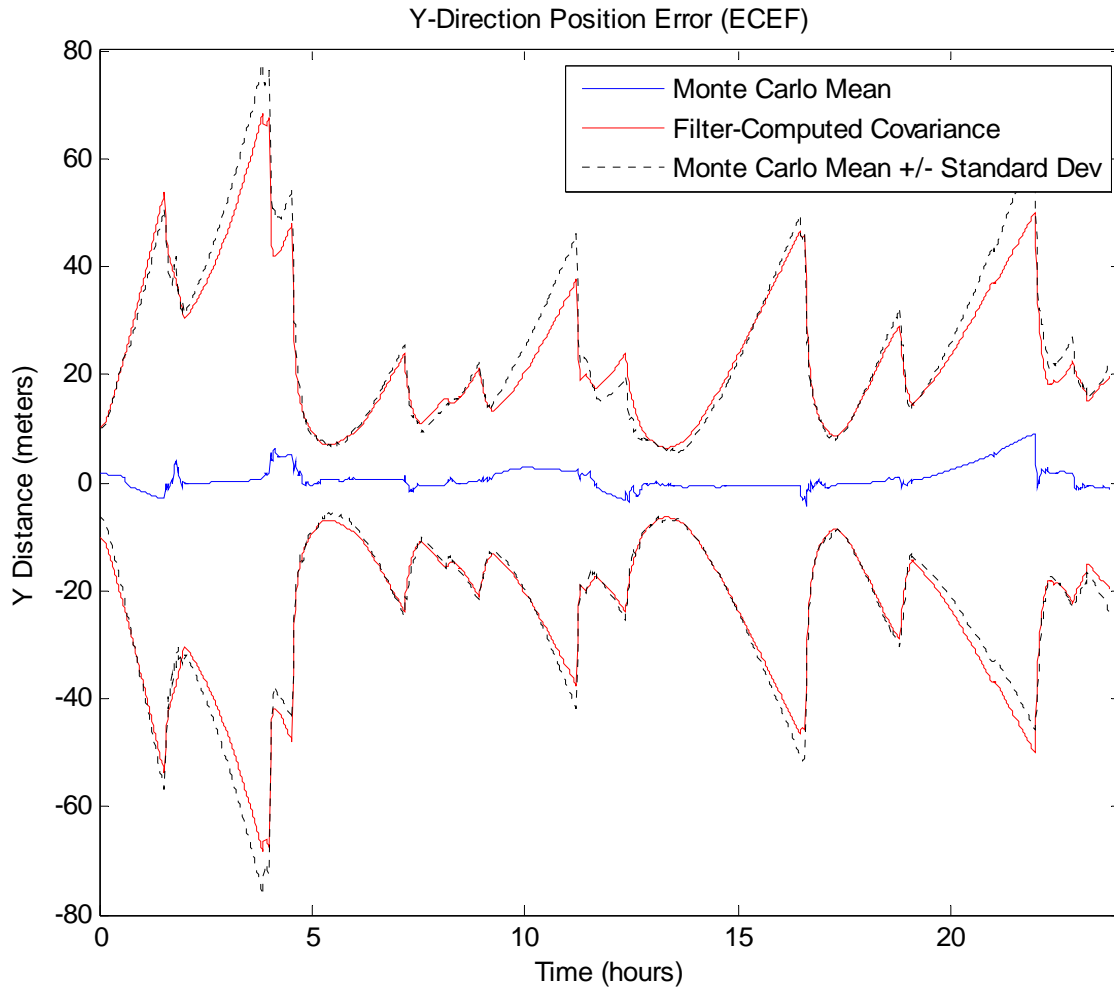


Figure 4.2: 100-Run Monte Carlo Measurement Mean, Measurement Standard Deviation, and Filter-Computed Covariance

The Monte Carlo standard deviation results closely match the filter-computed covariance results, indicating that the covariance analysis will be representative of the Monte Carlo simulation. Monte Carlo simulations that include TWTT measurements lead to the same conclusion as the non-TWTT case.

The original intent was to prove that covariance analysis is sufficient to analyze results by comparing covariance analysis results to Monte Carlo simulations. If single

runs are proved adequate, the massive computational time of numerous Monte Carlo runs can be avoided.

4.2.2 Root Mean Square Results

As explained in Section 3.6, the simulation results are provided in terms of Root Mean Square (RMS) positioning error. The RMS positioning error allows the results to be condensed into a single number, providing a quick and simple method for comparing trade study results.

RMS values are normally calculated from a collection of measurement data gathered from numerous simulations runs, such as a Monte Carlo simulation. Another method is to use the filter-computed covariance values calculated from a single simulation run, as opposed to the actual measurement data. As the number of Monte Carlo simulation runs approaches infinity, the RMS values calculated by using measurement data should equal the RMS values calculated by using covariance values. The filter-calculated covariance values will be the same for each simulation run, so Monte Carlo simulations are not required when using covariance values to calculate RMS values.

Two scenarios were selected to compare measurement-calculated RMS values with filter covariance-calculated RMS values. An ovenized crystal clock was assigned to the GEO satellite receiver while using two different GPS receiver sensitivity settings. The three-dimensional RMS results are displayed in Table 4.1. These two scenarios use GPS ephemeris data from January 1, 2006 and the complex GPS receiver model with complex antenna gain pattern data. These settings are the default for all the simulations unless otherwise specified.

Table 4.1: Comparison of Monte Carlo Simulation and Single Run Simulation, no TWTT

	<i>Standard Sensitivity (32 dB-Hz cutoff)</i>	<i>High Sensitivity (12 dB-Hz cutoff)</i>
Monte Carlo 3D RMS	83.90	3.88
Single Run 3D RMS	76.09	3.83
% Difference	10.26%	1.31%

Plotting the 3D position RMS values over time provides another useful way of comparing the Monte Carlo measurement values to the filter covariance values from a single run. If the filter is properly estimating the position of the GEO satellite, the filter-computed covariance 3D position RMS over time curve on the plot should match that of the Monte Carlo simulation. A plot of the 3D position RMS over time is shown in Figure 4.3.

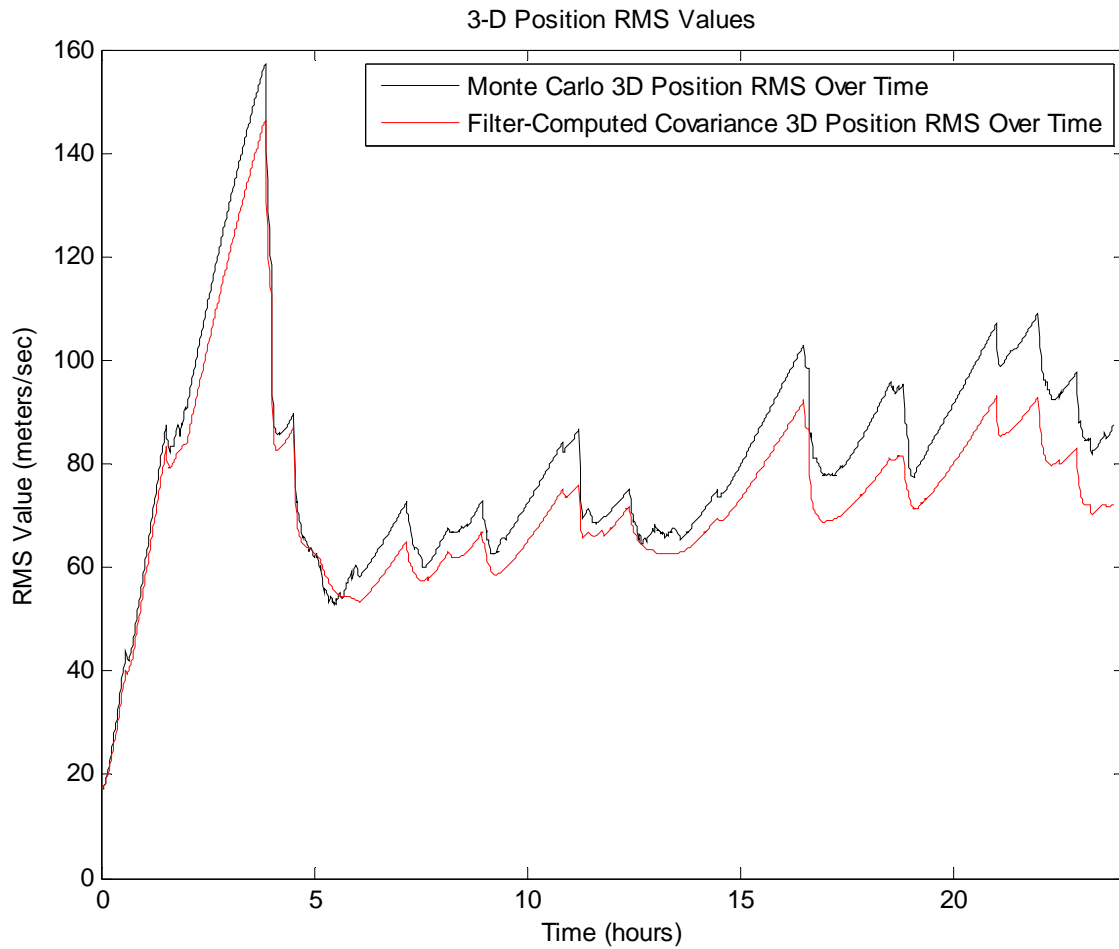


Figure 4.3: 3D Position RMS Over Time – Standard Sensitivity, no TWTT

The worst-case scenario is a standard sensitivity receiver with no TWTT measurements, displayed in Figure 4.3. In the simulation, the standard sensitivity receiver tracks between zero and four GPS satellites during a 24 hour period (see Appendix A), resulting in poor measurement precision. The lack of GPS signals is apparent when looking at the 3D RMS plot, where the measurements curve differs from the filter-computed covariance curve.

Since few measurements are available to the filter, it must rely heavily on estimating the satellite position. The covariance will predict how the position, velocity, and clock errors will propagate, but the lack of measurements will prevent the filter from

making consistent corrections to its estimation. This is what causes the disparity between the Monte Carlo results and the covariance results.

Since the Monte Carlo measurements closely match the filter-computed covariance values and carry the same trends, the model can be considered valid. The Monte Carlo measurement results can now be replaced with the covariance measurements from a single simulation run, producing enormous savings in computational time.

4.3 Baseline Results

A series of six scenarios were selected as the baseline for comparing against the trade study results. In the baseline analysis, an ovenized crystal clock is used for the GEO satellite GPS receiver and a Rubidium clock is used for the TWTT reference clock. All six GPS receiver sensitivity levels are used while switching the TWTT measurements on and off, resulting in twelve data sets. The GPS receiver sensitivity levels dictate the C/N_0 cutoff for the receiver's ability to detect and use a GPS signal, as well as the associated pseudorange error. The sensitivity levels range from 32 dB-Hz (standard) to 7 dB-Hz (ultra high) using 5 dB-Hz increments.

4.3.1 Plotting the Results

The plotted data provides a glimpse inside the simulation mechanics and helps to show that the model is valid. Certain trends are visible that point to tangible reasons for the nature of the data.

In situations where the receiver has a lower sensitivity, there will be periods of time when no GPS satellites are visible and the filter will need to rely completely upon its

process model estimating the state of the satellite. Over time, errors will propagate and the filter's prediction will diverge from the true position, as will the filter's confidence in the accuracy of the predicted position values. When a satellite comes into view, the filter will once again receive measurement data and can finally reduce the uncertainty. In the case of clock bias error, these rapid corrections are plainly visible in Figure 4.4. The blue line in Figure 4.4 represents the difference between the filter-predicted state and the true state, while the red line represents the filter-computed covariance. If the filter is accurate, the measurement values should stay within the boundaries of the covariance.

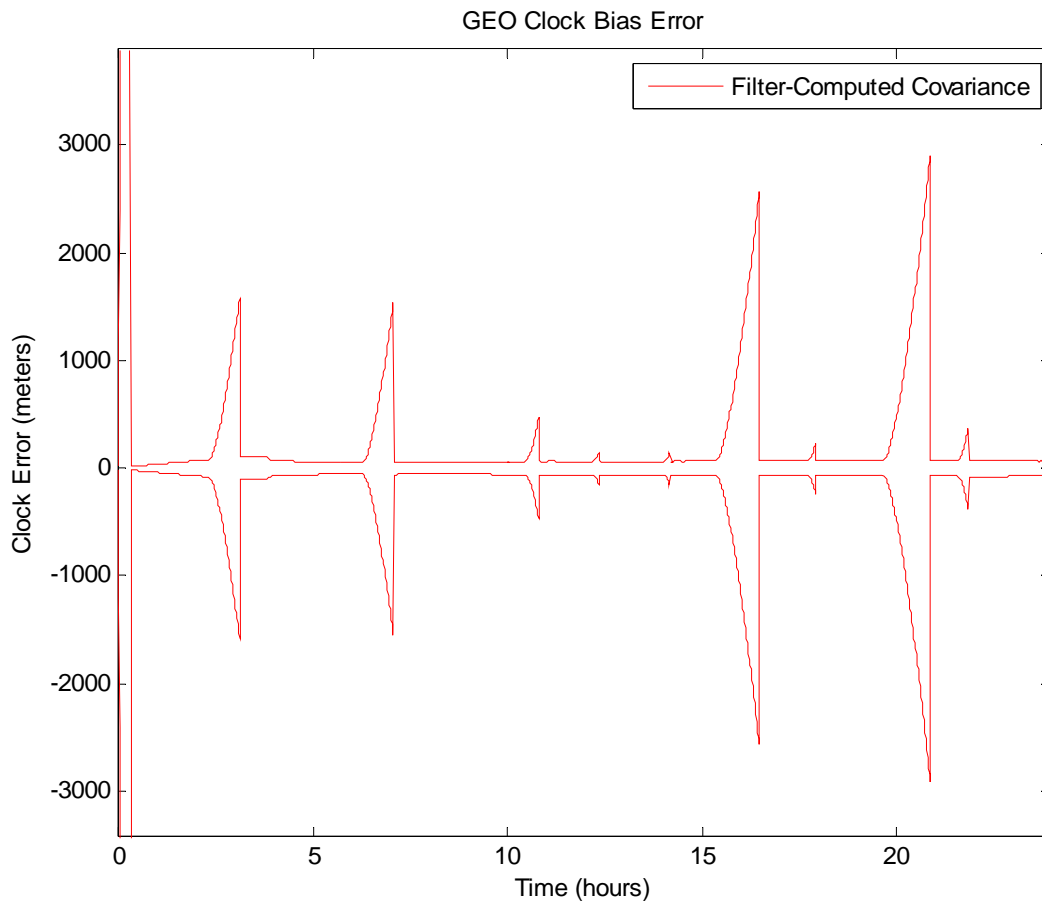


Figure 4.4: GEO Satellite Clock Bias Error Filter Covariance for a Single Run (Standard Sensitivity with no TWTT Measurements)

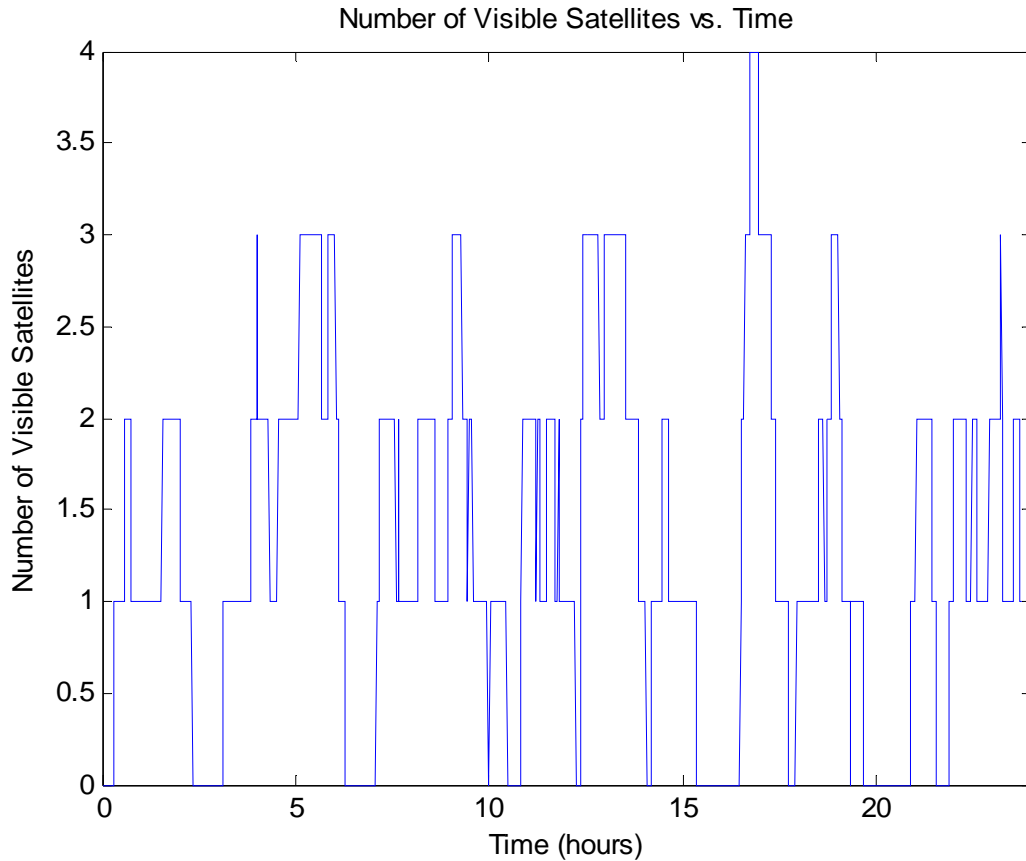


Figure 4.5: Visible GPS Satellites from GEO Satellite (Standard Sensitivity)

In Figure 4.4, the rapid covariance growth is directly linked to the periods where zero GPS satellites are visible. The filter-computed covariance of clock bias error grows when there are no available measurements, since the filter is continually losing confidence in the prediction. When measurements become available, the filter can immediately correct the prediction of the clock state, shrinking the covariance drastically as the filter is once again confident in the predicted clock state.

When TWTT measurements are included, the filter never relies solely on prediction for the clock state. The reference clock provides bias, drift, and drift rate information to the filter, allowing it to more accurately predict the velocity and position states. Figure 4.6 is based on exactly the same GPS satellite visibility as Figure 4.4, but

now includes TWTT measurements. The drastic jumps in the covariance disappear since the filter never experiences clock measurement blackouts.

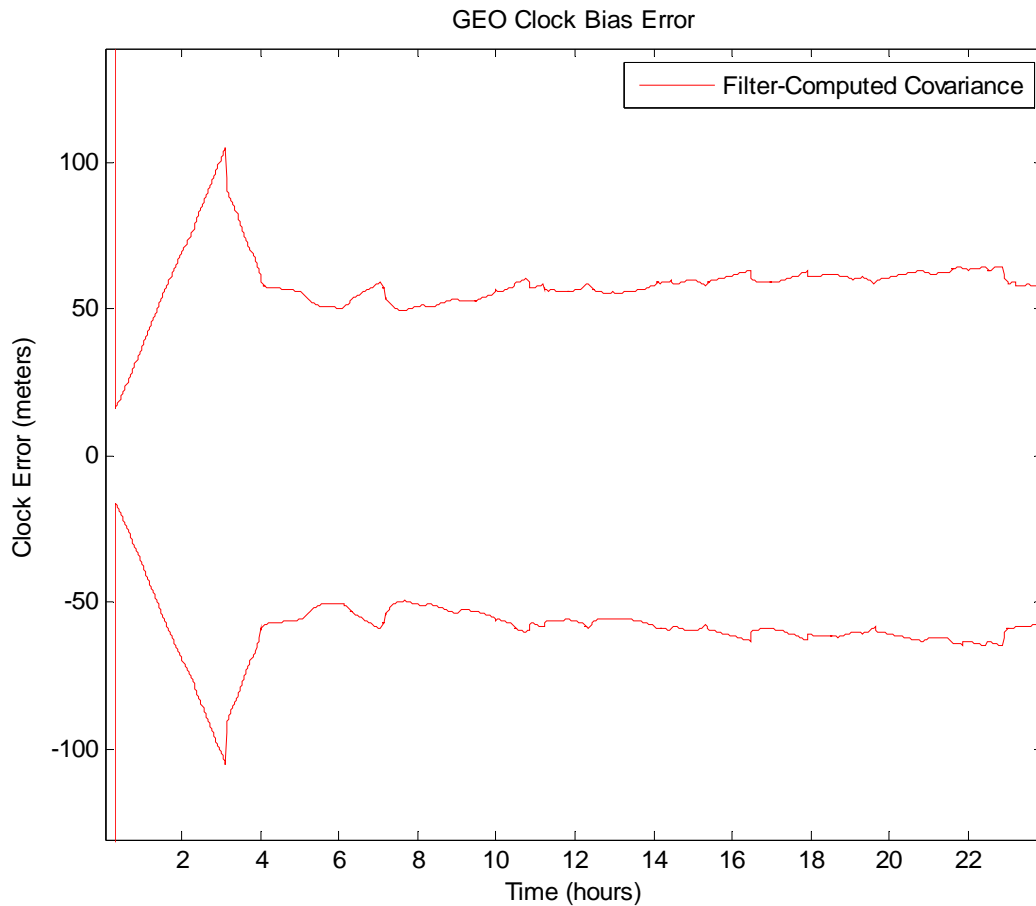


Figure 4.6: GEO Satellite Clock Bias Error Filter Covariance for a Single Run (Standard Sensitivity with TWTT Measurements Included)

When using a higher sensitivity receiver, the filter is able to more adequately correct the estimated state. Figure 4.7 illustrates the clock bias error of a medium sensitivity receiver with TWTT measurements turned on and off. The higher sensitivity receiver is able to track more GPS signals and allow the filter to predict the clock state more accurately than the receiver depicted in Figure 4.6. When TWTT measurements are included, the clock state prediction improves further and the covariance is smaller than the non-TWTT case.

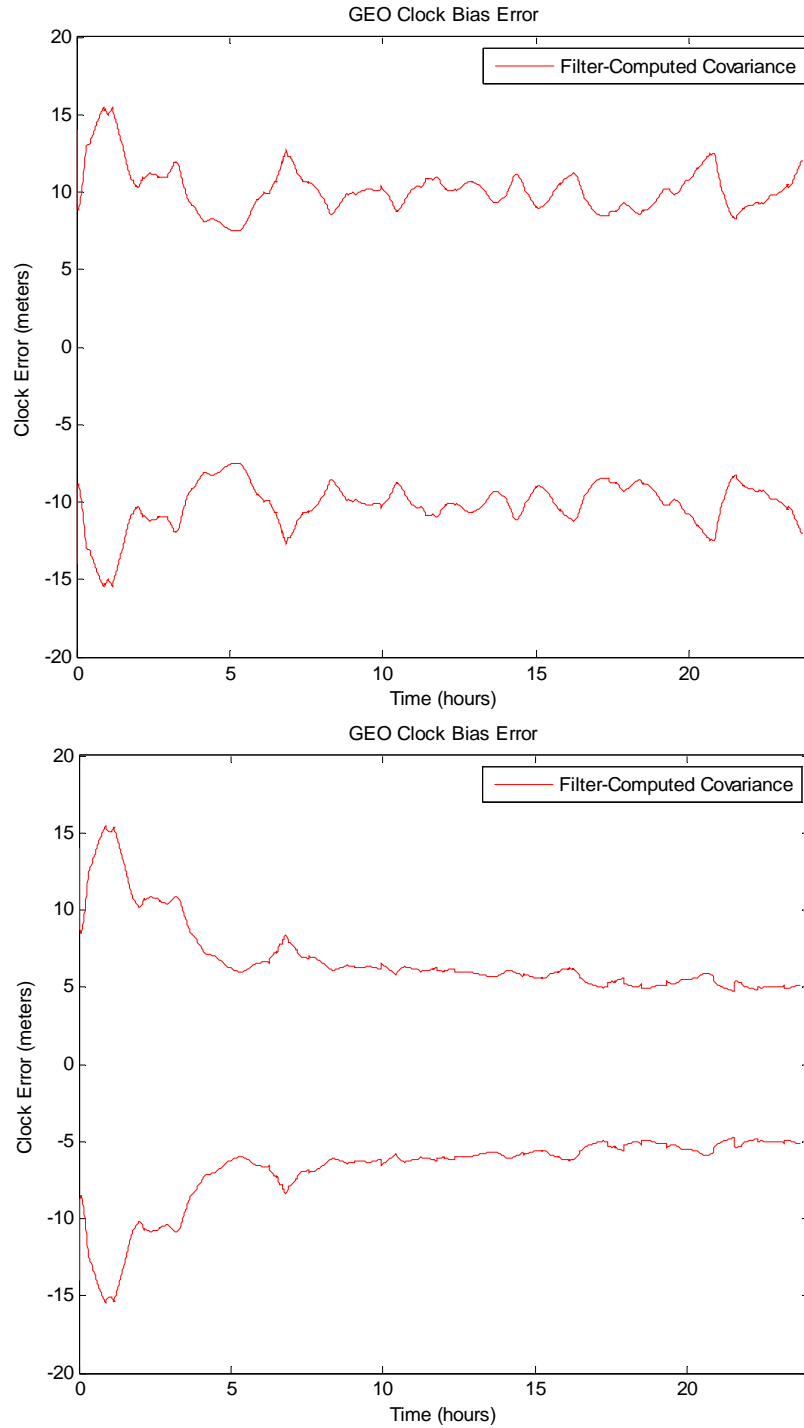


Figure 4.7: GEO Satellite Clock Bias Error with TWTT Turned Off (top) and On (bottom) (Medium Sensitivity)

A similar outcome is also apparent when looking at the position error. For example, the X-direction position error is shown in Figure 4.8.

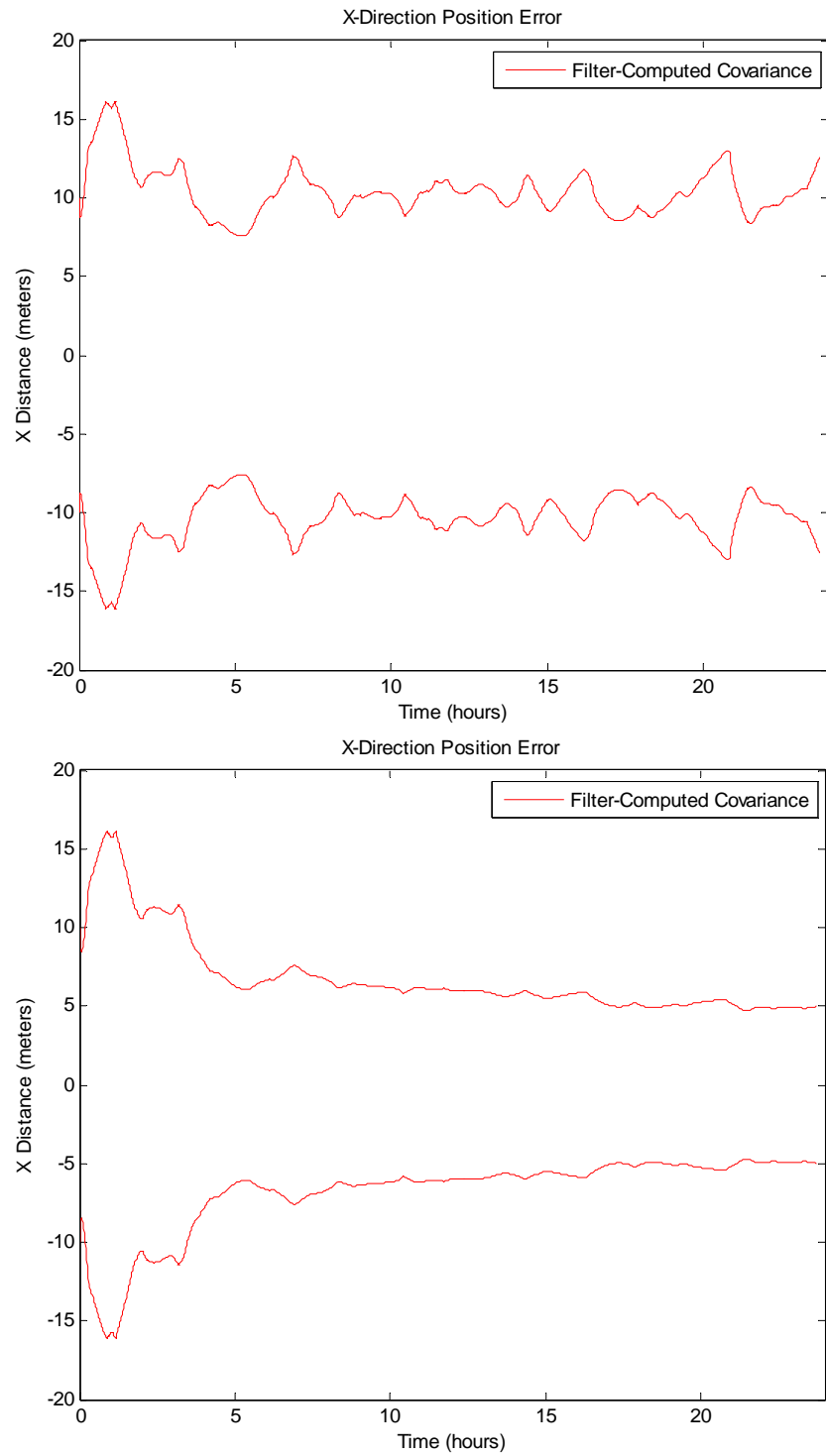


Figure 4.8: Geo Satellite X-Direction Position Error with TWTT Turned Off (top) and On (bottom) (Medium Sensitivity)

Plotting the simulation results can explain behaviors that would naturally be expected in the real-world system. By visually verifying these events in the data, the simulation model can be trusted with greater confidence.

4.3.2 Position Error

The compiled RMS position error data for the baseline case is listed in Table 4.2. The X, Y, and Z position errors are expressed as RMS values over time. For example, all the filter covariance X values over the entire simulation run time are squared and summed. This value is divided by the entire number of measurement epochs to calculate the mean of the squared values. The square root of the mean value results in the RMS value, condensing the entire simulation run into a single number for evaluation. After the initial state is declared, the simulation runs for 23 hours and 45 minutes with 60-second measurement intervals, resulting in 1,426 measurement values.

The three-dimensional RMS value, labeled 3D in Table 4.2, is calculated in a slightly different manner. When using Monte Carlo measurement data, the RMS values are calculated to find the three-dimensional position error for each measurement epoch (refer to Section 3.6). When using filter covariance values to calculate a three-dimensional position error, a root sum square (RSS) is used instead of the RMS (see Equation 3.43). All X, Y, and Z values are squared and summed and then the square root is calculated. The result is 1,426 RSS values that represent the three-dimensional position error for each epoch. In order to reduce this data into a single number for comparison, the RMS value of all the RSS values is calculated, providing the single number to describe the three-dimensional position error.

Table 4.2: Simulation Baseline Results – RMS Position Error Values per Receiver Sensitivities

GPS Receiver Sensitivity	Cutoff (dB-Hz)	RMS Position Type	RMS Position Error (m)		% Decrease in Position Error by Using TWTT
			<i>no TWTT</i>	<i>Rb TWTT</i>	
Standard	32	3D	76.09	60.32	20.73%
		X (Radial)	66.44	55.49	16.48%
		Y (In-track)	27.69	17.60	36.43%
		Z (Cross-track)	24.68	15.78	36.06%
Standard Plus	27	3D	31.87	24.10	24.36%
		X (Radial)	30.19	22.32	26.07%
		Y (In-track)	8.10	6.97	14.02%
		Z (Cross-track)	6.18	5.85	5.40%
Medium	22	3D	11.34	7.71	32.04%
		X (Radial)	10.54	6.56	37.76%
		Y (In-track)	3.11	2.97	4.41%
		Z (Cross-track)	2.80	2.74	1.97%
Medium Plus	17	3D	6.32	4.08	35.43%
		X (Radial)	5.87	3.38	42.49%
		Y (In-track)	1.70	1.66	2.38%
		Z (Cross-track)	1.60	1.58	1.09%
High	12	3D	3.83	2.40	37.43%
		X (Radial)	3.56	1.95	45.15%
		Y (In-track)	1.02	1.00	1.65%
		Z (Cross-track)	0.97	0.96	0.83%
Ultra High	7	3D	2.36	1.48	37.55%
		X (Radial)	2.19	1.18	46.14%
		Y (In-track)	0.65	0.64	1.18%
		Z (Cross-track)	0.63	0.62	0.68%

4.4 Trade Study 1: Ephemeris Date

To ensure the simulation does not depend upon the ephemeris data for a specific day, nine additional days were selected for comparison. One day was selected out of each year from 1997 to 2006, providing a comprehensive evaluation pool. Each simulation was identical, other than the different ephemeris date, and used the worst-case scenario of a standard sensitivity receiver with no TWTT measurements. The results of the study are listed in Table 4.3.

Table 4.3: Various Dates of Ephemeris and Resulting RMS Position Errors

Ephemeris Date	RMS Position Type	RMS Position Error (m)	% Difference from 1-Jan-06	Ephemeris Date	RMS Position Type	RMS Position Error (m)	% Difference from 1-Jan-06
1-Jan-06	3D	76.09		11-Nov-01	3D	79.07	3.91%
	X (Radial)	66.44			X (Radial)	68.01	2.36%
	Y (In-track)	27.69			Y (In-track)	30.58	10.44%
	Z (Cross-track)	24.68			Z (Cross-track)	26.28	6.49%
27-Mar-05	3D	68.39	10.12%	6-Aug-00	3D	78.18	2.74%
	X (Radial)	61.29	7.76%		X (Radial)	68.13	2.54%
	Y (In-track)	22.68	18.09%		Y (In-track)	30.41	9.84%
	Z (Cross-track)	20.19	18.20%		Z (Cross-track)	23.36	5.37%
16-May-04	3D	70.95	6.76%	20-Jun-99	3D	77.45	1.78%
	X (Radial)	63.51	4.41%		X (Radial)	66.36	0.12%
	Y (In-track)	25.56	7.67%		Y (In-track)	28.74	3.81%
	Z (Cross-track)	18.61	24.60%		Z (Cross-track)	27.71	12.27%
6-Apr-03	3D	74.29	2.36%	26-Jul-98	3D	80.72	6.09%
	X (Radial)	64.02	3.63%		X (Radial)	68.38	2.92%
	Y (In-track)	28.90	4.38%		Y (In-track)	31.59	14.08%
	Z (Cross-track)	24.19	1.98%		Z (Cross-track)	29.03	17.61%
15-Sep-02	3D	76.78	0.91%	10-Aug-97	3D	89.50	17.63%
	X (Radial)	66.42	0.03%		X (Radial)	71.87	8.18%
	Y (In-track)	26.67	3.68%		Y (In-track)	40.56	46.49%
	Z (Cross-track)	27.79	12.59%		Z (Cross-track)	34.64	40.34%

For additional insight, the mean value and standard deviation were calculated across all ten ephemeris dates, given in Table 4.4.

Table 4.4: RMS Position Error Measurement Mean and Standard Deviation Across all Ten Ephemeris Dates

RMS Position Type	Mean (m)	Standard Deviation (m)
3D	77.14	5.72
X (Radial)	66.44	2.97
Y (In-track)	29.34	4.75
Z (Cross-track)	25.65	4.58

The three-dimensional RMS position error mean value is approximately one meter greater than the value for the default January 1, 2006 ephemeris date. This ensures that the 2006 date will be a good representation of the expected values for the simulation at any given time. The 3D RMS standard deviation is less than six meters which is well within acceptable boundaries for instilling confidence in the simulation model.

Trends in the GPS satellite visibility provide another look at the simulation model's validity. Ephemeris data from each of the ten dates produced very similar visibility trends, as they all vary from zero to four with an average of approximately two. Samples of GPS satellite visibility plots are located in Figure 4.9. For the case of a standard sensitivity receiver and no TWTT measurements, the number of visible satellites ranged from zero to four. The only exception was when five GPS satellites were visible for a brief period while using the 2003 ephemeris data. This was the only time more than four satellites were visible.

By examining the RMS position error values and visible GPS satellite plots, it is apparent that differing ephemeris dates do not have a significant impact on the results of the simulation. The simulation is accurate and consistent for any ephemeris data that is used.

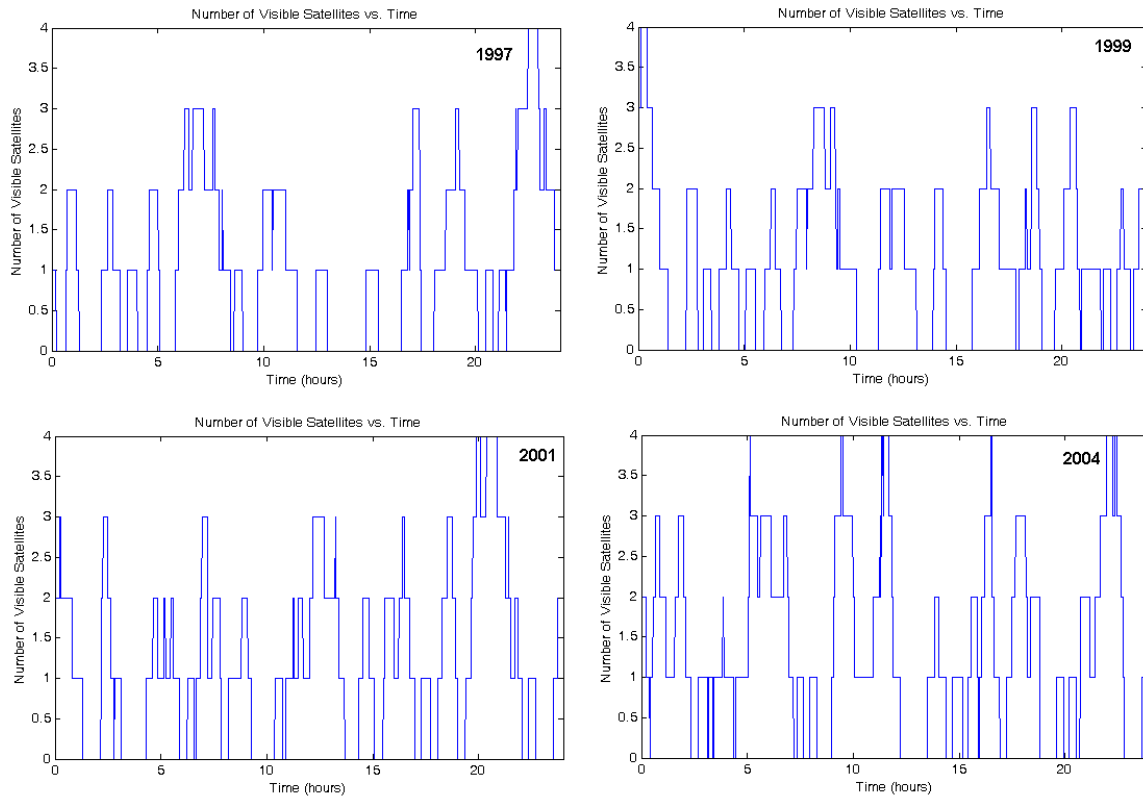


Figure 4.9: GPS Satellite Visibility Plots for a GEO Satellite Using Four Different Ephemeris Dates

4.5 Trade Study 2: GPS Receiver Models

The simulation contains a simple and a complex GPS receiver models. The simple receiver model is strictly concerned with satellite look angles and does not calculate signal path loss, varying degrees of pseudorange measurement noise error, or varying gain patterns. If the GEO satellite is within a GPS satellite's main beam field of view and is not obscured by the Earth, the receiver is assumed to be able to gather a pseudorange measurement. This measurement is simply the vector distance between the two satellites with the addition of white, Gaussian measurement noise with a five-meter standard deviation.

The complex receiver model calculates the received signal strength taking into account transmit and receive antenna gain patterns and path loss, as described in Section 3.4.3. The received signal strength dictates whether or not a pseudorange measurement is available, and if so, measurement noise error, as described in Section 3.4.3.

The simple GPS receiver model is dependent upon the look angle of the GPS satellite. A smaller look angle will limit the number of satellite that the GEO satellite can track simultaneously, while a larger look angle will allow the GEO satellite to track more GPS satellites. The first part of this trade study examines varying the look angle of the GPS satellites and the results are seen in Table 4.5. The 42.6° angle is a common representation of the GPS Block II/IIA main beam, as seen in [1] and others. The 38° and 120° angles were chosen to mimic the Block IIR main beam and Block IIR UHF crosslink beam as shown in [20]. The 50° angle was chosen arbitrarily to represent a modest increase over the commonplace 42.6° Block II/IIA main beam.

Table 4.5: Simple Model RMS Position Error Results with Pseudorange Measurement Noise Error Standard Deviation of 5 meters

GPS Look Angle	RMS Position Type	RMS Position Error (m)		% Decrease in Position Error using TWTT
		<i>no TWTT</i>	<i>Rb TWTT</i>	
38°	3D	90.45	68.34	24.45%
	X (Radial)	73.93	61.88	16.30%
	Y (In-track)	40.63	20.68	49.10%
	Z (Cross-track)	32.64	20.34	37.69%
42.6°	3D	72.66	56.84	21.78%
	X (Radial)	63.93	52.23	18.31%
	Y (In-track)	27.66	15.89	42.56%
	Z (Cross-track)	20.67	15.83	23.44%
50°	3D	51.39	39.20	23.72%
	X (Radial)	47.17	36.12	23.43%
	Y (In-track)	15.67	10.56	32.59%
	Z (Cross-track)	13.05	10.98	15.88%
120°	3D	6.72	4.34	35.45%
	X (Radial)	6.36	3.78	40.65%
	Y (In-track)	1.52	1.49	2.05%
	Z (Cross-track)	1.53	1.53	0.41%

When comparing with the complex GPS receiver model, there are similarities between the simple model's 42.6° look angle and the complex model's standard sensitivity level. The 120° look angle scenario is also similar to the medium plus sensitivity level. These traits are listed in Table 4.6.

Table 4.6: Comparison of Simple and Complex GPS Receiver Model RMS Position Error Values

GPS Look Angle	RMS Position Type	RMS Position Error (m)		% Decrease Using TWTT	GPS Receiver Sensitivity	Cutoff (dB-Hz)	RMS Position Type	RMS Position Error (m)		% Decrease Using TWTT
		<i>no TWTT</i>	<i>Rb TWTT</i>					<i>no TWTT</i>	<i>Rb TWTT</i>	
42.6°	3D	72.66	56.84	21.78%	Standard	32	3D	76.09	60.32	20.73%
	X (Radial)	63.93	52.23	18.31%			X (Radial)	66.44	55.49	16.48%
	Y (In-track)	27.66	15.89	42.56%			Y (In-track)	27.69	17.60	36.43%
	Z (Cross-track)	20.67	15.83	23.44%			Z (Cross-track)	24.68	15.78	36.06%
120°	3D	6.72	4.34	35.45%	Medium Plus	17	3D	6.32	4.08	35.43%
	X (Radial)	6.36	3.78	40.65%			X (Radial)	5.87	3.38	42.49%
	Y (In-track)	1.52	1.49	2.05%			Y (In-track)	1.70	1.66	2.38%
	Z (Cross-track)	1.53	1.53	0.41%			Z (Cross-track)	1.60	1.58	1.09%

The approximated Block II/IIA antenna main beam angle in the simple model produces results very similar to the standard sensitivity level in the complex model. This suggests that the simple model might be sufficient for examining scenarios that involve nominal equipment and values, where it is safe to assume all pseudorange measurement noise errors follow a standard deviation of five meters. Specialized hardware with higher

sensitivity levels will most likely require the complex model to represent the system. Still, the fact that the standard case shows correlation between the simple and the complex models further proves that the simulation is reliable.

The second part of this trade study explores various pseudorange measurement noise error standard deviation values and their effect on three-dimensional positioning accuracy for the simple receiver model. The pseudorange measurement noise error standard deviation is varied between 1, 2, 3, 5, and 7 meters, the results being listed in Table 4.7.

Table 4.7: Simple Model RMS Position Error Results with Varying Pseudorange Measurement Noise Error Standard Deviations and GPS Look Angle of 42.6°

Pseudorange Measurement Error σ	RMS Position Type	RMS Position Error (m)		% Decrease in Position Error using TWTT
		<i>no TWTT</i>	<i>Rb TWTT</i>	
1 m	3D	51.20	34.22	33.17%
	X (Radial)	44.37	30.50	31.24%
	Y (In-track)	21.01	10.67	49.20%
	Z (Cross-track)	14.57	11.26	22.74%
2 m	3D	59.73	42.14	29.44%
	X (Radial)	52.42	38.18	27.16%
	Y (In-track)	23.27	12.34	46.97%
	Z (Cross-track)	16.68	12.90	22.70%
3 m	3D	65.46	48.26	26.27%
	X (Radial)	57.68	44.09	23.55%
	Y (In-track)	25.00	13.68	45.26%
	Z (Cross-track)	18.25	14.05	23.00%
5 m	3D	72.66	56.84	21.78%
	X (Radial)	63.93	52.23	18.31%
	Y (In-track)	27.66	15.89	42.56%
	Z (Cross-track)	20.67	15.83	23.44%
7 m	3D	77.17	62.37	19.17%
	X (Radial)	67.45	57.25	15.12%
	Y (In-track)	29.88	17.72	40.72%
	Z (Cross-track)	22.62	17.28	23.61%

There are distinct similarities between the 7 meter standard deviation value in the simple model and the standard sensitivity level in the complex model. The correlation is shown in Table 4.8.

Table 4.8: Comparison of Simple and Complex GPS Receiver Models Based on Pseudorange Error

Pseudorange Measurement Error σ		RMS Position Type	RMS Position Error (m)		% Decrease Using TWTT
			<i>no TWTT</i>	<i>Rb TWTT</i>	
7 m		3D	77.17	62.37	19.17%
		X (Radial)	67.45	57.25	15.12%
		Y (In-track)	29.88	17.72	40.72%
		Z (Cross-track)	22.62	17.28	23.61%
GPS Receiver	Cutoff (dB-Hz)	RMS Position Type	RMS Position Error (m)		% Decrease Using TWTT
			<i>no TWTT</i>	<i>Rb TWTT</i>	
Standard	32	3D	76.09	60.32	20.73%
		X (Radial)	66.44	55.49	16.48%
		Y (In-track)	27.69	17.60	36.43%
		Z (Cross-track)	24.68	15.78	36.06%

The standard sensitivity level in the complex GPS receiver model limits the number of GPS satellites that are visible to the GEO satellite. The few satellites that are available will most likely be large look angles where the antenna gain patterns will provide the least amount of signal strength to the receiver. Low received signal strength will incur a higher pseudorange measurement noise error. For the complex model, the pseudorange measurement noise error is 15 meters at the receiver's signal strength cutoff boundary (i.e., the lowest signal power that can provide a pseudorange measurement). It makes sense that a 7-meter pseudorange error value would best represent the standard sensitivity level when using the simple model.

4.6 Trade Study 3: Gain Pattern Models

As stated in Section 3.4.3, there are two GPS antenna gain pattern models available for the complex GPS receiver model, taken from two different sources. The simple antenna model provides gain pattern data from nadir to 43°, while the complex model provides data from 0° to 180° off-boresight. Both gain pattern models replicate the GPS Block II/IIA transmit antenna. The primary and secondary lobes are contained in

the 0°-43° portion of the transmit beam (refer to Figure 3.4). Additional lobes exist at higher angles, but the gain is very small. Because the gains are so small at high angles, the complex gain pattern becomes more beneficial as the GPS receiver sensitivity increases. Table 4.9 displays the results of this trade study.

Table 4.9: Comparison of Simple and Complex GPS Gain Pattern Models and Resulting RMS Position Error Values

GPS Receiver Sensitivity	Cutoff (dB-Hz)	RMS Position Type	Complex GPS Gain Pattern Model		Simple GPS Gain Pattern Model		% Difference in Complex and Simple Position Error	
			RMS Position Error (m)		RMS Position Error (m)			
			<i>no IWTI</i>	<i>Rb IWTI</i>	<i>no IWTI</i>	<i>Rb IWTI</i>	<i>no IWTI</i>	<i>Rb IWTI</i>
Standard	32	3D	76.09	60.32	85.34	69.54	12.16%	15.30%
		X (Radial)	66.44	55.49	72.32	63.09	8.85%	13.69%
		Y (In-track)	27.69	17.60	34.84	20.67	25.84%	17.46%
		Z (Cross-track)	24.68	15.78	28.98	20.71	17.42%	31.24%
Standard Plus	27	3D	31.87	24.10	30.02	21.57	-5.80%	-10.49%
		X (Radial)	30.19	22.32	28.29	19.64	-6.30%	-12.03%
		Y (In-track)	8.10	6.97	8.09	6.94	-0.20%	-0.37%
		Z (Cross-track)	6.18	5.85	5.95	5.63	-3.84%	-3.73%
Medium	22	3D	11.34	7.71	16.79	10.98	48.03%	42.47%
		X (Radial)	10.54	6.56	16.04	9.92	52.18%	51.25%
		Y (In-track)	3.11	2.97	3.83	3.58	23.40%	20.60%
		Z (Cross-track)	2.80	2.74	3.12	3.04	11.68%	10.82%
Medium Plus	17	3D	6.32	4.08	10.82	6.40	71.24%	56.97%
		X (Radial)	5.87	3.38	10.41	5.74	77.33%	70.09%
		Y (In-track)	1.70	1.66	2.25	2.15	32.70%	30.06%
		Z (Cross-track)	1.60	1.58	1.88	1.84	17.72%	16.24%
High	12	3D	3.83	2.40	7.06	3.80	84.35%	58.61%
		X (Radial)	3.56	1.95	6.83	3.38	91.71%	73.05%
		Y (In-track)	1.02	1.00	1.36	1.32	33.88%	31.60%
		Z (Cross-track)	0.97	0.96	1.16	1.13	19.44%	17.69%
Ultra High	7	3D	2.36	1.48	4.73	2.39	100.30%	62.08%
		X (Radial)	2.19	1.18	4.59	2.12	110.13%	79.69%
		Y (In-track)	0.65	0.64	0.87	0.84	34.14%	32.06%
		Z (Cross-track)	0.63	0.62	0.75	0.73	19.91%	18.10%

As mentioned previously, the complex gain pattern is required when the GPS receiver sensitivity increases. For the standard sensitivity, where the small gains that exist at high look angles cannot be utilized, the simple gain pattern will most likely be sufficient for accurate simulation results.

When using a “standard plus” sensitivity level, the simple gain pattern appears to be more accurate than the complex gain pattern. This is most likely due to slight differences in the lobe sizes and positions between the two gain pattern models. The

minimum gain value between the primary and secondary lobes is different by a few degrees between the two models, which could cause the accuracy of the simple gain pattern model to be exaggerated in this particular situation.

4.7 Trade Study 4: Clock Type Selection

Three types of clocks are available in the simulation model. An ovenized crystal clock represents an inexpensive, commonly-used clock that would be onboard most common satellites. The Cesium and Rubidium atomic clocks represent hardware that provides much greater precision and accuracy in time measurements. GPS time is governed by high-quality atomic clocks like the Rubidium clock in this model.

This trade study examines the impact of atomic clocks on three-dimensional position error. Because pseudorange measurement accuracy is bound to the quality of the clock involved, it is expected that higher-accuracy clocks will provide smaller position errors. The results of this trade study are listed in Table 4.10.

Table 4.10: Comparison of Clock Types and Resulting 3D RMS Position Error Values (in meters)

GEO Clock	TWTT Ref Clock	GPS Receiver Sensitivity					
		Standard (32 dB-Hz)	Standard+ (27 dB-Hz)	Medium (22 dB-Hz)	Medium+ (17 dB-Hz)	High (12 dB-Hz)	Ultra High (7 dB-Hz)
Crystal	None	76.09	31.87	11.34	6.318	3.830	2.363
Crystal	Cesium	60.33	24.12	7.722	4.103	2.431	1.518
Crystal	Rubidium	60.32	24.10	7.707	4.080	2.396	1.476
Cesium	None	60.37	24.16	7.772	4.135	2.447	1.518
Cesium	Cesium	60.31	24.10	7.702	4.080	2.400	1.482
Cesium	Rubidium	60.31	24.09	7.697	4.071	2.386	1.464
Rubidium	None	60.36	24.14	7.757	4.112	2.413	1.476
Rubidium	Cesium	60.30	24.09	7.696	4.070	2.385	1.461
Rubidium	Rubidium	60.30	24.09	7.694	4.067	2.381	1.456

As expected, the inclusion of TWTT measurements provides smaller position errors, as does a more accurate clock. As the sensitivity of the GPS receiver increases, there is a smaller percent decrease in position error. With the high sensitivity receiver, there are enough quality measurements to drastically reduce the clock error, so the addition of TWTT measurements is less significant. The percent decrease in 3D RMS position error per scenario is listed in Table 4.11.

Table 4.11: Percent Decrease in 3D RMS Position Error Compared to Scenario Using Ovenized Crystal GEO Satellite Clock, no TWTT, Standard Sensitivity Receiver

GEO Clock	TWTT Ref Clock	GPS Receiver Sensitivity					
		Standard (32 dB-Hz)	Standard+ (27 dB-Hz)	Medium (22 dB-Hz)	Medium+ (17 dB-Hz)	High (12 dB-Hz)	Ultra High (7 dB-Hz)
Crystal	None						
Crystal	Cesium	20.71%	24.31%	31.91%	35.06%	36.54%	35.77%
Crystal	Rubidium	20.73%	24.36%	32.04%	35.43%	37.43%	37.55%
Cesium	None	20.66%	24.19%	31.47%	34.55%	36.12%	35.75%
Cesium	Cesium	20.74%	24.38%	32.08%	35.43%	37.34%	37.28%
Cesium	Rubidium	20.74%	24.39%	32.13%	35.57%	37.70%	38.04%
Rubidium	None	20.68%	24.23%	31.60%	34.92%	37.00%	37.54%
Rubidium	Cesium	20.75%	24.40%	32.14%	35.58%	37.74%	38.16%
Rubidium	Rubidium	20.75%	24.40%	32.15%	35.62%	37.83%	38.37%

It is interesting to note that the inclusion of an atomic clock makes a remarkable impact on the position error. As long as there is at least one atomic clock involved in the navigation process, the highest accuracy is achieved. For example, when a Rubidium TWTT reference clock is introduced to an ovenized crystal clock on the GEO satellite, the effect is the same as having a single Rubidium clock on the GEO satellite, or a Rubidium clock in both locations. The difference between these three scenarios is on the order of millimeters of three-dimensional position error. This means that a cheap, simple, durable clock can be placed on a satellite in a harsh unstable environment, while the

expensive, complex, fragile atomic clock can reside at a TWTT reference clock station on Earth in a controlled environment.

4.8 Trade Study 5: TWTT Measurement Noise Error

TWTT measurements are subject to measurement noise error, just as the pseudorange measurements are. It is expected that as technology advances, TWTT measurements will become more accurate, lowering the amount of error. This trade study examines the impact of varying TWTT measurement noise error, ranging between standard deviation values of 10, 3, 0.3, 0.03, and 0.003 meters. Table 4.12 displays the results of varying the TWTT measurement noise error standard deviation. Gaps in the table exist because some scenarios were deemed of lesser importance and eliminated to save computation time.

Table 4.12: Comparison of Various TWTT Measurement Noise Error Standard Deviation Values and Resulting 3D RMS Position Errors (in meters)

GEO Clock	TWTT Ref Clock	TWTT Measurement Error σ (m)	GPS Receiver Sensitivity					
			Standard (32 dB-Hz)	Standard+ (27 dB-Hz)	Medium (22 dB-Hz)	Medium+ (17 dB-Hz)	High (12 dB-Hz)	Ultra High (7 dB-Hz)
Crystal	Cesium	10	63.582		8.155		3.106	
		3	60.911	24.563	7.849	4.224	2.597	1.739
		0.3	60.330	24.118	7.722	4.103	2.431	1.518
		0.03	60.323	24.111	7.718	4.099	2.424	1.509
		0.003	60.323		7.718		2.424	
Crystal	Rubidium	10	63.575		8.143		3.093	
		3	60.899	24.551	7.836	4.202	2.567	1.710
		0.3	60.317	24.103	7.707	4.080	2.396	1.476
		0.03	60.310	24.096	7.703	4.076	2.390	1.466
		0.003	60.310		7.703		2.390	
Rubidium	Rubidium	10	60.306		7.700		2.393	
		3	60.305	24.090	7.696	4.070	2.385	1.462
		0.3	60.304	24.089	7.694	4.067	2.381	1.456
		0.03	60.303	24.088	7.694	4.067	2.380	1.456
		0.003	60.303		7.694		2.380	

Varying the TWTT measurement error has a small effect on the position accuracy in the simulation. When the 3D RMS position error is 24 and 60 meters, having a TWTT measurement accuracy greater than 3 meters will gain 50-60 centimeters of position accuracy. When the position error is 1-7 meters, increasing the TWTT measurement accuracy beyond 3 meters gains 0-30 centimeters.

Overall, the accuracy of the TWTT measurements is not extremely critical. In some cases it will provide half a meter of increased accuracy, but it is usually less than that.

4.9 Additional TWTT Study – TWTT Reference Clock Locked to GPS Time

The investigation of the impact of TWTT measurements on GPS navigation led to another scenario concept that involved a reference clock that is synchronized with GPS time. If the reference clock could exactly match GPS time, then the receiver clock error could be essentially removed from the pseudorange measurement using the TWTT measurement. In this case, the TWTT reference clock errors are not estimated by the Kalman filter (since they are zero), as they were in the previous cases. Using the TWTT with the reference clock synchronized to GPS time significantly reduced the position error, as shown in Table 4.13. The use of TWTT in this mode resulted in 60-70% improvement in positioning accuracy, depending on the receiver sensitivity.

Table 4.13: Comparison of 3D Position RMS Error (meters) When Using a TWTT Reference Clock that is Synchronized with GPS Time

GEO Clock	TWTT	GPS Receiver Sensitivity					
		Standard (32 dB-Hz)	Standard+ (27 dB-Hz)	Medium (22 dB-Hz)	Medium+ (17 dB-Hz)	High (12 dB-Hz)	Ultra High (7 dB-Hz)
Crystal	None	76.09	31.86	11.34	6.32	3.83	2.36
Rubidium	None	60.36	24.14	7.76	4.11	2.41	1.48
Crystal	Rubidium	60.32	24.10	7.71	4.08	2.40	1.48
Rubidium	Rubidium	60.30	24.09	7.69	4.07	2.38	1.46
Crystal	GPS Time	22.93	9.01	4.07	2.33	1.44	0.95

4.10 Summary

This chapter outlined the simulation results and provides analysis of the data. The baseline results provide the fundamental information used to compare against each trade study. The trade studies included using ephemeris data from different days, using a simple and complex GPS receiver model, using a simple and complex GPS antenna gain pattern, varying the clock types found on the GEO satellite and TWTT reference station, and adjusting the TWTT measurement error.

The results indicate that changing the ephemeris date has no effect on the simulation data, so the model is valid for any day. The simple GPS model and GPS gain pattern proved useful for low sensitivity receivers, but the complex model and gain pattern are required for mid- to high-sensitivity receivers. As long as a single high-accuracy atomic clock is available somewhere in the system, either on the satellite or supplied via TWTT measurements, the position accuracy is the same. Having a TWTT measurement error standard deviation smaller than 3 meters had little effect on the three-dimensional position error of the satellite. A value of 30 centimeters proved to be as beneficial as a value of 3 centimeters. Most importantly, providing a TWTT reference

clock which is slaved to GPS time offers radical position accuracy enhancements, far beyond what is achievable with current GPS receivers alone.

Chapter 5 will provide summary conclusions and recommendations for future research in this area.

5 Conclusions and Recommendations

5.1 Significance of Research

The goal of this research was to evaluate the benefits of Two-Way Time Transfer measurements when used to augment GPS navigation at very high altitudes like geostationary orbit. At this altitude, the receiver is above the GPS satellite constellation, a location where the GPS system was not designed to provide navigation information. The satellite geometry at GEO severely limits the number of usable GPS satellites, since the Earth occludes most of the GPS signals from the GEO satellite. In order to produce navigation information, a minimum of four satellites are needed to solve for the three dimensional position and clock error. When less than four satellites are available, the clock error cannot be resolved and the information provided is not very useful.

TWTT provides a method for resolving the clock error when less than four GPS satellites are visible. TWTT is a technique that involves simultaneously exchanging signals between two or more clocks and is one of the most accurate ways to compare clocks. With TWTT measurements, the clock error between the GPS satellite transmitter and the GEO satellite receiver can be resolved, allowing useful information to be gleaned from any number of visible satellites, even if it is less than four.

This capability allows any standard GPS receiver to operate effectively on a GEO satellite with reasonable accuracy. Accurate GPS navigation in high-altitude orbits provides numerous opportunities, such as automated station-keeping in a GEO orbit. Also, by substituting automation and removing the ground-based ranging systems, the cost reduction incurred by reducing ground support is considerable.

To summarize the key results into a single figure, five scenarios were selected: 1) Ovenized crystal GEO clock, no TWTT, 2) Rubidium GEO clock, no TWTT, 3) Ovenized crystal GEO clock, TWTT to Rubidium reference, 4) Rubidium GEO clock, TWTT to Rubidium reference, 5) Ovenized crystal GEO clock, TWTT to clock synchronized to GPS time. Each of these scenarios were run. The three-dimensional Root Mean Square (3D RMS) position error for each simulation run is provided in Figure 5.1.

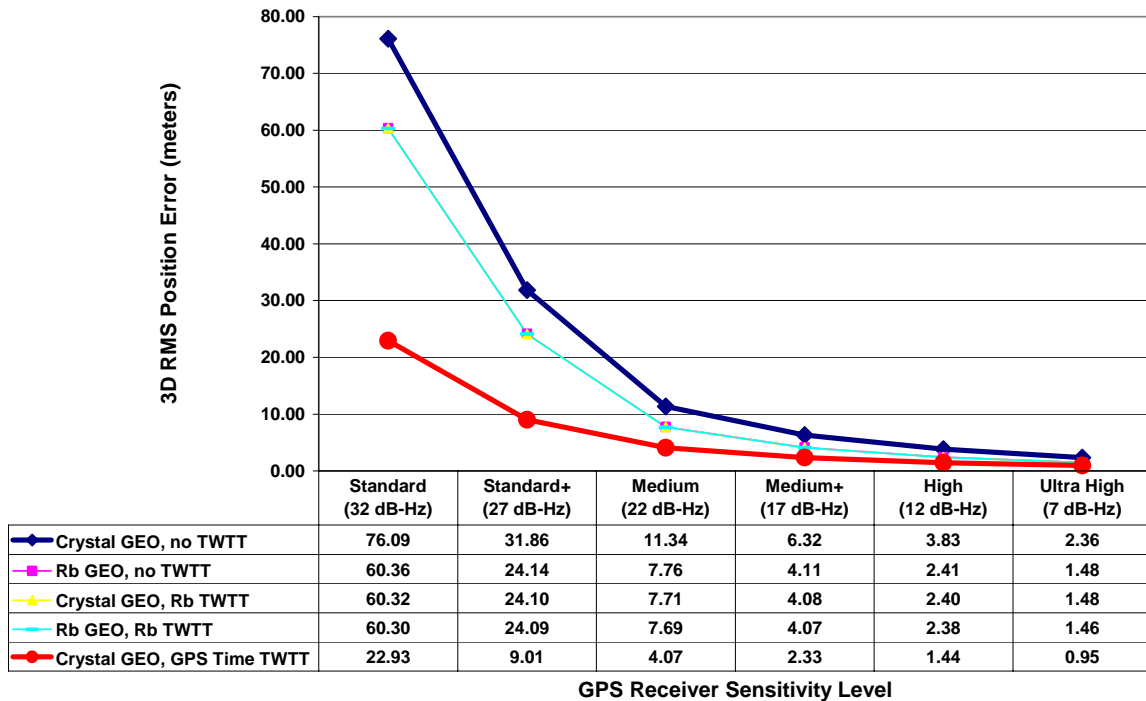


Figure 5.1: Keystone Plot – 3D RMS Position Error vs. GPS Receiver Sensitivity Levels and Clock Configurations

This is the key plot that captures the essence of this thesis research, as it clearly describes the benefit of including TWTT measurements with GPS pseudorange measurements for navigation. Introducing an atomic clock provides some positioning improvement, but the breakthrough occurs when the TWTT reference clock is

synchronized with GPS time, offering a 60-70% reduction in three-dimensional position error.

The precise clock does not necessarily need to reside on the satellite, but rather can be placed on Earth where it can be better protected and maintained. Also, if the precise clock fails, the on-orbit satellite is not rendered inoperable. Ovenized crystal clocks are less complex and more robust, making them a better candidate for space flight, further emphasizing the importance of keeping the precise atomic clock on the ground.

The idea of using TWTT measurements in GPS navigation has been explored in the original user environment on Earth, and provided exceptional accuracy improvements. By now addressing TWTT measurements used in GPS navigation in high-altitude orbits, such as GEO, the accuracy improvements are even more remarkable.

5.2 Trade Studies

A number of additional trade studies were performed using this simulation. Results are summarized in the sections that follow.

5.2.1 Baseline Results

The baseline results are the primary research results and are compared with the trade studies. These primary results consist of six GPS receiver sensitivity levels that are used with and without TWTT measurements. The GEO satellite clock is an ovenized crystal clock, the TWTT reference clock is a Rubidium clock, and the TWTT measurement error standard deviation is 0.3 meters.

It is apparent that increasing the sensitivity level of the GPS receiver provides the greatest improvement in measurement accuracy. Using a single GPS receiver with a

predefined sensitivity level, the inclusion of TWTT measurements does allow for significant positioning accuracy improvements that would otherwise not be available. This improvement ranges from 21% (when using a standard sensitivity receiver) to 38% (when using an ultra high sensitivity receiver).

5.2.2 Trade Study 1: Ephemeris Date

To ensure that the simulation model does not depend on ephemeris data, ten separate days were tested. The same scenario was run for each day and the results were examined to find similar trends that would suggest correlation.

The mean 3D RMS position error value is 77.14 meters, while the standard deviation is 5.72 meters. The standard deviation is less than 10% of the mean value, insinuating that there are no large anomalies when varying the ephemeris data. The GPS satellite visibility plots for each ephemeris date are very similar, each providing the same general level of satellite coverage to the GEO satellite. These findings indicate that the output of the simulation model will not be corrupted by slight differences in ephemeris data, thus the model is valid for any day.

5.2.3 Trade Study 2: GPS Receiver Models

The simulation model contains two types of GPS receiver models. The first type is a simple model that only examines the maximum look angle of the GPS satellite and the cutoff angle between the GPS satellite and the Earth that obscures the GEO satellite. The simple model uses a constant pseudorange measurement noise error standard deviation value. The second type is a complex model that accounts for look angles, gain

patterns, signal strengths, and varying pseudorange measurement error standard deviation values.

The first part of this trade study examines the effect of GPS satellite look angle on the GEO satellite 3D RMS position error. Increasing the GPS satellite look angle has a similar effect as increasing the GPS receiver sensitivity level in the baseline results. The 42.6° look angle is comparable to the standard sensitivity level, while the 120° look angle is comparable to the medium plus sensitivity level.

The second part of this trade study examines the effect of pseudorange measurement noise error standard deviation on the GEO satellite 3D RMS position error. A standard deviation value of 7 meters is comparable to the standard sensitivity level in the baseline results.

The simple GPS receiver model does not have the precision of the complex model, but it is still relatively accurate. Using a GPS satellite look angle of 42.6° and a pseudorange error of 7 meters, the simple model performs very similarly to the complex model when using an ovenized crystal clock on the GEO satellite, with and without a Rubidium TWTT reference clock. This is an additional step toward validating the complex GPS receiver model, which provides the most realistic results.

5.2.4 Trade Study 3: Gain Pattern Models

The complex GPS receiver model uses either a simple or a complex GPS satellite antenna gain pattern. This trade study examines the impact of various GPS satellite antenna gain patterns on the GEO satellite 3D RMS position error.

When using a lower sensitivity GPS receiver, the difference in 3D RMS position error values between the simple and complex GPS satellite antenna gain pattern models is

the largest, but the percent difference is the smallest. The 3D RMS position error for a standard sensitivity receiver will differ by 9.25 meters, which is 12% of the 3D RMS position error when using the complex antenna gain pattern. The reverse is true for the higher sensitivity receivers. The 3D RMS position error for an ultra high sensitivity receiver will differ by only 2.37 meters, which is a 100% increase changing from the complex antenna gain pattern model to the simple model. This trade study shows that the simple GPS satellite antenna gain pattern model is accurate and correlates well with the complex model, indicating the complex model is reliable and accurate while also providing more realistic results.

5.2.5 Trade Study 4: Clock Type Selection

There are three different types of clock available in the simulation model for use in the GEO satellite and the TWTT reference station. This trade study examines how varying the clock type in both locations affects the GEO satellite 3D RMS position error.

It is immediately apparent that whenever an atomic clock is introduced, the position results for a particular GPS receiver sensitivity level reach maximum accuracy. If a Rubidium clock is placed on the GEO satellite and no TWTT measurements are used, the end result is the same as having an ovenized crystal clock on the GEO satellite and a Rubidium clock as the TWTT reference. This trade study suggests that TWTT will allow any satellite to benefit from an atomic clock without the burden of carrying one on orbit.

5.2.6 Trade Study 5: TWTT Measurement Noise Error

This trade study examines the effects of altering the TWTT measurement error standard deviation value on the GEO satellite 3D RMS position error. The default

standard deviation value throughout the simulation runs is 0.3 meters, which is representative of a sophisticated TWTT setup.

The TWTT measurement accuracy does not appear to have much effect on the 3D RMS position error of a GEO satellite. When using a standard sensitivity GPS receiver, changing the TWTT measurement error standard deviation from 10 meters to 3 meters gains approximately 3 meters of position accuracy, or 4%. When using a higher sensitivity receiver, the 3D RMS position accuracy improvement is on the order of centimeters. This trade study indicates that a TWTT measurement error standard deviation value smaller than 0.3 meters gains relatively nothing.

5.2.7 Additional TWTT Study – Reference Clock Locked to GPS Time

This additional study addressed a TWTT scenario where the reference clock is set to match GPS time. This will allow the GPS receiver to maintain the exact time as the GPS satellites. As a result, the pseudorange measurements will have all clock error removed, allowing the calculation of a three-dimensional position with only three satellites, since clock error no longer needs to be solved. This configuration will allow more than three times the amount of positioning accuracy as compared to the scenario using an atomic clock in the TWTT system.

5.2.8 Overall Results

The first three trade studies provide key information that allows a deeper understanding of the simulation model. By varying parameters and exploring the results, the model can be validated, ensuring that the output is reasonable and accurate. The mechanics of the simple GPS receiver model are relatively easy to test and confirm, so

using the simple model to help validate the complex model is a natural step towards a reliable simulation.

The last two trade studies examine the concept of aiding GPS pseudorange positioning with TWTT, and explore the benefits and limitations of such a system. By testing different clock configurations and TWTT measurement noise error values it is confirmed that a single atomic clock placed anywhere in the system can provide an increase in positioning accuracy, anywhere from 21-38%. By creating a reference clock that is synchronized with GPS time, the positioning accuracy increases by 70%.

5.3 Recommendations for Future Research

5.3.1 Improve Simulation Fidelity

There are many aspects of the simulation model that have the potential for enhancement. This research was focused on the accuracy improvements that TWTT measurements offer, not on complicated orbital dynamics, sophisticated signal transmission and reception mechanics, or the inclusion of all possible error sources. The following paragraphs describe portions of the simulation model that could be improved to include many of the items discussed above.

The simulation could be enhanced to model each GPS satellite appropriately by using specific information on the individual Block of GPS satellite used by each PRN. Currently, the simulation uses the same transmit antenna gain pattern and transmit power for all GPS satellites. Obviously, every single GPS satellite in orbit is not a Block II/IIA variant, so the simulation model should more accurately represent all of the current satellite variants in orbit. Some of the newer GPS satellites provide higher transmit

power, which could provide greater three-dimensional positioning accuracy than this simulation indicates.

Similarly, the simulation should model the actual GPS receiver that is built into the GEO satellite. The simulation currently uses a low-cost, off-the-shelf GPS receiver patch antenna that provides 4dB gain or less. If the GEO satellite is using a higher-quality antenna that provides higher receiver gain, the results would also provide a greater positioning accuracy than indicated in this research.

A sophisticated propagation model (not just simple two-body dynamics) for the GEO satellite orbit truth propagation and filter propagation should be developed. The simple propagator does not account for perturbations in the Earth's gravity field, the gravity of the sun and moon, solar wind pressure, atmospheric drag, or any other high-order phenomenon. These effects could alter the results of the simulation, and should be modeled for complete accuracy.

5.3.2 Investigate a Non-standard GPS Receiver Antenna on the GEO Satellite

This simulation assumes that the GPS receiver points directly to the center of the Earth and has maximum gain at a zero degree look angle (boresight). From GEO, the Earth blocks most of the GPS satellites from view, so all visible GPS satellites will be at an angle from the GEO satellite. It is intuitive that the GPS receiver antenna should not have maximum gain that points toward the center of the earth if the received signals will come from an angle. Instead, the GEO satellite GPS receiver antenna should have maximum gain at an angle that will coincide with the direction of the visible GPS satellites.

A GPS satellite transmit antenna uses a gain pattern with maximum gain at approximately 10° , providing the maximum signal power to the limb of the Earth where atmospheric loss will be the greatest for a ground user. It is recommended that the GEO satellite GPS receiver have a similar gain pattern, allowing the maximum signal power reception to be in line with the visible GPS satellites. By boosting received signal power in this manner, the pseudorange measurement noise errors will be reduced, providing more accurate navigation information.

Appendix A – GPS Satellite Visibility Plots

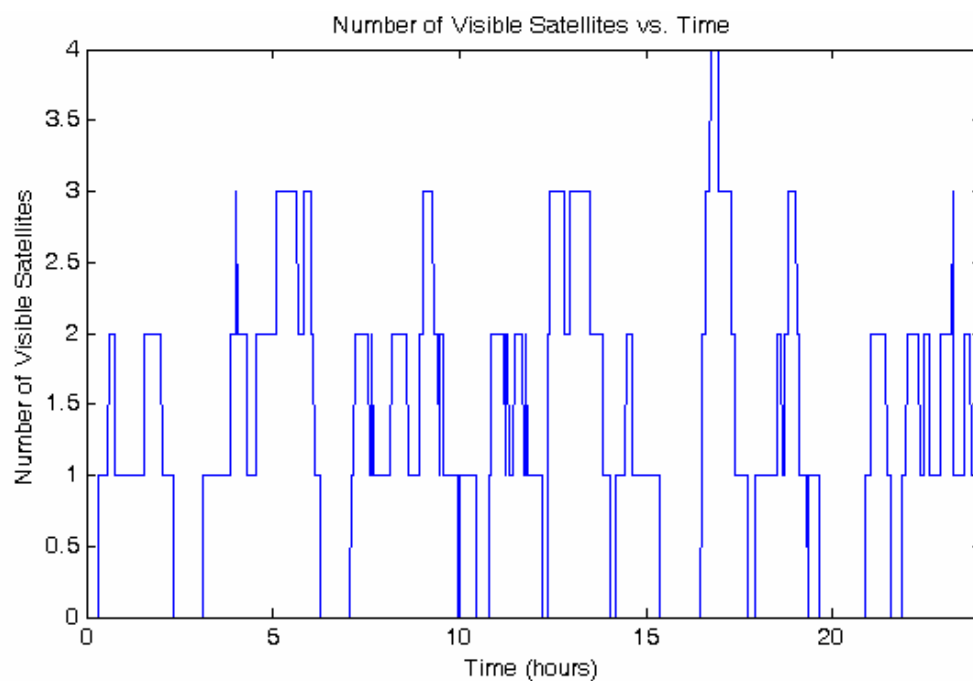


Figure A.1: GPS Satellite Visibility from GEO for Standard Sensitivity Receiver (32 dB-Hz cutoff)

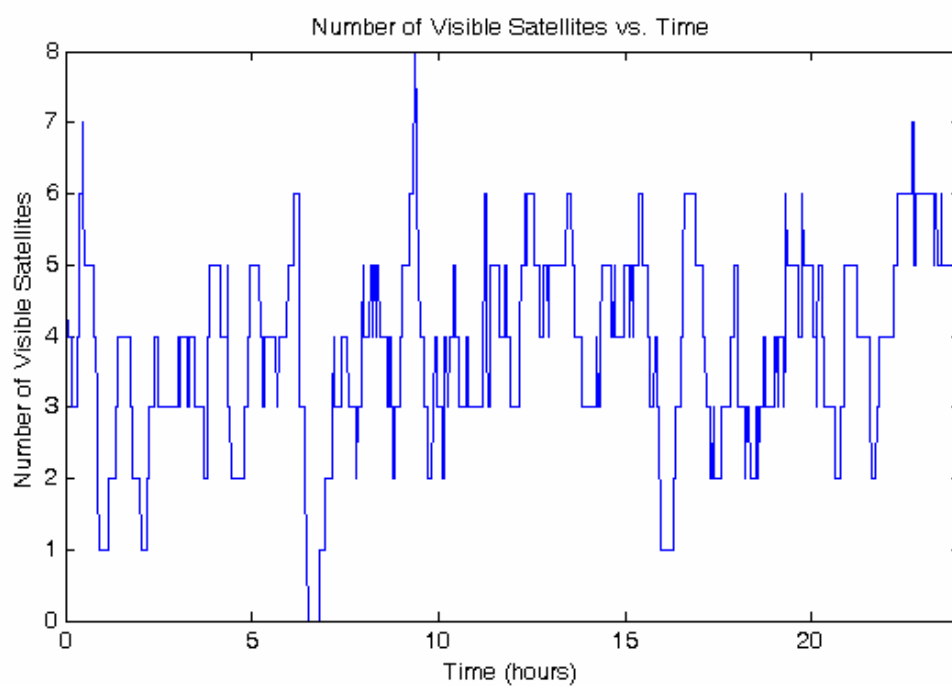


Figure A.2: GPS Satellite Visibility from GEO for Standard Plus Sensitivity Receiver (27 dB-Hz cutoff)

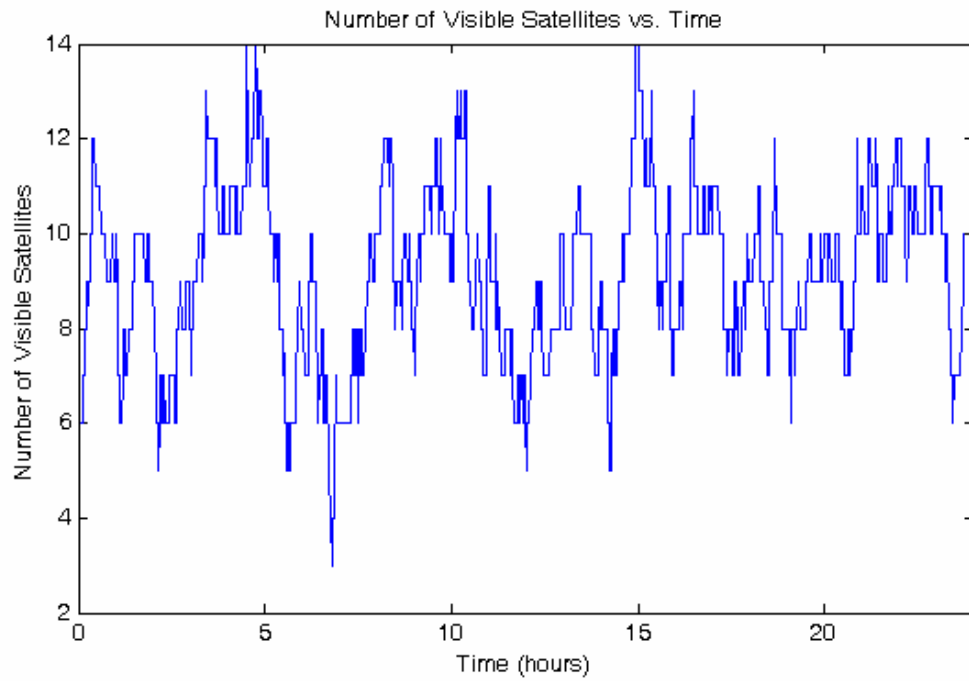


Figure A.3: GPS Satellite Visibility from GEO for Medium Sensitivity Reciever (22 dB-Hz cutoff)

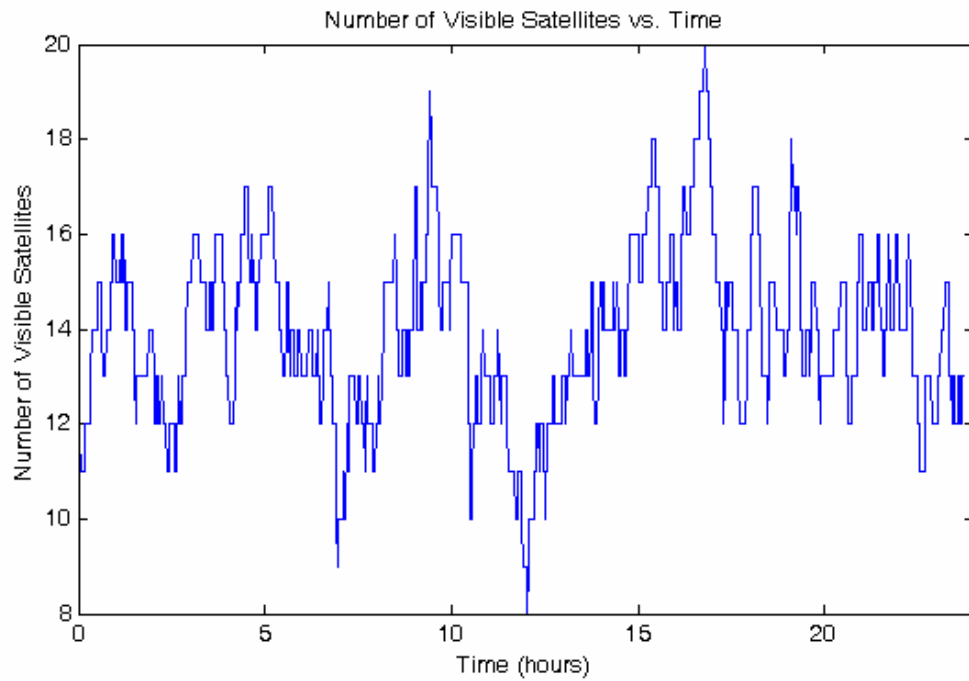


Figure A.4: GPS Satellite Visibility from GEO for Standard Plus Sensitivity Reciever (17 dB-Hz cutoff)

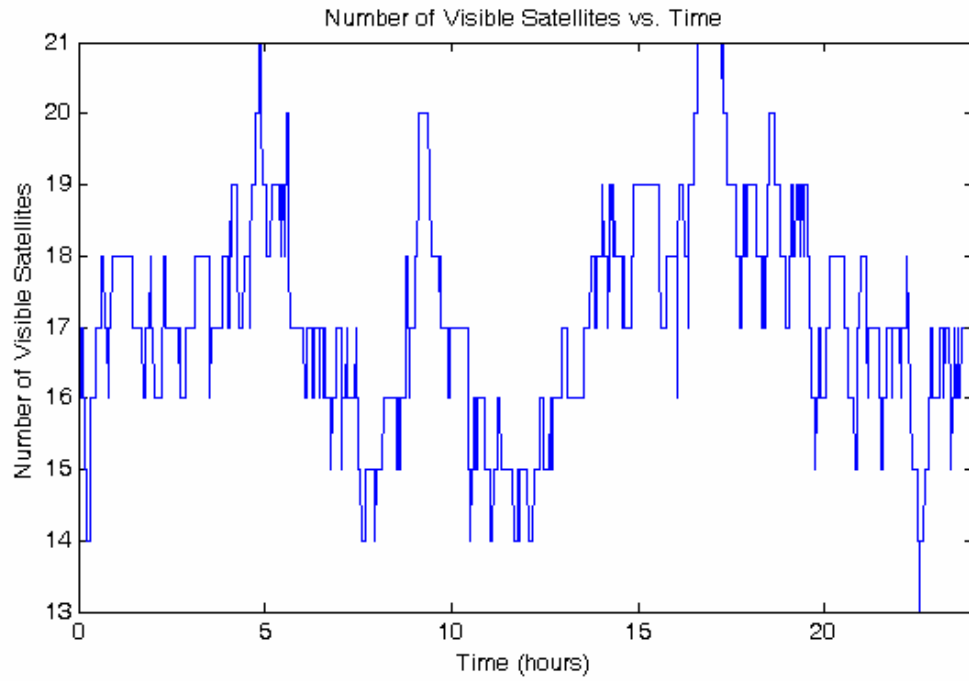


Figure A.5: GPS Satellite Visibility from GEO for High Sensitivity Reciever (12 dB-Hz cutoff)

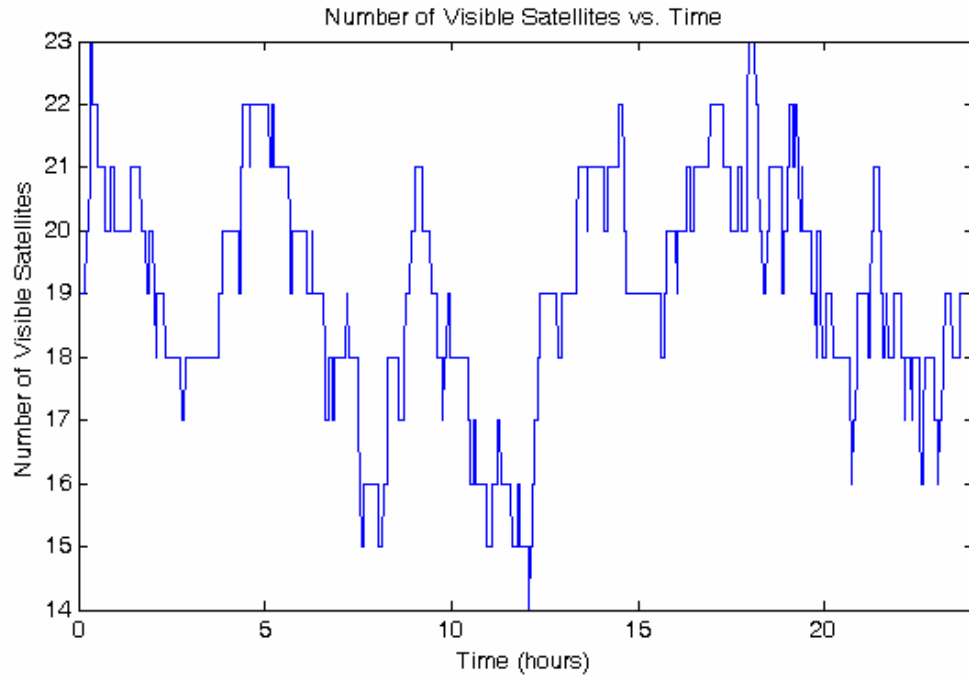


Figure A.6: GPS Satellite Visibility from GEO for Ultra High Sensitivity Reciever (7 dB-Hz cutoff)

Bibliography

- [1] Bamford, William, Curtis Hay, and Luke Winternitz. "Spacecraft Navigator: Autonomous GPS Positioning at High Earth Orbits." *GPS World*, 17: 50-55 (April 2006).
- [2] Beckman, Richard, Tom Celano, Scott Francis, Al Gifford, Peter Howe, and Jeremy Warriner. "Dynamic Two-Way Time Transfer to Moving Platforms." Proceedings of IEEE International Frequency Control Symposium and PDA Exhibition Jointly with the 17th European Frequency and Time Forum, 2003.
- [3] Beckman, Richard, Tom Celano, Scott Francis, Al Gifford, Peter Howe, and Jeremy Warriner. "Two-Way Time Transfer to Airborne Platforms Using Commercial Satellite Modems." Proceedings of 34th Annual Precise Time and Time Interval (PTTI) Meeting, 2002.
- [4] Brown, Allison and Kenn Gold. "Architecture and Performance Testing of a Software GPS Receiver for Space-based Applications." Proceedings of IEEEAC, Big Sky, Montana, March 2004.
- [5] Brown, Kenneth R. "Characterizations of OCS Kalman Filter Errors." Proceedings of the ION GPS-91, 148-158, September 1991.
- [6] Brown, Kenneth R. "The Theory of the GPS Composite Clock." Proceedings of the ION GPS-91, 223-241, September 1991.
- [7] Brown, Robert G. and Patrick Y.C. Hwang. *Introduction to Random Signals and Applied Kalman Filtering*. New York: John Wiley & Sons, Inc., 1997.
- [8] Cook, Kendra L. B. "Characterizing the Impact of Precision Time and Range measurements From Two-Way Time Transfer Systems on Network Differential GPS Position Solutions." Masters Thesis, AFIT, 2006.
- [9] Czopek, Francis M. and Scott Shollenberger. "Description and Performance of the GPS Block I and II L-Band Antenna and Link Budget." Proceedings of the ION GPS-93, Volume I, 1993.
- [10] *Differential GPS Explained*. ESRI: Geographic Information System (GIS) and Mapping Software, 2003. 6 February 2007.
<http://www.esri.com/news/arcuser/0103/differential1of2.html>.
- [11] Frey, Charles and Jennifer Ruiz. "Geosynchronous Satellite Use of GPS." Proceedings of the ION GNSS 18th International Technical Meeting of the Satellite Division, Long Beach, September 2005.

- [12] *Global Positioning System (GPS)*. IEEE Virtual Museum, 2007. 5 January 2007
<http://www.ieee-virtual-museum.org/collection/tech.php?taid=&id=2345902&lid=1>.
- [13] Hanson, D.W. "Fundamentals of Two-Way Time Transfers by Satellite." 43rd Annual Symposium on Frequency Control, Boulder, 1989.
- [14] Hutsell, Steven T. "Fine Tuning GPS Clock Estimation in the MCS." 26th Annual Precise Time and Time Interval (PTTI) Applications and Planning Meeting, 63-74, December 1994.
- [15] Logsdon, T. *The Navstar Global Positioning System*. New York: Van Nostrand Reinhold, 1992.
- [16] Misra, Pratap and Per Enge. *Global Positioning System: Signals, Measurements, and Performance*. Lincoln, Massachusetts: Ganga-Jamuna Press, 2001.
- [17] National Research Council. "The Global Positioning System, a Shared National Asset, Recommendations for Technical Improvements and Enhancements." Technical Report, National Academy Press, Washington DC, 1995.
- [18] Parkinson, B.W. and J.J. Spilker. "Global Positioning System: Theory and Applications, Volume 1." American Institute of Aeronautics and Astronautics, Inc., Washington DC, 1996.
- [19] Powell, Thomas D., Philip D. Martzen, Steven B. Sedlacek, Chia-Chun Chao, Randy Silva, Alison Brown, and Gabriele Belle. "GPS Signals in a Geosynchronous Transfer Orbit: 'Falcon Gold' Data Processing." Proceedings of Institute of Navigation, National Technical Meeting 'Vision 2010: Present and Future." Proceedings of the ION GPS-99, San Diego, 1999.
- [20] Powell, Thomas D., William A. Feess, and Micheal D. Menn. "Evaluation of GPS Architecture for High Altitude Spaceborne Users." Proceedings of Institute of Navigation 54th Annual Meeting, Denver, Colorado, 157-165, June 1998.
- [21] Raquet, John F. "EENG 533: Navigation Using GPS." Air Force Institute of Technology, Spring 2006.
- [22] Raquet, John F. "EENG 633: Advanced GPS Theory and Applications." Air Force Institute of Technology, Summer 2006.
- [23] Vallado, David A. *The Fundamentals of Astrodynamics and Applications*. New York: The McGraw-Hill Companies, Inc., 1997.
- [24] Wiesel, William E. *Modern Orbit Determination*. Beavercreek, OH: Aphelion Press, 2003.

- [25] Woodfork, D. “The Use of X-Ray Pulsars for Aiding GPS Satellite Orbit Determination.” Masters Thesis, AFIT, 2005.

REPORT DOCUMENTATION PAGE				Form Approved OMB No. 074-0188	
<p>The public reporting burden for this collection of information is estimated to average 1 hour per response, including the time for reviewing instructions, searching existing data sources, gathering and maintaining the data needed, and completing and reviewing the collection of information. Send comments regarding this burden estimate or any other aspect of the collection of information, including suggestions for reducing this burden to Department of Defense, Washington Headquarters Services, Directorate for Information Operations and Reports (0704-0188), 1215 Jefferson Davis Highway, Suite 1204, Arlington, VA 22202-4302. Respondents should be aware that notwithstanding any other provision of law, no person shall be subject to a penalty for failing to comply with a collection of information if it does not display a currently valid OMB control number.</p> <p>PLEASE DO NOT RETURN YOUR FORM TO THE ABOVE ADDRESS.</p>					
1. REPORT DATE (DD-MM-YYYY) 22-03-2007		2. REPORT TYPE Master's Thesis		3. DATES COVERED (From – To) Aug 2005 – Mar 2007	
4. TITLE AND SUBTITLE Use of Two-Way Time Transfer Measurements to Improve Geostationary Satellite Navigation				5a. CONTRACT NUMBER	
				5b. GRANT NUMBER	
				5c. PROGRAM ELEMENT NUMBER	
6. AUTHOR(S) Dainty, Benjamin G., Captain, USAF				5d. PROJECT NUMBER	
				5e. TASK NUMBER	
				5f. WORK UNIT NUMBER	
7. PERFORMING ORGANIZATION NAMES(S) AND ADDRESS(S) Air Force Institute of Technology Graduate School of Engineering and Management (AFIT/EN) 2950 Hobson Way WPAFB OH 45433-7765				8. PERFORMING ORGANIZATION REPORT NUMBER AFIT/GSS/ENG/07-01	
9. SPONSORING/MONITORING AGENCY NAME(S) AND ADDRESS(ES) N/A				10. SPONSOR/MONITOR'S ACRONYM(S)	
				11. SPONSOR/MONITOR'S REPORT NUMBER(S)	
12. DISTRIBUTION/AVAILABILITY STATEMENT APPROVED FOR PUBLIC RELEASE; DISTRIBUTION UNLIMITED.					
13. SUPPLEMENTARY NOTES					
14. ABSTRACT <p>An emerging use of GPS is to provide accurate navigation information for satellites in orbit. The GPS satellites are designed to provide service to terrestrial users, so the antenna array points directly towards the Earth and uses a narrow primary beamwidth. Because GEO altitudes are well above the GPS constellation, the Earth occludes most of the GPS signals to the satellite. Decreased satellite visibility is debilitating, as GPS navigation requires at least four visible satellites to determine position. To assist with the visibility problem, the receiver can look at the GPS satellite transmit antenna side lobes, but this does not entirely solve the navigation problem. GPS measurements are inherently bound by receiver clock errors. The clock error must be known or estimated in order to obtain meaningful ranging information. To obtain three-dimensional positioning, at least four satellites must be tracked to solve for three dimensions of position plus the receiver clock error. A new method for improving geostationary navigation accuracy using GPS is to correct the time error by including Two-Way Time Transfer (TWTT) measurements. TWTT is a technique in which signals are simultaneously exchanged between two clocks, and is one of the most accurate methods of comparing clocks. By effectively removing the clock error between the GPS satellite and the GPS receiver, TWTT allows meaningful information to be gathered when less than four GPS satellites are available. The results show a 21-38% improvement in the 3-D RMS position accuracy while using TWTT between the GEO satellite and an atomic clock on the ground. There was a 60-70% improvement when the clock on the ground was synchronized to GPS time.</p>					
15. SUBJECT TERMS GPS, Two-Way Time Transfer, Geostationary orbit, Kalman filter, space navigation					
16. SECURITY CLASSIFICATION OF:			17. LIMITATION OF ABSTRACT UU	18. NUMBER OF PAGES 113	19a. NAME OF RESPONSIBLE PERSON John F. Raquet (ENG)
REPORT U	ABSTRACT U	c. THIS PAGE U			19b. TELEPHONE NUMBER (Include area code) (937) 255-6565, ext 4580; e-mail: john.raquet@afit.edu

Standard Form 298 (Rev. 8-98)
Prescribed by ANSI Std. Z39-18